Study of the dynamics of transport and mixing in fluid systems using set oriented methods

Pradeep C. Rao

Dissertation submitted to the Faculty of the
Virginia Polytechnic Institute and State University
in partial fulfillment of the requirements for the degree of

Doctor of Philosophy
in
Engineering Mechanics

Mark A. Stremler, Chair
Shane D. Ross
Saad Ragab
Anne Staples
Mark R. Paul

Dec 10, 2013
Blacksburg, Virginia

Keywords: Chaotic Advection, Mixing, Coherent Sets

Study of the dynamics of transport and mixing in fluid systems using set oriented methods

Pradeep C. Rao

(ABSTRACT)

Efficient mixing can be achieved in flows where turbulence is absent, if the trajectories of passively advected particles in the flow are chaotic. The chaotic nature of particle trajectories results in exponential stretching of material lines in the flow. Thus the interface along which diffusion occurs is stretched exponentially leading to efficient mixing. It has been demonstrated recently that regions in flow fields that exhibit poor mixing and non-chaotic particle trajectories can have an important bearing on the overall dynamics and transport of the entire domain.

The space-time trajectories of physical stirrers or elliptic points in two dimensional flows can be classified according to braid groups. One can predict a lower bound on the topological entropy (i.e. exponential rate of stretching of material lines) of flows (h_f) by applying the Thurston-Nielsen classification theorems to these braids. This gives a reduced order model for the dynamics of transport of the entire flow field using just a few points. Recent work has shown that this methodology can be used to estimate a lower bound on h_f using the braids formed by Almost Cyclic Sets (ACS) in certain periodic Stokes' flows. These ACS are closely related to Almost Invariant Sets (AIS) which are identified using a probabilistic set oriented method that makes use of the descritised Perron-Frobenius operator of the flow map.

This work extends this approach to flows at non-zero Reynolds numbers, which take into

account the effects of inertia. The role of Finite Time Coherent Structures (FTCS) in the dynamics of flow fields is also investigated. Unlike ACS, the FTCS approach is more general as it can be applied to aperiodic flow fields. Further, the relationship between mixing efficiency and the topological entropy of flow fields at non-zero Reynolds numbers is also studied.

Dedication

To Bhargavi.

Acknowledgements

I would like to thank my advisor Dr. Mark Stremler, for his guidance, infinite patience, and his faith in my ability. This thesis would not have been possible without his insight and ability to explain the most complicated and confusing concepts in the simplest of terms. I would also like to thank Dr. Shane Ross for his discussions with me on almost invariant sets.

I am grateful to my collegues Saikat Basu, Vikas Krishnamurthy, Arshad Mehmood, Shibabrat Naik, Souvik Chatterjee, Mohsen Gheisarieha and Naveen Prakash for their companionship and support.

Contents

List of Figures

Chapter 1

Introduction

Transport and mixing are important and widely studied phenomena in the field of fluid mechanics. They find application in a wide spectrum of areas ranging from the design of lab-on-a-chip devices, the manufacture of dyes, polymers and metals, and efficient combustion in engines, to the study of atmospheric and oceanic currents. The traditional approach used to improve mixing rates in a system has been to make the flow field turbulent, as transition to turbulence from laminar flows results in improved mass and momentum transfers. However, in many applications, turbulence is either impossible to achieve (eg. when dealing with very viscous fluids or very small scales) or is undesirable (eg. for biofluids) [2]. The main mechanism available for transport and mixing in such cases is diffusion which can be a very slow process.

One way of enhancing mixing in laminar flows is by increasing the area of the interface along which diffusion occurs. It was shown by Aref [3] that this can be achieved in simple flows by ensuring that the trajectories of passively advected particles are chaotic, thereby introducing the notion of *chaotic advection*. Subsequently, chaotic advection has been shown to occur in a wide variety of time dependent two-dimensional, and steady three-dimensional flows [2, 4, 5]. In all these studies, regions of a flow field that are characterised by chaotic

particle trajectories were shown to display good mixing, compared to regions where particle trajectories are not chaotic.

Contrary to intuition, however, the dynamics of poorly mixed regions in the flow field can have a significant effect on mixing and transport in the entire flow field. Boyland et. al. [6] showed this through mixing achieved in a very viscous two-dimensional flow through the motion of three stirring rods. The authors applied the Thurston-Nielsen classification theorem (TCNT) to the topology of stirrer motions to predict lower bounds on stretching rates based on whether the stirrers formed a pseudo-Anosov (pA) or finite-order braid. This method gives a reduced order model for the dynamics of the system based on the dynamics of very few points in the system. The use of this topological methodology was later extended to points on periodic and aperiodic orbits, fixed points, and coherent structures in the flow field [7, 8, 9]. The main strength of this approach is that, by ensuring that certain trajectories in the flow field are on a pA braid, one can guarantee a minimum degree of complexity in the flow.

An effective tool in the detection of coherent structures in a flow field is the calculation of eigenvectors and singular vectors of the discretised Perron-Frobenius operator of the flow map [10, 11], which give us almost invariant sets (AIS) and finite time coherent sets (FTCS), respectively, in the flow. Almost invariant sets are closely related to almost cyclic sets (ACS) in time-periodic flow fields [10]. The dynamics of the ACS identified in the most dominant AIS found using this approach has been shown to be closely related, through the use of topological tools, to the dynamics, transport and mixing in 2D lid driven Stokes' flows in Refs. [9, 12]. In these studies, the authors showed that the TCNT can be applied to the topology of the motion of ACS in a Stokes' flow field to get a strict lower bound on the complexity in the flow. The work presented in this dissertation aims to extend this result to flows at non-zero Reynolds numbers where effects due to inertia can not be neglected. It also establishes the relation between coherent sets and transport in flow fields where the underlying flow is not derived directly from a flow field that has elliptic points on a pA braid.

The relation between the dynamics of FTCS in the flow and complexity is also investigated. Thus, this dissertation aims to characterise the influence of coherent structures in laminar flows at finite Reynolds numbers identified from AIS and FTCS on the dynamics of transport and mixing.

This thesis is organised as follows. Chapter 2 covers the mathematical preliminaries regarding AIS and TCNT, describes the reference Stokes' flow used in this study, and discusses the numerical techniques used for simulating flows at finite Reynolds numbers. Chapter 3 investigates the relation between AIS, topological entropy of the flow calculated using a line-stretching algorithm and mixing efficiency. Chapter 4 describes the methodology used in this thesis for identifying ACS and FTCS in the flow, and discusses the results for flows at finite Reynolds numbers that are based on a Stokes' flow containing elliptic points on a pA braid. Chapter 5 discusses the topological entropy results of the braids produced by coherent structures in flows at finite Reynolds numbers that are based on a Stokes' flow case that has elliptic points on a finite-order braid. The conclusions of this thesis are presented in chapter 6.

Chapter 2

Background and mathematical preliminaries

2.1 Set oriented methods for detecting coherent structures in flow fields

2.1.1 Almost-invariant and almost-cyclic sets

This section describes a set oriented probabilistic technique that can be used to detect statistically important sets in phase space for dynamical systems that can be described as iterations of flow maps. This technique makes use of the discretised Perron-Frobenius operator of the flow map to find regions in phase space that have minimal exchange of trajectories between them. A detailed description of this method can be found in Refs. [13, 14, 10, 15]. The sets identified using this method are called almost-invariant sets. Fig. 2.1 shows a schematic of such sets in a rectangular two-dimensional domain.

Consider a non-autonomous dynamical process described by the ordinary differential equa-

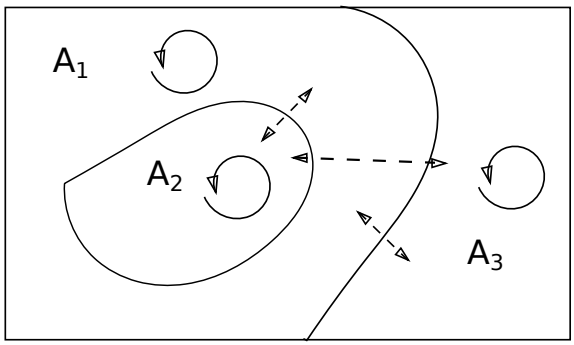

Figure 2.1: Schematic representation of 3 almost invariant sets. The probability is high that trajectories that start in one of the 3 sets remain in that set.

tion

$$\dot{x} = f(x,t), \tag{2.1}$$

where $x \in X \subset \mathbb{R}^l$, X is compact, and $f : X \times \mathbb{R} \to \mathbb{R}^l$ is a smooth vector field. Let the solution to this ordinary differential equation be described by the time dependent flow map $\Phi_\tau : X \times \mathbb{R} \to X$, which defines a diffeomorphism, i.e. a one-to-one mapping with an inverse, both being differentiable. The location of the trajectory of a point in the flow which is at x_0 at time t_0 after τ time units is given by $\Phi_\tau(x_0, t_0)$.

A set $A \subset X$ is said to be Φ-invariant over $[t, t+\tau]$ if $A = \Phi_{-s}(A, t+s)$ for all $0 \leq s \leq \tau$ [13]. This implies that all trajectories in A at time t remain in A over the period $[t, t+\tau]$ in the Eulerian sense. If the flow map Φ is periodic in time with a period τ (owing to the periodicity in time of Eq. (2.1)), we can define invariance in a weaker sense with respect to a discrete time map. In that case, a set $A \subset X$ is said to be Φ-invariant with a period τ if $A = \Phi_{-\tau}(A, t+\tau)$, which implies that all and only trajectories that are in A at time t return to A after flowing for τ time units, as defined by the discrete time map Φ_τ.

Coherent structures are defined here to be regions in the flow that tend to stick together, and are approximately (or almost) invariant over short periods of time. To be able to define approximate or almost invariance, define a Borel σ-algebra with a probability measure μ on X. Let μ be preserved by Φ. μ is an invariant measure if $\mu(\Phi_{-\tau}(A, t+\tau)) = \mu(A)$. Set

$A \subset X$ is said to be almost invariant with respect to a probability measure μ if

$$\rho_{\mu,\tau}(A) := \frac{\mu(A \cap \Phi_{-\tau}(A, t+\tau))}{\mu(A)} \approx 1, \tag{2.2}$$

where $\rho_{\mu,\tau}(A)$ is the proportion of set A that remains in A after flowing for a period of τ starting from time t, with respect to the probability measure μ [13, 10]. Note that we need to use a measure that is invariant under the action of Φ to be able to compare sets subjected to the mapping, and the Lebesgue measure m is not necessarily invariant under Φ.

Now consider the Perron-Frobenius or transfer operator $\mathcal{P}_\tau : \mathcal{M} \to \mathcal{M}$ on the space of bounded complex valued measures defined by

$$(\mathcal{P}_\tau \nu)(A) = \nu(\Phi_{-\tau}(A, t+\tau)), \quad A \subset X \text{measurable}, \quad \nu \in \mathcal{M}. \tag{2.3}$$

This operator describes the evolution of bounded complex measures brought about by the flow from time t to time $t+\tau$ [13]. $\mathcal{P}_\tau$ is an infinite dimensional operator, and can be approximated by a finite dimensional linear operator $P_{n,\tau}$, which is computed as follows. The domain X is partitioned by $\mathcal{B} = B_1, \cdots, B_n$, a set of connected compact boxes as shown in Fig. 2.2. The ijth entry of the matrix $P_{n,\tau}$ is then given by the relation

$$P_{n,\tau;ij} = \frac{m(B_i \cap \Phi_{-\tau}(B_j, t+\tau))}{m(B_i)}, \tag{2.4}$$

where m represents normalised Lebesgue measure. Thus, the entry $P_{n,\tau;ij}$ represents the probability that a point from bin B_i at time t will be in B_j at time $t+\tau$ [10]. The matrix $P_{n,\tau}$ is stochastic, and is typically sparse, and its transpose defines a finite Markov chain. $P_{n,\tau}$ has a positive left eigenvector p_n corresponding to an eigenvalue of 1, which is used to construct an estimate of the unique fixed point h of $\mathcal{P}_\tau$ by setting

$$h_{n,i} = \frac{p_{n,i}}{m(B_i)}. \tag{2.5}$$

This is used to define the corresponding invariant probability measure used in Eq. (2.2) [15],

$$\mu_n(A) = \sum_{i \in I} h_{n,i}, \tag{2.6}$$

with $A \in \mathcal{C}_n$, $I \subset \{1, \cdots n\}$, where $\mathcal{C}_n$ is defined in Eq. (2.8).

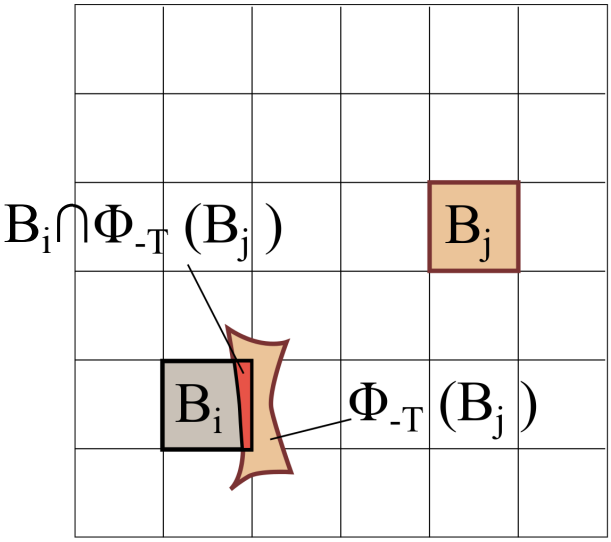

Figure 2.2: To compute $P_{t,\tau}$ numerically, the domain is binned into boxes and the intersection of the pre-image of every box B_i with every box B_j is calculated.

To numerically approximate the finite dimensional transfer operator using Eq. (2.4), we define N points in each bin B_i and calculate $\Phi_\tau(x_{i,k}, 0)$, where $k \in \{1, \cdots, N)$ and $x_{i,k}$ is the initial position of the k^{th} point in bin B_i, by numerically integrating the trajectories of each point. As in Ref. [15], we calculate

$$P_{n,\tau;ij} = \frac{\#\{k : x_{i,k} \in B_i, \Phi_\tau(x_{i,k}, 0) \in B_j\}}{N}, \tag{2.7}$$

where $\#\{.\}$ represents the number of points in set $\{.\}$. To be able to find maximally optimal almost invariant sets in X, we restrict A to elements of $\mathcal{C}_n$ where

$$\mathcal{C}_n := \{A \subset X : A = \cup_{i \in I} B_i, I \subset \{1, \cdots, n\}\}. \tag{2.8}$$

The probability measure of any such set can then be calculated using the relation

$$\mu_n(A) := \sum_{i \in I} p_{n,i}, \quad \text{where} \quad A = \sum_{i \in I} B_i, \quad I \subset \{1, \cdots, n\}, \tag{2.9}$$

and therefore the invariance of any $A \in \mathcal{C}_n$ is approximated using

$$\rho_{\mu_{n,\tau}} := \frac{\sum_{i,j \in I} p_{n,i} P_{n,\tau,ij}}{\sum_{i \in I} p_{n,i}}. \tag{2.10}$$

The stochastic matrix $P_{n,\tau}$ is not invariant to time reversal, i.e. the probability of a trajectory moving from bin B_i to B_j under the action of Φ_τ is not necessarily the same as the probability of a trajectory moving from bin B_j to bin B_i. We obtain a reversible Markov chain from $P_{n,\tau}$ using the relation

$$R_{n,\tau} := (P_{n,\tau} + \hat{P}_{n,\tau})/2, \tag{2.11}$$

where $\hat{P}_{n,\tau}$ is the finite-state Markov chain obtained from the time reversal of the transition matrix $P_{n,\tau}$, and is calculated by substituting $\Phi_{-\tau}$ for Φ_τ in Eq. (2.7). If a point is at position x at time $t = \tau$, $\Phi_{-\tau}(x, \tau)$ gives its position at time $t = 0$ after advecting it back in time for τ time units. The value of $\rho_{\mu_{n,\tau}}$ remains unchanged by substituting $R_{n,\tau}$ for $P_{n,\tau}$ in Eq.(2.10)[10]. Further, there exist theoretical bounds for $\max_{A \in C_n} \rho_{\mu_{n,\tau}}(A)$ when $\mu_{n,\tau}(A) \leq \frac{1}{2}$ in terms of the second eigenvalue of $\lambda^{(2)}$ of $R_{n,\tau}$ given by

$$1 - \sqrt{2(1 - \lambda^{(2)})} \leq \max_{A \in C_n} \rho_{\mu_{n,\tau}}(A) \leq \frac{1 + \lambda^{(2)}}{2}. \tag{2.12}$$

The maximally almost invariant sets in the flow can be obtained by calculating the right eigenvectors $\hat{v}^{(i)}$ of $R_{n,\tau}$, which are ordered with respect to decreasing eigenvalues [10].

Each $\hat{v}^{(i)}$ divides X into two almost invariant partitions, and the degree of invariance of the sets obtained is ordered by the magnitudes of the corresponding eigenvalues $\lambda^{(i)}$. The

higher the value of λ^i, the more invariant, and therefore, the less leaky are the almost invariant sets obtained from the corresponding eigenvalues. The eigenvector $\hat{v}^{(1)}$ corresponds to an eigenvalue of 1 and represents the entire domain X since it is bounded and therefore invariant. To partition X using any subsequent eigenvector, say $v^{(2)}$, we select c such that $\min_{1\leq i\leq n} v_i^{(2)} \leq c \leq \max_{1\leq i\leq n} v_i^{(2)}$ to divide X into two sets

$$A_1 = \cup_{i\in I_1} B_i, \qquad \text{where } I_1 = \{i : \hat{v}_i^{(2)} \leq c\}, \tag{2.13}$$

$$A_2 = \cup_{i\in I_2} B_i, \qquad \text{where } I_2 = \{i : \hat{v}_i^{(2)} \geq c\}. \tag{2.14}$$

The value of c is selected such that it maximises $\min\{\rho_{n,\tau}(A_1), \rho_{n,\tau}(A_2)\}$. Alternately, information from multiple eigenvalues with values close to 1 can be combined to obtain multiple AIS using a clustering algorithm as shown in Ref. [10].

For the purposes of this study, the AIS structures are used primarily to find sets on cycles in a time-periodic flow field. Almost cyclic sets (ACS) are groups of sets with a probability for a trajectory starting in one set to return to that set after visiting every set in the group once. The methodology developed to identify these almost cyclic sets using the AIS data in this study is outlined in §4.1.

2.1.2 Detecting coherent sets in aperiodic flow fields

The set oriented probabilistic approach to finding coherent structures in flows described in §2.1.1 is suitable for autonomous dynamical systems, and flow fields where velocity is periodic in time. This restriction exists because the method attempts to detect sets $A \subset X$ such that $A \approx \Phi(A)$, which implies that trajectories that start in A should either stay in A for long times or visit A for many applications of Φ. Thus, this method does not apply to trajectories that tend to stick together for long periods as they travel through the phase space, but do not satisfy the above two conditions. Most real flows, such as atmospheric,

oceanic and industrial flows, are not exactly periodic in time and are therefore not very amenable to the analysis described in §2.1.1.

Finite-time coherent sets, which are regions that stay coherent over a specific time interval, are more general and therefore find more application than the almost invariant sets defined previously. It is hypothesized that the motions of such structures will play an important role in global transport and mixing in non-periodic flows. Froyland et. al. [11] present a set oriented probabilistic methodology to detect such finite-time coherent sets, which are minimally dispersive, or maximally coherent, under the flow for a finite time interval. The coherent pairs of sets thus found are robust under diffusive perturbations, and the method favors sets that are geometrically regular. Another advantage of this method is that it is applicable to dynamical systems that map the domain to a different region in the phase space and are not necessarily volume preserving. This method therefore can be applied to systems where particles leave the original domain, and can thus be used to study open flows such as atmospheric and oceanic flows.

This method involves calculating the singular values of the discretised Perron Frobenius operator associated with the flow map (as opposed to eigenvectors for calculating the AIS) and is outlined here briefly. Consider a map $\Phi : X \to Y$, where $X, Y \subset M \subset \mathbb{R}^l$, that defines the solution to a smooth non-autonomous dynamical system $\dot{x} = f(x,t)$, $x \in M$. An example of such a map is a map that gives the position of a particle being advected in a 2-D plane after time τ, given its initial position. Let X and Y be subdivided into disjoint sets or bins $\{B_1, \cdots, B_m\}$ and $\{C_1, \cdots, C_n\}$ respectively. If $\Phi(X)$ is a strict subset of Y, we discard all B_i such that $\Phi(B_i) \cap Y = \emptyset$ and all C_j such that $\Phi(X) \cap C_j = \emptyset$, and renumber the bins. The discretised Perron-Frobenius operator associated with Φ_τ is numerically estimated using the relation

$$P_{n,\tau}(t)_{i,j} = \frac{m(B_i \cap \Phi_{-\tau}(C_j, t+\tau))}{m(B_i)}. \tag{2.15}$$

where m here again is the normalised Lebesgue measure. By construction, the matrix $P_{n,\tau}$

is row-stochastic in nature, and $P_{n,\tau}(t)_{i,j}$ denotes the probability that a randomly selected point in B_i has its image in C_j.

To numerically approximate the finite dimensional transfer operator using Eq. (2.15), we define N uniformly distributed points in each bin B_i and calculate $\Phi_\tau(x_{i,k})$, where $k \in \{1, \cdots, N)$ and $x_{i,k}$ is the initial position of the k^{th} point in bin B_i, by numerically integrating the trajectories of each point. As in Ref. [11], we calculate

$$P_{n,\tau}(t)_{ij} = \frac{\#\{k : x_{i,k} \in B_i, \Phi_\tau(x_{i,k}) \in C_j\}}{N}. \tag{2.16}$$

The main difference in the above equation as compared to the equation for the discretised Perron-Frobenius operator for the AIS approach is that C_j above is replaced with B_j in eq. 2.7. That is to say, the Perron-Frobenius operator for the FTCS approach can map densities from a domain to a different co-domain, whereas for the AIS approach, the domain and co-domain need to be the same.

Let X be endowed with a probabilistic measure μ, and further, let $p_i = \mu(B_i)$ and $q_j = P_{\tau,ij}p_i$. The probability measure μ in this case is not necessarily invariant under the action of $P_{n,\tau}$, and m can be used as a possible candidate for the same. As proved in Ref. [11], the most coherent sets in the flow, each with measure roughly half the domain, can be extracted from the left and right singular vectors corresponding to the second largest singular value of $\Pi_p^{1/2} P_\tau \Pi_q^{-1/2}$. Here Π_p is an $m \times m$ diagonal matrix with p on the diagonal, and Π_q is an $n \times n$ matrix with q on the diagonal. The actual coherent sets are then calculated in the same manner as in the previous section, by using each right singular vector to divide the domain into two regions, and identifying coherent structures using a thresholding algorithm. This methodology is further explained in §4.2.

2.2 Topology of stirring motions and its relation to the complexity of flow fields

Boyland et. al [6] introduced the notion of "built in" chaos through the topology of stirrer motions in bounded two dimensional flows. Mixing can be achieved through the prescribed motions of stirrers in the flow and the boundary, called "stirring protocols", that define discrete time flow maps that are diffeomorphisms (mappings that have an inverse, such that both the mapping and its inverse are differentiable) given by

$$h : R_k \to R_k, \tag{2.17}$$

where R_k is the bounded domain containing k stirrers or "holes". Let us assume that the stirrers are returned to their originial positions by h, up to a permutation.

All stirring protocols in which the stirrers are fixed in place, but can rotate, and the boundary can move tangentially, fall under the category of *fixed stirrer diffeomorphisms*. Note that all mappings possible using the equations of motions for fluids only form a subset of this class of diffeomorphisms. Fixed stirrer diffeomorphisms can be described by a time parameterised set of mappings ψ_t, $t \in [0, 1]$, and we call $\psi_0 = \mathrm{id}$, the identity. We say that a diffeomorphism h is *isotopic to the identity* if there exists a set of fixed stirrer diffeomorphisms such that $\psi_0 = \mathrm{id}$ and $\psi_t = h$. That is, h is isotopic to the identity if the mapping can be produced by a fixed stirrer diffeomorphism (or in other words, the mapping can be produced by a continuous deformation while keeping the stirrers fixed). We say two diffeomorphism g and f are isotopic to each other if there exists a diffeomorphism h isotopic to the identity such that $g = hf$. Thus, given a diffeomorphism h, we can define its *isotopy class*, which is the set of all diffeomorphisms isotopic to h.

According to the Thurston-Nielsen (TN) classification theorem [16] every homeomorphism h of a compact surface has a TN representative ϕ in its isotopy class that is one of the following

types:

1. Finite order: $\phi^n = \mathrm{id}$ for some integer $n > 0$.

2. Pseudo-Anosov (pA): ϕ causes stretching and contraction everywhere by factors λ and λ^{-1}. Thus repeated application results in exponential stretching of fluid elements. λ is called the *dilatation* and $\log \lambda$ is the *topological entropy*.

3. Reducible: ϕ divides the domain into a family of closed curves within which ϕ satisfies either 1 of 2.

A homeomorphism is a continuous function with a continuous inverse, and therefore by definition, every diffeomorphism is a homeomorphism. Thus the TN classification theorem applies to diffeomorphisms as well. If a diffeomorphism has a pA representative in its isotopy class, Handel's isotopy stability theorem guarantees the presence of a region in the domain that stretches and contracts everywhere at least by λ and λ^{-1} [17]. The size of this region relative to that of the domain is not predicted, however, but experiments indicate that it is of the scale of the stirrer motions for Stokes' flows [6, 18]. Thus, if we can show that a diffeomorphism has a TN representative that is pA, it is reasonable to expect exponential stretching of material lines in some part of the domain, and we can predict the lower bound on the stretching rate. Exponential stretching of material lines is an indicator of chaotic particle trajectories which typically leads to efficient mixing [3], and thus any mapping that has a pA representative in its isotopy class should achieve good mixing in some part of the domain [6].

One way of acertaining the type of TN representative present in the isotopy class of a stirring protocol is studying the braid formed by the stirrers. The train-track algorithm by Bestvina-Handel [19] tells us which isotopy class the TN representative belongs to using the braid. The physical braid of a stirring protocol is the three dimensional space-time plot of all the stirrers in the domain. The braid can be described by a sequence of elementary crossings

between stirrer trajectories which are called *generators*, and which form a braid group. This description was introduced by Artin in Ref. [20]. A generator $\sigma_i,\ i = 1 \cdots k-1$, denotes the clockwise interchange between strands i and $i+1$ keeping all other strands fixed, where i is the position of strands from left to right and not a label for a particular strand [21]. Similarly a counterclockwise exchange is denoted by σ_i^{-1}. Two braids are equivalent if they have the same order of crossings, irrespective of the actual path taken by the stirrers.

Concatenating generators of successive interchanges together from left to right gives the algebraic braid and we can thus define a *braid group on k strands,* B_k. The identity element of the braid group is the identity braid, which corresponds to no braiding or to disentangled strands. For algebraic braids to correspond to physical braids, we require that elements of B_k satisfy two additional properties, namely, $\sigma_i\sigma_{i+1}\sigma_i = \sigma_{i+1}\sigma_i\sigma_{i+1}$ and $\sigma_i\sigma_j = \sigma_j\sigma_i$, for $|i-j| > 1$ [22].

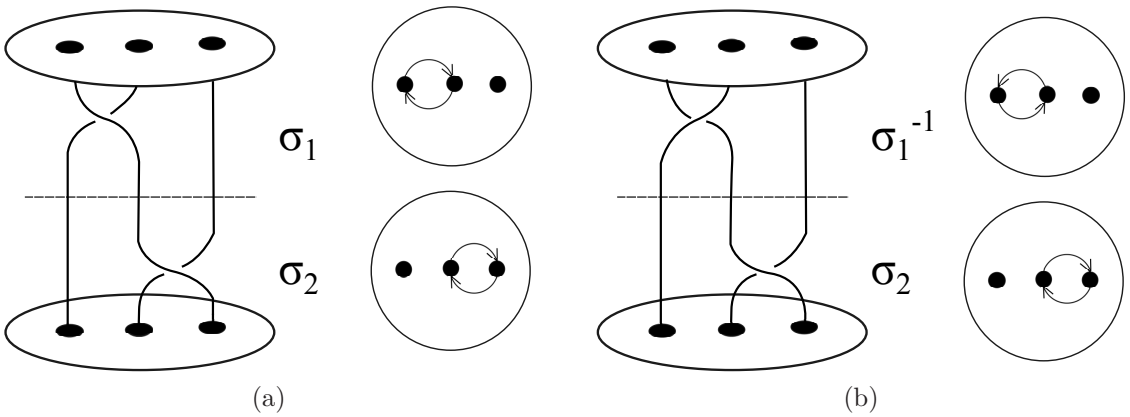

Figure 2.3: Braids formed by the trajectories of stirrer motions in time (time increases upwards) for (a) the braid $\sigma_2\sigma_1$ whose TN representative is of finite order type and (b) the braid $\sigma_2\sigma_1^{-1}$ whose TN representative is of pA type.

Once the algebraic description of the braid is computed, one can calculate the growth rate of non-trivial loops due to the braid, which is exponential if the braid has a pA representative. For example, for the braid $\sigma_2\sigma_1^{-1}$ shown in Fig. 2.3 (b), the dilatation is $\lambda = (3+\sqrt{5})/2$ and the topological entropy $h_{\text{braid}} = \log((3+\sqrt{5})/2) \approx 0.962$. h_{braid} is the lower bound on the topological entropy of the flow h_{f,τ_f^*}, which can be defined as the exponential growth rate of

non-trivial material lines in the flow [23].

This thesis makes use of two methods for the calculation of h_f from the braid generators obtained from the trajectories of passively advected points in the flow field. The first is the freely available implementation of the Bestvina-Handel (train tracks) algorithm by Toby Hall [24]. This algorithm is very accurate and gives more information about the braid other than the isotopy class and topological entropy, but has exponential computational complexity. Thus, this algorithm becomes prohibitively expensive to use for more than around 40 generators [23]. The train tracks algorithm is therefore more suitable for cases where the number of braid generators is small, which is typical of periodic maps. The second algorithm used is the algorithm developed by Mousaffir [25] which uses the Dynnikov coordinates [26] to keep track of the number of crossings of a material curve with the projection axis. The Dynnikov encoding uses the least amount of information required to track the growth rate of a material curve which makes it very efficient for calculating the topological entropy in cases with many generators. For an easy to follow implementation of Moussafir's algorithm, please see Ref. [21].

The above methods give us the entropy of the braid formed by a finite number of points in the flow field (h_{braid}). This gives us a lower bound on the complexity in the flow [6, 23]. A line stretching algorithm is used to estimate the topological entropy of the entire flow field (h_f). A non-trivial line in the flow field defined by a set of discrete points is advected in time and the asymptotic growth rate of this line gives h_f [27]. Distances between points can grow exponentially in a flow that exhibits chaotic advection. Hence, to enforce a minimum distance between two adjacent points, and a minimum angle between 3 points at every time step, points are added to ensure that the line is accurately resolved. Further, since errors in positions can grow exponentially in time, these points need to be added sufficiently early in the simulation.

Lastly, an ensemble averaging method from Ref. [21] which gives us h_{ensemble} is used to

estimate the topological entropy of the flow. The trajectories of a fixed number of points are calculated using n realisations of random seeding for the initial positions. An ensemble average of the topological entropies of the braids generated by the trajectories in each realisation (calculated using the Dynnikov method) is calculated to obtain h_{ensemble}.

2.3 Braiding using "ghost rods"

2.3.1 Replacing physical stirrers with points on periodic orbits

Now, one does not need physical stirrers to produce a braid in a flow field. Braids can be produced by points in the flow that act as barriers to material lines, and the TCNT can be applied to them to predict the characteristics of the flow field. This methodology has been applied successfully to elliptic islands on periodic orbits [18], fixed points in the flow field [8], point vortices in a potential flow [7] and points on aperiodic orbits [28]. The braids thus formed can be analysed to determine the TN representative of the flow mapping much in the same way as for physical stirrers. The following is the description of a "toy" Stokes' flow where points on periodic orbits play the role of physical stirrers. This flow field is used as the reference case for the periodic (in space) lid driven cavity flows in this dissertation.

The 3 "ghost-rod" mixing protocol considered in this study is a two-dimensional, lid-driven cavity flow in the Stokes flow limit, which is the same as in Refs. [9, 1]. This protocol is modeled on the 3 rod-stirrer flow having a pA representative in its isotopy class in Ref. [6], which is similar to one of Fig. 2.3 (b). The braiding in the fluid can be interpreted to be the result of the exact interchange of 3 points ("ghost rods") on period 3 orbits. The domain is a two dimensional rectangle $[-L/2, L/2] \times [-h, h]$, where $L = 12h$. The flow is periodic in x with period L and in time with a period $t = \tau_f^*$.

The flow has an exact mathematical representation and the following description is taken

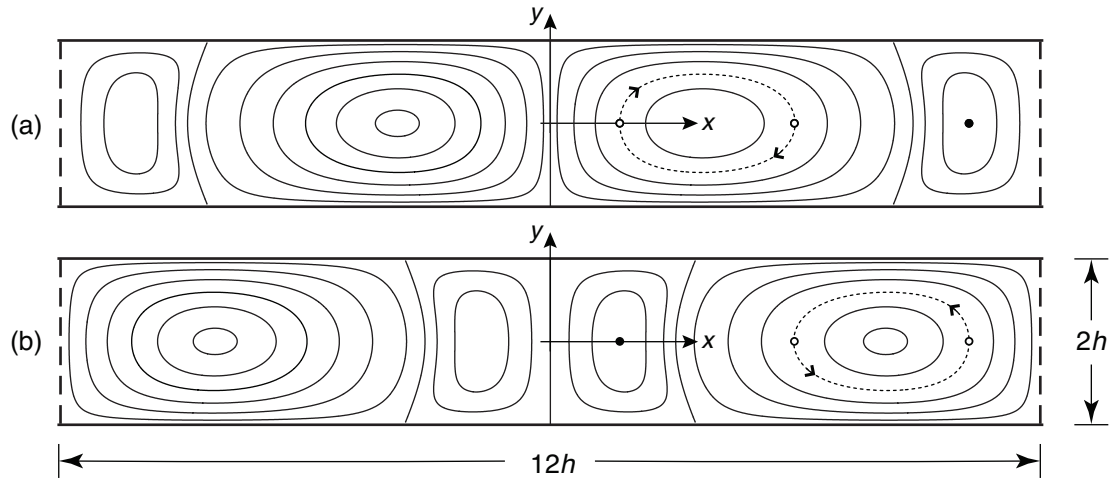

Figure 2.4: [Source: [1], used with permission of Pradeep Rao.] General flow domain, and representative streamlines in the Stokes' flow limit with $U_2/U_1 \simeq 0.8413$ for (a) the first half of the flow period and (b) the second half of the flow period. Filled circles show the stagnation points used to define the flow protocol, and open circles show the points that exchange positions along the dotted streamlines when taking the parameter values $h = 1$, $U_{max} \simeq 1.0$, and $\tau \simeq 15.261$, for the base or reference case.

from Ref. [1]. The equation governing the dynamics of the Stokes' flow is the biharmonic equation for the stream function,

$$\nabla^4 \psi = 0, \tag{2.18}$$

where ψ is the stream function of the flow. ψ is related to the x and y velocity components u and v respectively, through the relations $u = \partial\psi/\partial y$ and $v = -\partial\psi/\partial x$. Now consider the boundary conditions:

$$\begin{aligned} \psi(x, \pm h) &= 0 \\ \frac{\partial \psi}{\partial y}(x, \pm h) &= \pm \sum_{n=1}^{N} U_n \sin(n 2\pi x/L) \\ \psi(x + L, y) &= \psi(x, y). \end{aligned} \tag{2.19}$$

Due to the linearity of Eq. (2.18) and considering the boundary conditions in Eq. (2.19),

the stream function can be written in the form

$$\begin{aligned}\psi(x,y) &= \sum_{n=1}^{N} U_n \psi_n(x,y) \\ &= \sum_{n=1}^{N} U_n C_n f_n(y) \sin(n2\pi x/L). \end{aligned} \tag{2.20}$$

The solution for this (steady) flow is given by

$$f_n(y) = y\cosh(n2\pi h/L)\sinh(n2\pi y/L) - h\sinh(n2\pi h/L)\cosh(n2\pi y/L), \tag{2.21a}$$

$$C_n = 2\left[\sinh(n4\pi h/L) + n4\pi h/L\right]^{-1}. \tag{2.21b}$$

Thus, for a finite value of N, the velocity field is given by a closed-form analytical solution. From this steady flow we generate a time-dependent system consisting of two counter-rotating flow cells contained within $0 \le x \le 6h$ by taking $N = 2$ with the time-periodic boundary conditions

$$\begin{aligned}\frac{\partial \psi}{\partial y}(x, \pm h; t) &= \pm\left[U_1 \sin\left(2\pi\, x/L + \varphi(t)\right) + U_2 \sin\left(4\pi\, x/L + 2\,\varphi(t)\right)\right], \\ \varphi(t) &= \begin{cases} 0 & \text{for } t \in [n\tau_f, (n+1/2)\tau_f), \\ \pi & \text{for } t \in [(n+1/2)\tau_f, (n+1)\tau_f). \end{cases} \end{aligned} \tag{2.22}$$

Thus the flow switches between 2 steady states every half period (i.e. $\tau_f^*/2$), as governed by the applied velocity boundary conditions in Eq. (2.22). The Stokes' flow case is immediately periodic in time, since the time dependence comes only from the boundary conditions (which are periodic in time). The parameters chosen for the base Stokes' flow case are domain half-height $h = 1$ and boundary conditions given by $U_1 \simeq 0.62123$ and $U_2 \simeq 0.52264$ (corresponding to $U_{max} \simeq 1.0$), and $\tau_f = \tau_f^* \simeq 15.261$. These parameter values are chosen so that the points highlighted in Fig. 2.4 exchange positions exactly after $t = \tau_f^*$. Each point returns to its original position after a period $3\tau_f^*$. Note that since there exist vertical

streamlines in the flow at $x = pL/2$, where p is an integer, we need only to study half the domain, i.e. for $0 \leq x \leq L/2$.

The braid formed by the "ghost-rods" in one period is $\sigma_1\sigma_2^{-1}$, which has a dilatation of $\lambda = (3+\sqrt{5})/2$ and topological entropy $h_{\text{braid}} = \log((3+\sqrt{5})/2) \approx 0.962$. The topological entropy of the flow h_{f,τ_f^*} was calculated to be 0.968 [9], which is well represented by the entropy of the braid. Note that if we multiply the boundary conditions in Eq. (2.22) by -1 for $t \in [(n+1/2)\tau_f^*, (n+1)\tau_f^*)$, we obtain an interchange of the points on the periodic orbit corresponding to the braid $\sigma_1\sigma_2$, which has a TN representative that is finite order and is similar to Fig. 2.3(a). Both the pA and the finite-order flow fields are used as the base reference case for the finite Reynolds number simulations in this study.

2.3.2 Replacing points on periodic orbits by almost-cyclic sets

As described in the previous sections, the TCNT is a very powerful tool that can be used to determine the complexity inherent in fluid flows, and predict the degree of chaos and mixing efficiency of flow fields. However, all examples in the previous sections required the presence of physical stirrers, or the identification of points on exactly periodic orbits. This would limit the applicability of the TCNT to more general flows where such points may be absent or very expensive to detect. The entropy of the flow field can be approximated by calculating the entropy of a braid of randomly selected aperiodic trajectories in the flow, but this has shown to be a poor estimate [28].

In Refs. [9, 12], the authors apply the TCNT to the lid driven Stokes' flow described in §2.3.1 based on the presence of almost-cyclic sets (ACS) [29], which are closely related to the almost-invariant sets described in §2.1.1. The authors found that reducing the switching times for the flow led to the destruction of the period 3 orbits that are responsible for producing the pA braid. However, a comparison of stretching rates on non-trivial lines showed that despite a 5% decrease in τ_f below the reference case τ_f^*, h_{TN} from the reference

case still provided a lower bound for h_{f,τ_f^*}. To try and explain this phenomenon, the authors computed the AIS from the second eigenvector $v^{(2)}$ of the reversible matrix $R_{n,\tau}$ as calculated from the descritised Perron-Frobenius operator $P_{n,\tau}$ of the discrete time flow field for the cases with $\tau_f \leq \tau_f^*$. For $\tau_f^* \geq \tau_f \geq 0.95\tau_f^*$, the ACS consist of 3 disjoint coherent structures that move on a braid isotopic to the braid of the points on period 3 orbits in the reference case. Further reducing τ_f leads to splitting of the ACS into 13 disjoint coherent structures on periodic orbits, and the entropy of the flow is bounded below by the entropy of the braid of these structures. The ACS are leaky, in that points within them will eventually move out of them after long times, but they still were shown to provide a very good estimate of the entropy of the flow field through the application of the TCNT.

2.4 Extension of Stokes' flow to finite Reynolds numbers

As mentioned previously, the major focus of this work is to establish the relation between the dynamics of coherent structures in the flow and mixing and transport at non-zero Reynolds numbers. For this we need to solve the Navier-Stokes' equations numerically, as closed form analytical solutions are only available in the Stokes' flow limit. The flow fields considered are two-dimensional lid driven cavity flows, with either periodic boundary conditions or solid walls in the x direction. For both cases, the Navier Stokes' equations are solved using the streamfunction-vorticity formulation.

$$\mathrm{Re}\left(\frac{\partial \omega}{\partial t} + \underline{u}\cdot\nabla\omega\right) = \nabla^2\omega \tag{2.23a}$$

$$\omega = (\nabla\times\underline{u})\cdot\underline{e}_z = -\nabla^2\psi, \tag{2.23b}$$

where $\underline{u} = (u, v)$, and ω is the component of vorticity in the z direction. The advantage of this formulation is that the pressure term is absent in this form, and hence one does not need to implement an iterative algorithm to solve for pressure. The caveat is that boundary conditions are known only for the streamfunction, and not for vorticity. Influence matrix techniques are used to exploit the linearity in the streamfunction-vorticity equation (2.23b) to circumvent this difficulty.

For both cases, the flow field is determined using spectral method algorithms implemented in C++. Spectral methods differ from finite element or finite difference methods in the choice of trial or basis functions [30]. In classical spectral methods, like the one used in this study, a single set of basis functions, obtained through a tensor product of 1-D basis functions, is used for the entire domain. This use of a single set of basis functions affords solutions that are infinitely differentiable [30], unlike spectral element method solutions, which are composed of multiple sets of basis functions that are globally C^0 continuous. The use of spectral methods affords exponential spatial convergence [31]. This enables accurate tracking of passively advected particles in the flow using a 4th order Runge Kutta scheme and helps mitigate the exponential growth of small errors in particle trajectories due to their chaotic nature. Particle tracking is required to compute the AIS (see section 2.1.1), as well as to determine mixing efficiency (see section 3.3).

Note that for a finite Reynolds number, the flow field is not immediately periodic in time when starting from a state of rest. The flow fields considered for all cases studied in the current work are those that develop after time $n^*\tau$, where n^* is the number of periods after which the flow field becomes periodic in time. Refer to Fig. 2.5 (a) for the values of n^* for different Reynolds numbers.

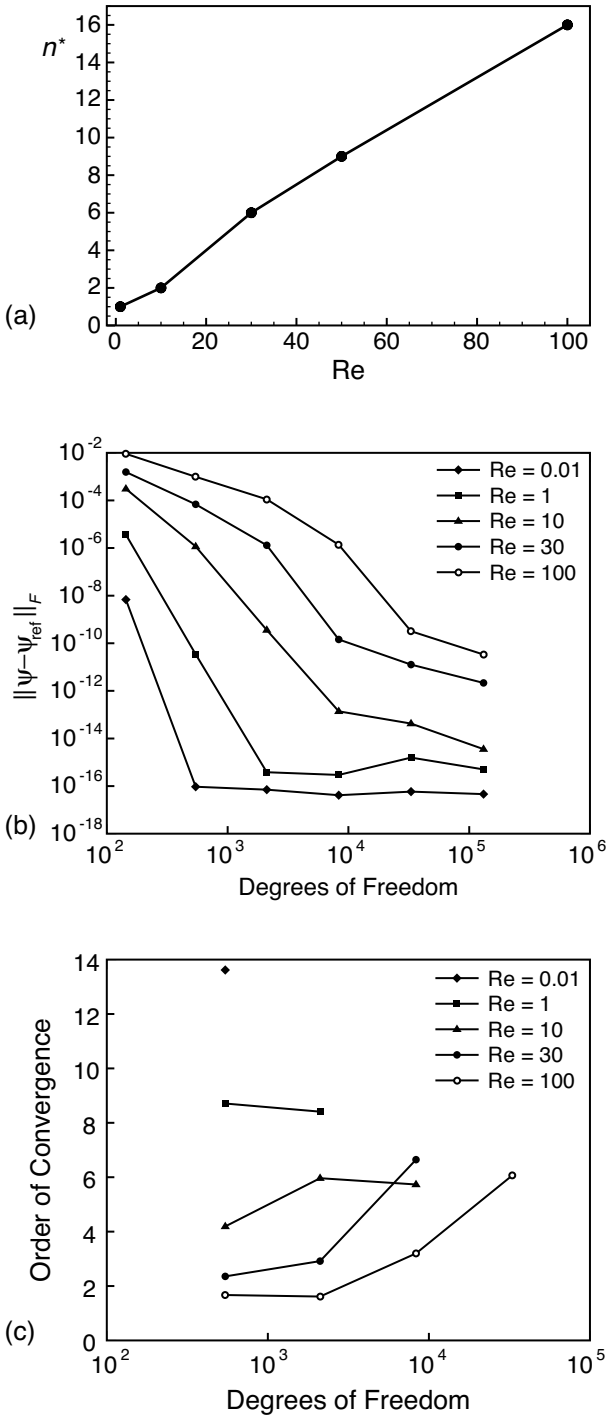

Figure 2.5: [Source: [1], used with permission of Pradeep Rao.] (a) Flow period n^* at which the bulk flow becomes periodic in time, (b) spectral convergence of the stream function, and (c) order of convergence. Since the convergence is geometric for a spectral method instead of algebraic, the order of convergence (rate) varies with degrees of freedom, and often machine precision is reached.

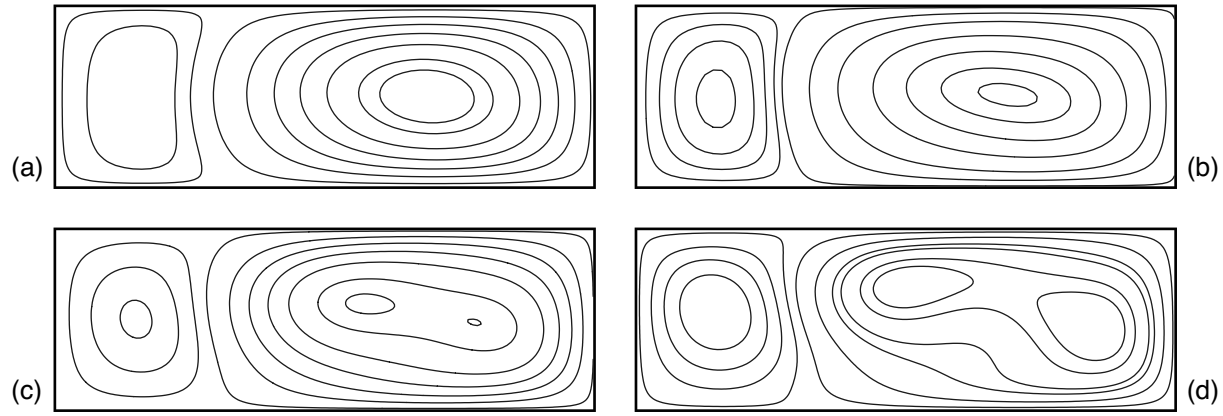

Figure 2.6: [Source: [1], used with permission of Pradeep Rao.] Instantaneous streamlines at time $t = n^*\tau$, i.e. at the end of an advection cycle, once the flow has become periodic for Re = (a) 10, (b) 30, (c) 50 and (d) 100

2.4.1 Fourier-Chebyshev method

As in the analytical solution, the two-dimensional flow field is described by a stream function $\psi(x, y, t)$, which enforces a divergence free velocity field. Since the flow domain under consideration is periodic in the x direction, the spectral basis of choice is the Fourier series. In the y direction the Chebyshev approximation is applied, which gives good near-wall resolution and fast transforms [30]. The use of the Fourier-Chebyshev formulation for the vorticity-streamfunction form of the incompressible Navier Stokes equations is well established [32, 31]. The solution sought for any field variable in a domain which is periodic in x

with a period of L is of the form

$$\psi(x,y,t) = \sum_{m=0}^{M} \sum_{k=-K/2}^{K/2-1} \hat{\psi}_{mk}(t)\, T_m(y)\, e^{ik\,2\pi x/L}, \tag{2.24a}$$

$$\omega(x,y,t) = \sum_{m=0}^{M} \sum_{k=-K/2}^{K/2-1} \hat{\omega}_{mk}(t)\, T_m(y)\, e^{ik\,2\pi x/L}, \tag{2.24b}$$

$$u(x,y,t) = \sum_{m=0}^{M} \sum_{k=-K/2}^{K/2-1} \hat{u}_{mk}(t)\, T_m(y)\, e^{ik\,2\pi x/L}, \tag{2.24c}$$

$$v(x,y,t) = \sum_{m=0}^{M} \sum_{k=-K/2}^{K/2-1} \hat{v}_{mk}(t)\, T_m(y)\, e^{ik\,2\pi x/L}, \tag{2.24d}$$

where $\hat{\cdot}_{mk}(t)$ are the unknown coefficients and $T_m(y) = \cos(m\cos^{-1}(y))$ are the Chebyshev basis functions. Recall that x and y are normalized by h, so that $-1 \le y \le 1$ as required by this formulation. The total number of terms, $M \times K$, representing each field variable is referred to as the resolution of the approximation.

Substituting the spectral approximations for the field variables into Eqn. (2.23) results in

$$\sum_{m=0}^{M} \sum_{k=-K/2}^{K/2-1} \left[\frac{\partial \hat{\omega}_{mk}}{\partial t} + \hat{Q}_{mk} \right. \tag{2.25a}$$

$$\left. - \frac{1}{Re}\left(\hat{\omega}^{(2)}_{mk} - (2\pi k/L)^2 \hat{\omega}_{mk}\right)\right] T_m(y)\, e^{ik\,2\pi x/L} = 0,$$

$$\sum_{m=0}^{M} \sum_{k=-K/2}^{K/2-1} \left[\hat{\psi}^{(2)}_{mk} - (2\pi k/L)^2 \hat{\psi}_{mk} + \hat{\omega}_{mk}\right] T_m(y) e^{ik\,2\pi x/L} = 0, \tag{2.25b}$$

where the superscript $^{(2)}$ refers to the matrix corresponding to the second derivative operator of the Chebyshev polynomial, and where

$$\sum_{m=0}^{M} \sum_{k=-K/2}^{K/2-1} \hat{Q}_{mk}\, T_m(y)\, e^{ik\,2\pi x/L} = \underline{u} \cdot \nabla \omega \tag{2.26}$$

is the spectral projection of the non-linear terms in Eqn. (2.23a). By applying the orthog-

onality of the Fourier basis and the Chebyshev basis to Eqn. (2.25a), $M \times K$ sets of 1-D transient equations for vorticity and $M \times K$ algebraic equations for the streamfunction are obtained. As in [31], the vorticity equations are discretized in time, with time step δt, using the semi-implicit Adams-Bashforth/Backward-Differentiation Scheme (AB/BDI2), where the linear (diffusive) terms are solved implicitly using a 2nd order Backward-Differentiation scheme, and the nonlinear (convective) terms are treated using an explicit Adams-Bashforth formulation

$$\hat{\omega}_{mk}^{(2)^{n+1}} - \left((2\pi k/L)^2 + \frac{3\mathrm{Re}}{2\delta t} \right) \hat{\omega}_{mk}^{n+1} = \frac{\mathrm{Re}}{2\,\delta t} \left[-4\hat{\omega}_{mk}^{n} + \hat{\omega}_{mk}^{n-1} \right] + \mathrm{Re} \left[2\hat{Q}_{mk}^{n} - \hat{Q}_{mk}^{n-1} \right], \tag{2.27a}$$

$$\hat{\psi}_{mk}^{(2)} - (2\pi k/L)^2 \hat{\psi}_{mk} = -\hat{\omega}_{mk}. \tag{2.27b}$$

To solve this system, four boundary conditions are required. Using a Lanczos-Tau formulation [33], the two boundary conditions given in Eqn. (2.22) are applied for the streamfunction, and the remaining two boundary conditions given in Eqn. (2.19) are integrated into the vorticity equation through the influence matrix technique [31]. The boundary velocities are changed instantaneously at the end of each half of a flow cycle, just as in the Stokes' flow case.

In each case the flow is taken to be initially at rest. Unlike the Stokes' flow case, the presence of inertial effects prevents the flow from immediately becoming periodic in time. The number of cycles needed for the flow to become periodic, denoted here by n^*, increases with the Reynolds number of the flow, as shown in Fig. 2.5(a). In Fig. 2.6 we show instantaneous streamlines at time $t = n^*\,\tau$, a pattern that then repeats every flow period. Two counter-rotating flow cells similar to those in the Stokes' flow case are evident for $\mathrm{Re} \leq 30$. For $\mathrm{Re} > 30$ (for cases tested), inertial effects begin to develop a more complicated flow pattern, with the larger flow cell splitting into two smaller co-rotating cells.

To ensure that the solutions are independent of the resolution used, the solutions obtained at different resolutions ($M \times K = 9 \times 16,\ 17 \times 32,\ 33 \times 64,\ 65 \times 128,\ 129 \times 256$, and 257×512) were interpolated onto an evenly spaced 100×600 spatial grid and compared at these points with a reference solution obtained at a resolution of $M \times K = 513 \times 1024$. The plot of the Frobenius norm, $||\cdot||_F$, of the difference in these stream function values is shown in Fig. 2.5(b) for Re $= 0.01, 1, 10, 30$ and 100. Each case attains a geometric convergence rate, which shows that the flow is well resolved. The final resolutions $M \times K$ used to obtain the velocity fields for our analysis were 33×64 for Re ≤ 1, 65×128 for Re $= 10$, and 129×256 for Re > 10.

2.5 Mixing metrics

To determine the mixing efficiency of a flow field, we use mixing metrics based on the advection of N_p passive particles in the flow. The domain is binned into N_b equally sized boxes having sides of size $s = 2N_p^{-1/2}$. This scaling is chosen to ensure that for a perfectly random distribution of particles, at least 98% of the bins would contain at least one particle. Particles are advected in the flow starting from an initial distribution (eg. evenly distributed along $y = 0$), and mixing is tracked based on the number of particles contained in the i^{th} bin, η_i. The first two measures taken from Ref. [34] are defined by

$$\epsilon_{\eta^*} = \frac{1}{N_b} \sum_{i=1}^{N_b} w_i, \tag{2.28a}$$

$$\text{with} \quad w_i = \begin{cases} \eta_i/\eta^* & \text{if } \eta_i < \eta^*, \\ 1 & \text{if } \eta_i \geq \eta^*. \end{cases} \tag{2.28b}$$

By taking $\eta^* = 1$ we get the *spreading index* ϵ_1 which gives us the fraction of bins that contain at least one particle. A good mixing protocol will lead to all bins containing at least

one particle and thus $\epsilon_1 \to 1$ as $t \to \infty$. Setting $\eta^* = N_p/N_b$ in Eq. (2.28) we get the *homogenisation index* where the weighting w_i penalises bins with less than η^* particles, and thereby favours a homogenous system.

The third mixing measure used in this study is the *variance of concentration measure* [35] which is calculated using the relation

$$\sigma = \frac{1}{N_b} \sum_{i=1}^{N_b} (\eta_i - \eta^*)^2, \tag{2.29}$$

with $\eta^* = N_p/N_b$. This measure penalises bins for both $\eta_i > \eta^*$ and $\eta_i < \eta^*$. For a completely homogenous system, $\sigma \to 0$. These metrics provide a measure of how well mixed the system is at any given point in time but do not directly give us a mixing rate. To calculate mixing rate, we do a regression curve fit of the time series evolution of either ϵ_1 or ϵ_{η^*} with the equation

$$\epsilon = 1 - \exp(-r(t - c)) \tag{2.30}$$

where r is the mixing rate exponent, and c is the time after which the exponential increase in mixing is seen after the inital ramp-up phase.

2.6 Mixing results obtained by ramping up the Reynolds number using the reference flow parameters

The "3 ghost-rod" mixing protocol described in §2.3.1 achieves efficient mixing due to the exponential stretching of material lines as predicted by the TCNT, as the braid due to the elliptic points has a pA representative in its isotopy class. It is of interest to know if the same protocol would achieve efficient mixing in the case of a non-zero Reynolds number where inertial effects can not be neglected, using the same boundary conditions as in the reference Stokes' flow case. This could extend the use of similar protocols and the application

of the TCNT to a wider range of real flows and applications.

Rao et. al [1] studied the mixing efficiency of this protocol for a range of Reynolds numbers from 0.1 to 100. They found that ramping up the Reynolds number whilst keeping all other flow parameters, such as the flow period and the boundary conditions, the same, led to a destruction of periodic islands associated with the elliptic points on period-3 orbits for Re > 1. The best mixing rates were observed for Re ≈ 10, and the mixing results were identical for all cases with Re ≤ 1. Increasing the Reynolds number above 10 led to a decrease in mixing efficiency despite the flow structure being more complicated. The poorest overall mixing rates were observed for Re $= 30$. Even in this case, however, a fairly homogenous distribution of passive particles was seen after 20 flow cycles, except for 2 islands in the flow. For further details please see Ref. [1].

Chapter 3

Almost invariant sets, topological entropy and mixing

3.1 AIS and for the perturbed 3 "ghost-rod" mixing protocol at finite Re.

In Ref. [1] the authors speculated that the decreased mixing efficiency observed for Re > 10 could be due to the destruction of almost invariant sets that form a pA braid in the flow field, based on the conclusions of Ref. [9]. To test this hypothesis, the AIS for Re = 1, 10, 30 and 50 have been computed using the procedure outlined in §2.1.1.

To numerically estimate the transfer operator (or transfer matrix) $P_{n,\tau}$ and associated matrices $\hat{P}_{n,\tau}$ and $R_{n,\tau}$ for this study, we bin the domain into $240 \times 80 = 19200$ square boxes, evenly distribute 400 particles in each box, and follow the procedure outlined in §2.1.1. These particles are passively advected in the flow field both forward and backward in time using a 4th order Runge Kutta time integration scheme and previously calculated time-periodic velocity fields, for one period. The velocity fields ($u(x, y)$ and $v(x, y)$) are stored in the form

of coefficients of Fourier-Chebyshev series expansions at every time step, and are calculated using the procedure outlined in §2.4.1. For each case, the vorticity-streamfunction form of the Navier Stokes' equations are solved starting from a state of rest at $t = 0$. After a minimum of n^* periods have passed (to ensure that the velocity field has become periodic in time), the velocity field at every time step in one period is stored. The velocity at any point in the domain can then be determined with spectral accuracy using Eq. (2.24)(c,d).

The eigenspectrum of the reversible matrix $R_{n,\tau}$ (eq. (2.11)) indicates the various AIS present in the system as discussed in §2.1.1. Since the entire domain maps to itself, the first eigenvector $v^{(1)}$ corresponds to the entire domain, and the corresponding eigenvalue $\lambda^{(1)} = 1$, since the flow map is area preserving. Thus the dynamics of the flow in the domain is dominated by the subsequent AIS. The AIS are isolated by the near zero contours of the eigenvectors from $v^{(2)}$ onwards, and the magnitude of the corresponding eigenvalues give a measure of the invariance or "leakiness" of the AIS [15]. Note that the eigenvectors are ordered with decreasing magnitude of the corresponding eigenvalues. The different AIS may correspond to different regions in the flow field, but the AIS corresponding to eigenvectors after $v^{(2)}$ should in theory have less of an effect on the dynamics of the flow, since they are more "leaky".

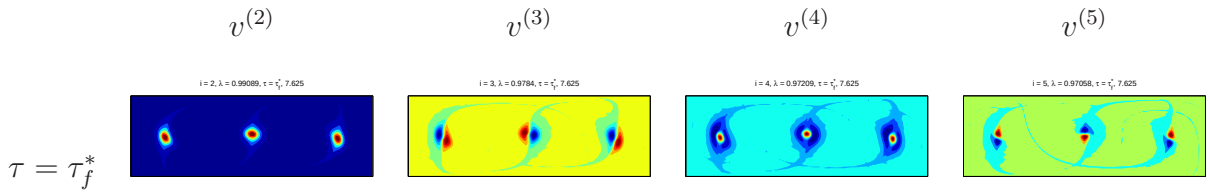

Figure 3.1: Contour plots of eigenvectors of the reversible matrix for Re = 1

In the Stokes' flow case, with the reference case parameters described in §2.3.1, there exist 3 points on period 3 orbits as shown in Fig. 2.4. The Poincaré section for this case shows 3 islands corresponding to these elliptic points. As the Reynolds number is ramped up keeping all other parameters the same, these islands are no longer discernable, even though the basic 2 counter-rotating cell flow structure persists, which seems to suggest the destruction of

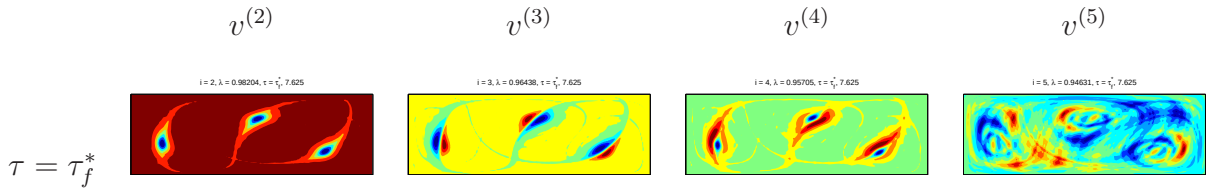

Figure 3.2: Contour plots of eigenvectors of the reversible matrix for Re = 10

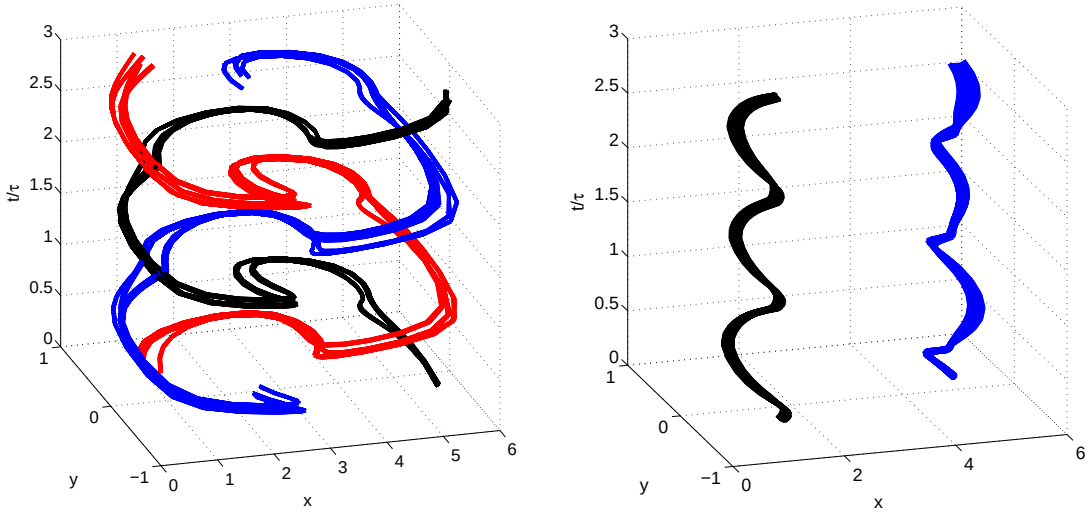

(a) (b)

Figure 3.3: (a) The trajectories of period 3 of the AIS corresponding to $v^{(2)}$ for the case $\tau = 1.2\tau_f^*$ which braid in a pA fashion, (b) The trajectories of period 1 of the AIS corresponding to $v^{(2)}$ and $v^{(3)}$ for the case $\tau = 1\tau_f^*$,Both figures are for Re = 30.

the period 3 elliptic orbits. This could be explained by the fact that due to inertia, points in the flow will take longer to traverse the same distance along streamlines (which are no longer constant during one half advection cycle). The now apparently non-existent elliptic points on exact period-3 orbits are replaced by ACS on period-3 orbits in some cases (for example, Re = 10 with $\tau = \tau_f^*$). This phenomenon can be observed in the contour plots of the eigenvectors of the reversible matrix for various Reynolds numbers in Figures 3.1 to 3.5.

As can be seen from Figures 3.1 and 3.2 the most dominant eigenvector $v^{(2)}$ for Re = 1 and Re = 10 respectively show the presence of 3 coherent structures on period-3 orbits, whose

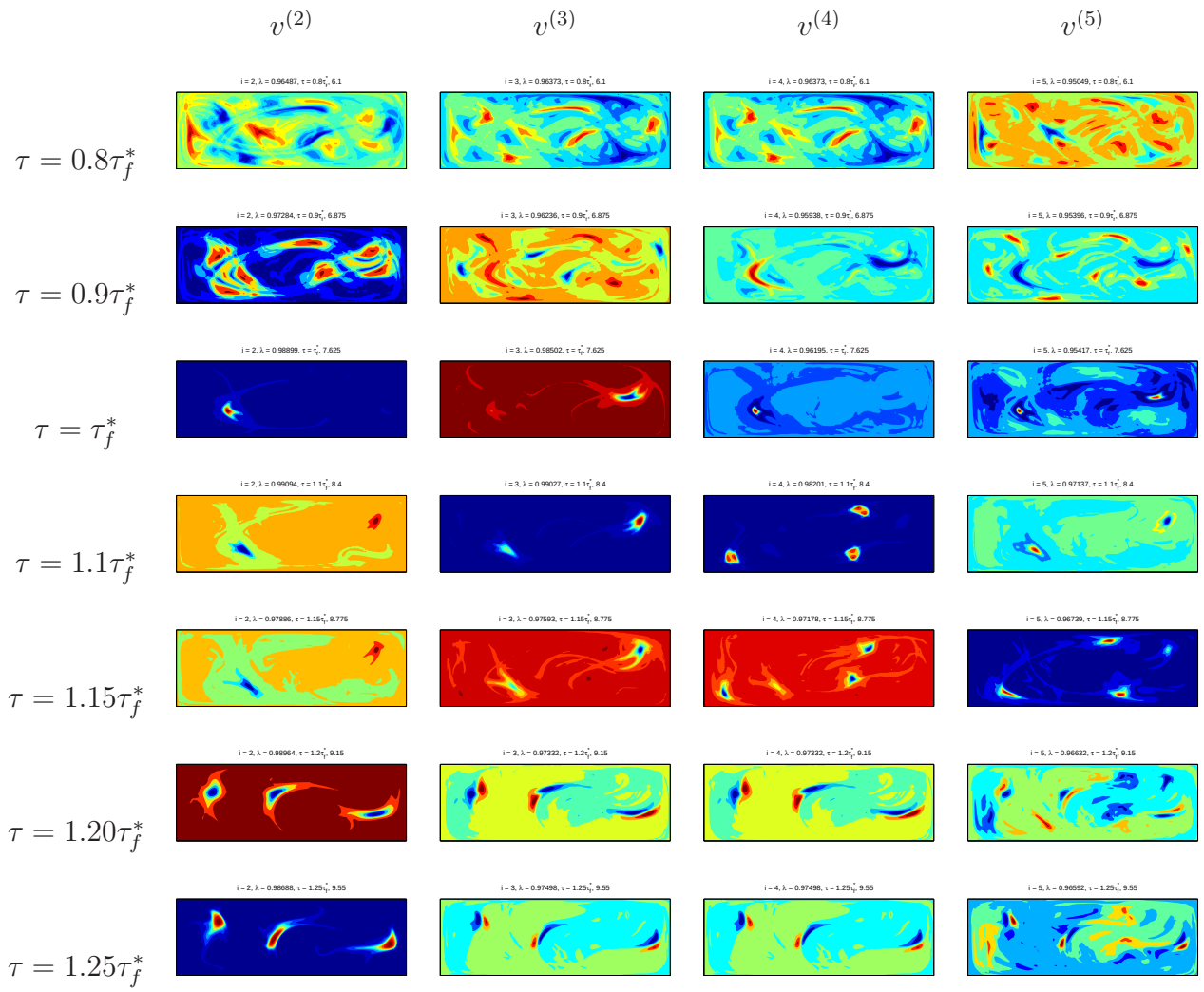

Figure 3.4: Contour plots of eigenvectors of the reversible matrix for Re = 30, for various switching periods

braid is mathematically of pA type (see Fig. 3.3 (a) for a representation of this braid). These coherent structures on period 3 orbits appear to be dominant features of the flow field for Re = 1 and Re = 10 as they show up in eigenvectors further down in the eigen spectrum as well. It can be hypothesized that the good mixing rates observed for Re = 10 in Ref. [1] are associated with the exponential stretching produced by this pA braid. For Re = 30, as seen from Figs. 3.4(b,c), the two most dominant AIS for $\tau = \tau_f^*$ correspond to two distinctly different coherent structures that move on separate period-1 orbits. The trajectories of these structures are depicted in Fig. 3.3(b). As is evident from the trajectories, the AIS do not

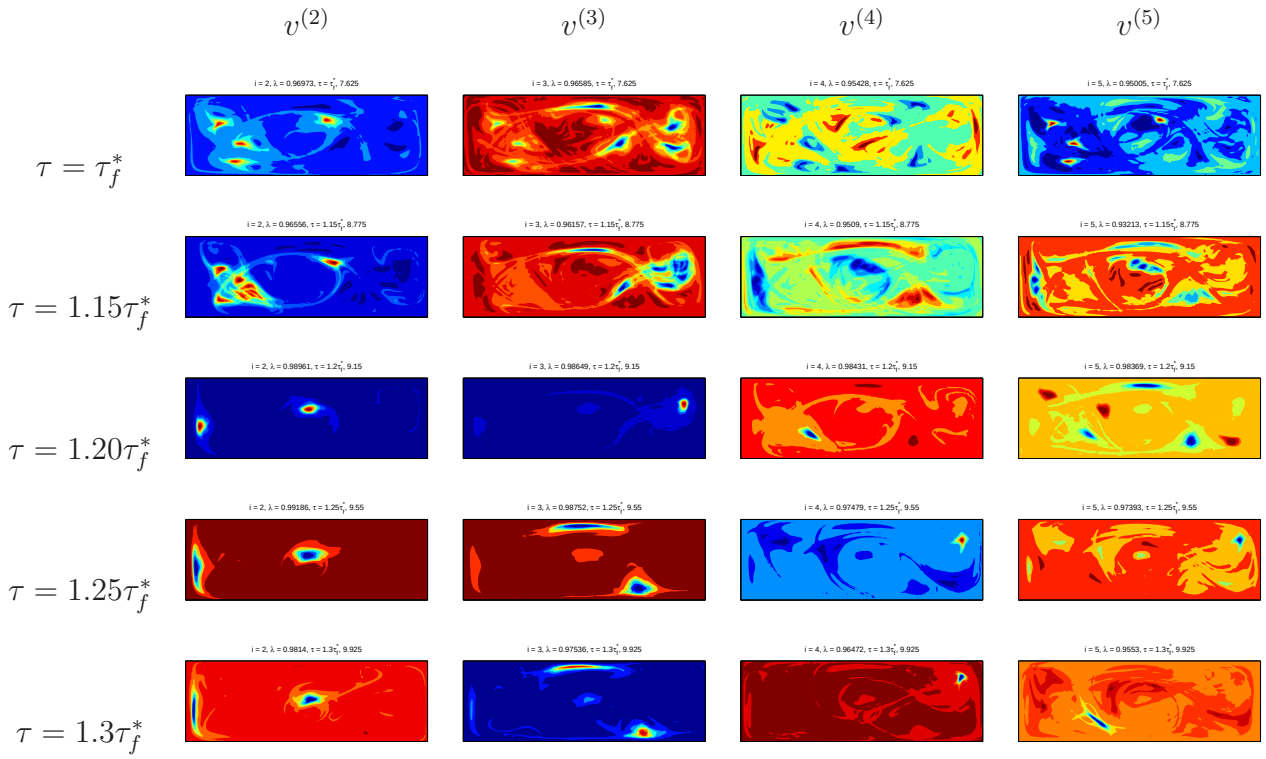

Figure 3.5: Contour plots of eigenvectors of the reversible matrix for Re = 50, for various switching periods

venture out of the half of the domain they start in, and therefore do not braid around each other. One could hypothesize that this is the cause of poor mixing observed for the Re = 30 case as compared to Re $\leq$ 10 in Ref. [1], although this is mostly not the case as we shall see in the next section.

Assuming that the disappearance of coherent structures on period-3 orbits with increasing Re is due to increasing inertial effects, it follows that increasing the period of the flow could lead to the reappearance of these structures. Indeed, as the period of the flow is increased for Re = 30, the AIS corresponding to coherent structures on period 3 orbits become more dominant. As seen in Fig. 3.4 for $\tau = 1.1\tau^*$ and $\tau = 1.15\tau^*$, we find such AIS corresponding to $v^{(4)}$. For $\tau = 1.2\tau^*$ and $\tau = 1.25\tau^*$, these period-3 structures are the most dominant AIS and correspond to $v^{(2)}$. The braid corresponding to these AIS is depicted in Fig. 3.3(b) and is identical to the braid of the points on period 3 orbits in the base Stokes' flow case, which

cause exponential stretching and folding of material lines in the fluid. Note that for $\tau \leq \tau_f^*$ for Re = 30, such structures are not clearly evident even in the first 16 eigenvectors of $R_{n,\tau}$. Similarly for Re = 50, we observe AIS that are sets of 3 coherent structures in the contour plots of $v^{(5)}$ for $\tau = 1.2\tau_f^*$ and $v^{(4)}$ for $\tau = 1.25\tau_f^*$ (see Fig. 3.5).

3.2 Relation between AIS and topological entropy for Re = 30

A line tracking algorithm is used to calculate the asymptotic growth rate of a non-trivial line in the flow field to estimate the entropy (h_{f,τ_f^*}) of the flow, as described in §2.2. To do so, a set of points along $y = 0$ at time $t = 0$ is advected with the flow using a fourth order Runge Kutta algorithm and previously calculated velocity fields.

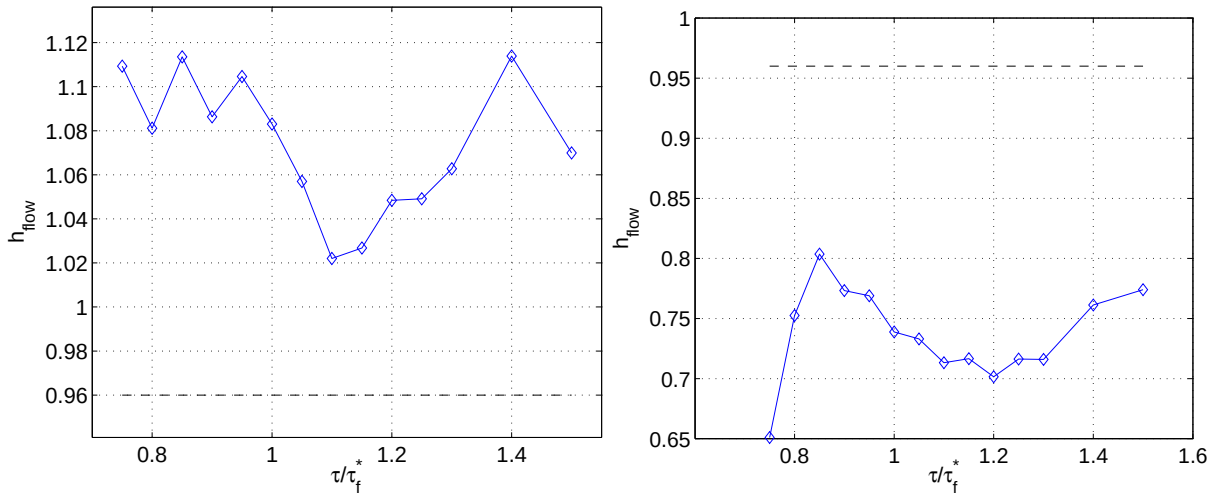

Figure 3.6: Topological entropy of the flow as a function of the flow period τ for Re = 30 for the flow fields based on the (a) pA mixing protocol and (b) the finite order mixing protocol obtained by tracking the stretching of a non-trivial line in the flow for 6 flow periods. The dashed line is the topological entropy of the pA braid on 3 strands.

Figures 3.6 (a) and (b) show the topological entropy of the flow at Re = 30 calculated using

the above method, as a function of the flow period τ, for the flows based on pA and finite order cases respectively. Note that the topological entropies are normalised using the flow period of the reference case to be able to make a fair comparison across different flow periods using the relation

$$h_{f,\tau_f^*} = \frac{\tau_f^*}{\tau}\ln(\lambda). \tag{3.1}$$

The dilatation λ is calculated as the average stretching factor over flow periods 4 to 6. We find that h_{f,τ_f^*} is always well above h_{TN} predicted by the PA braid for the flow based on the pA case, and always well below for the flow based on the finite order case. Also, we see in Fig. 3.6 (a) that, unlike as one would expect from the AIS in Fig. 3.4, h_{f,τ_f^*} for $1.15\tau_f^* \leq \tau \leq 1.25\tau_f^*$ is lower than that for $\tau = \tau_f^*$. Assuming that braiding of material lines in the flow is due to the motion of AIS [9], this would indicate that looking at just the most dominant eigenvector of $R_{n,\tau}$, as was done in Ref. [9], does not predict a sufficiently tight lower bound on the complexity in the flow field for non-zero Reynolds numbers. Thus, for generic flows with a reasonable amount of complexity, information from multiple eigenvectors of $R_{n,\tau}$ needs to be combined to better understand the dynamics of transport in the flow field. This is a significant result, and this thesis focuses on identifying the most significant AIS in such flows in terms of the dynamics of transport.

3.3 Comparison of mixing efficiency with topological entropy of the flow

To calculate the mixing efficiency of the flow, the box counting method proposed in Ref. [34] and described in §3.3 is used. The domain is binned into $240 \times 80 = 19200 = N_b$ boxes, and $N_p = N_b \times 4 = 76800$ particles are uniformly distributed along $y = 0$ at time zero. The particles are advected in time using a fourth order Runge Kutta algorithm and previously calculated velocity fields. The results for all three mixing measures discussed previously are

shown for both the pA and the finite order cases for Re = 1, 10, 30 and 50 in figures 3.7, 3.8, 3.9 and 3.10 respectively. For these studies, the flow fields used are periodic in time. That is the velocity fields used for the advection of passive particles are those that develop after time $n^*\tau$. Refer Fig. 2.5 (a) For the values of n^* for different Reynolds numbers.

For all Reynolds numbers, the flow fields based on the pA reference case outperform the flow fields based on the finite order case in terms of mixing rates with respect to all mixing measures. Further, the spread between the best and worst performing case for different switching periods reduces with increasing Reynolds numbers. This seems to indicate that as inertial effects become more important, the mixing efficiency is less sensitive to changes in boundary conditions if the energy input to the system remains constant.

One would expect that flow fields with the highest normalised h_{f,τ_f^*} would also have the best mixing rates, with the reverse also being true. However, a comparison of Fig. 3.6 with Fig. 3.9 reveals that this correspondence between h_{f,τ_f^*} and mixing is not necessarily the case. For example, the pA case with $\tau = 1.4\tau_f^*$ has among the highest normalised h_{f,τ_f^*}, but is among the poorest performers in early and mid times with respect to both ϵ_1 and ϵ_2 measures. Also, the pA case with $\tau = 1.1\tau_f^*$ achieves amongst the best mixing rates with respect to the ϵ_1 and ϵ_2 measures, but has the lowest h_{f,τ_f^*}.

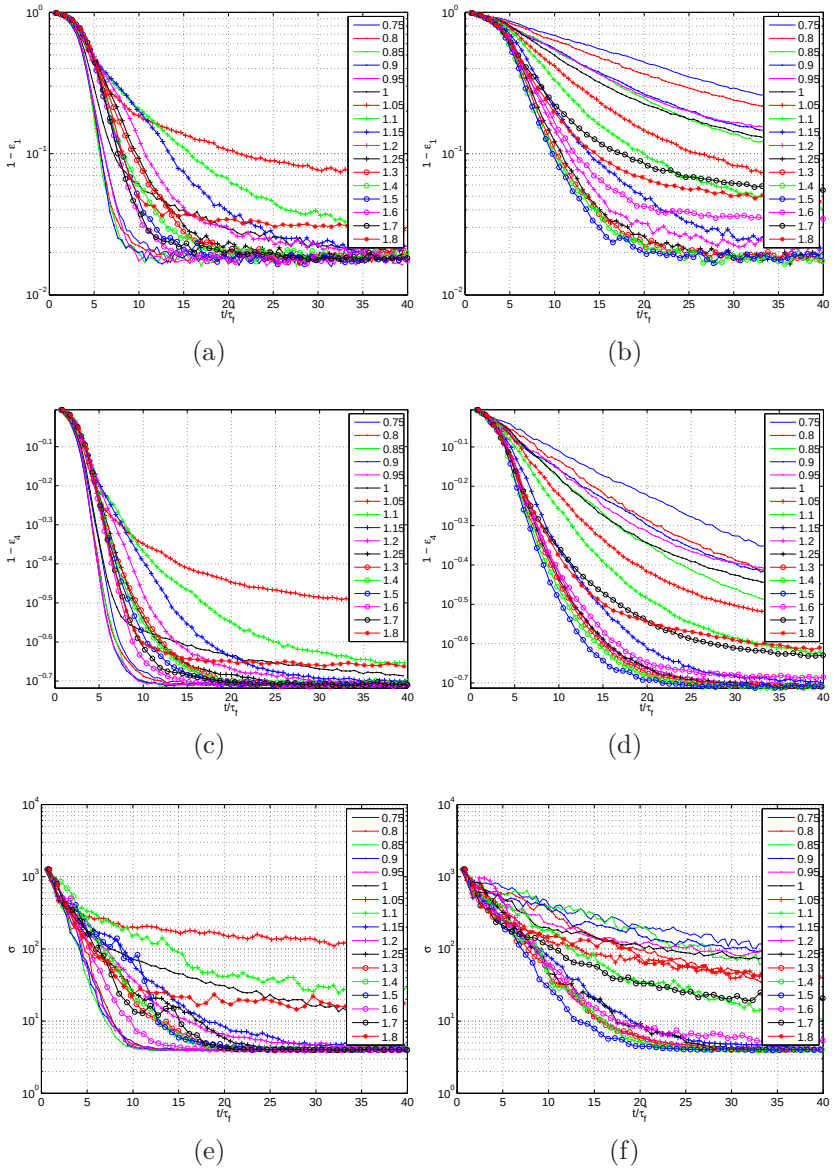

Figure 3.7: Re = 1: Plots show the evolution of the spreading index $1-\epsilon_1$, the homogeneity index $1-\epsilon_4$ and variance of concentration σ with time from top to bottom for various switching periods τ. Lower values indicate better mixing. The figures on the left are for the pA case and the ones on the right are for the finite order case. As can be seen, the pA cases achieve better mixing overall as compared to the finite order cases.

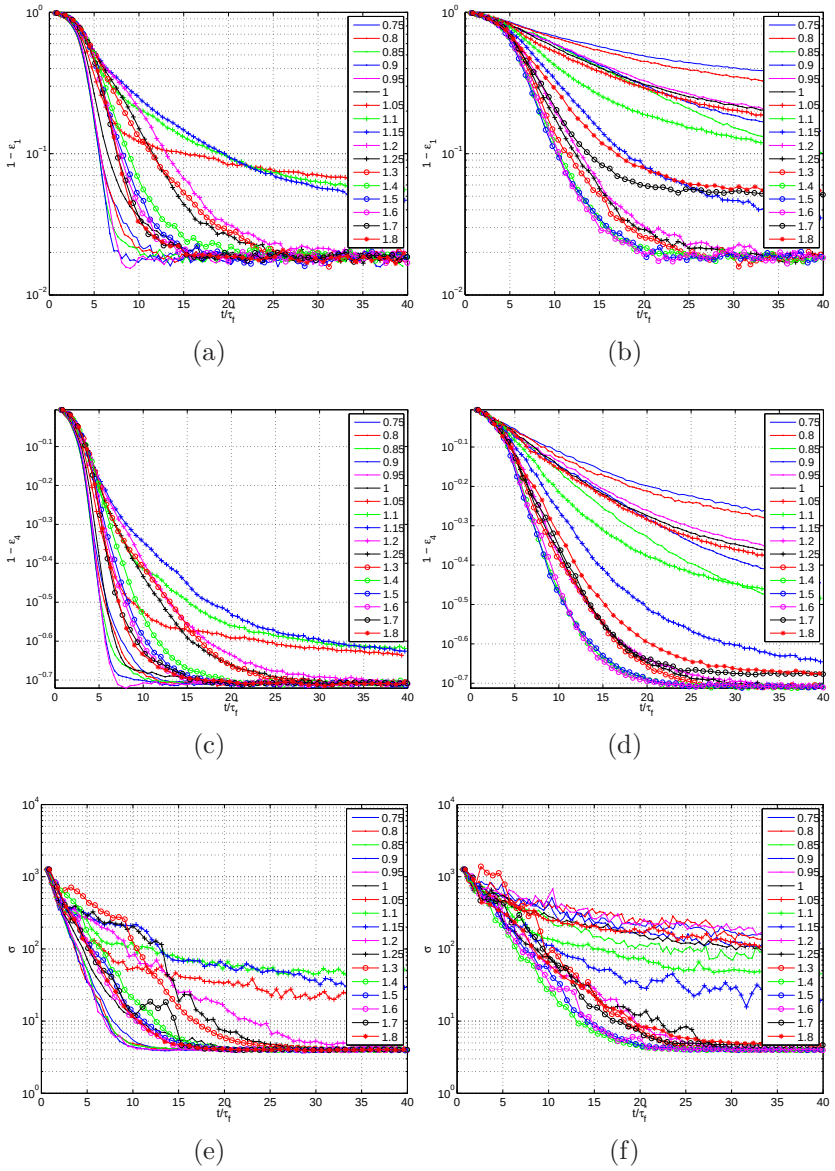

Figure 3.8: Re = 10: Plots show the evolution of the spreading index $1-\epsilon_1$, the homogeneity index $1-\epsilon_4$ and variance of concentration σ with time from top to bottom for various switching periods τ. Lower values indicate better mixing. The figures on the left are for the pA case and the ones on the right are for the finite order case. As can be seen, the pA cases achieve better mixing overall as compared to the finite order cases.

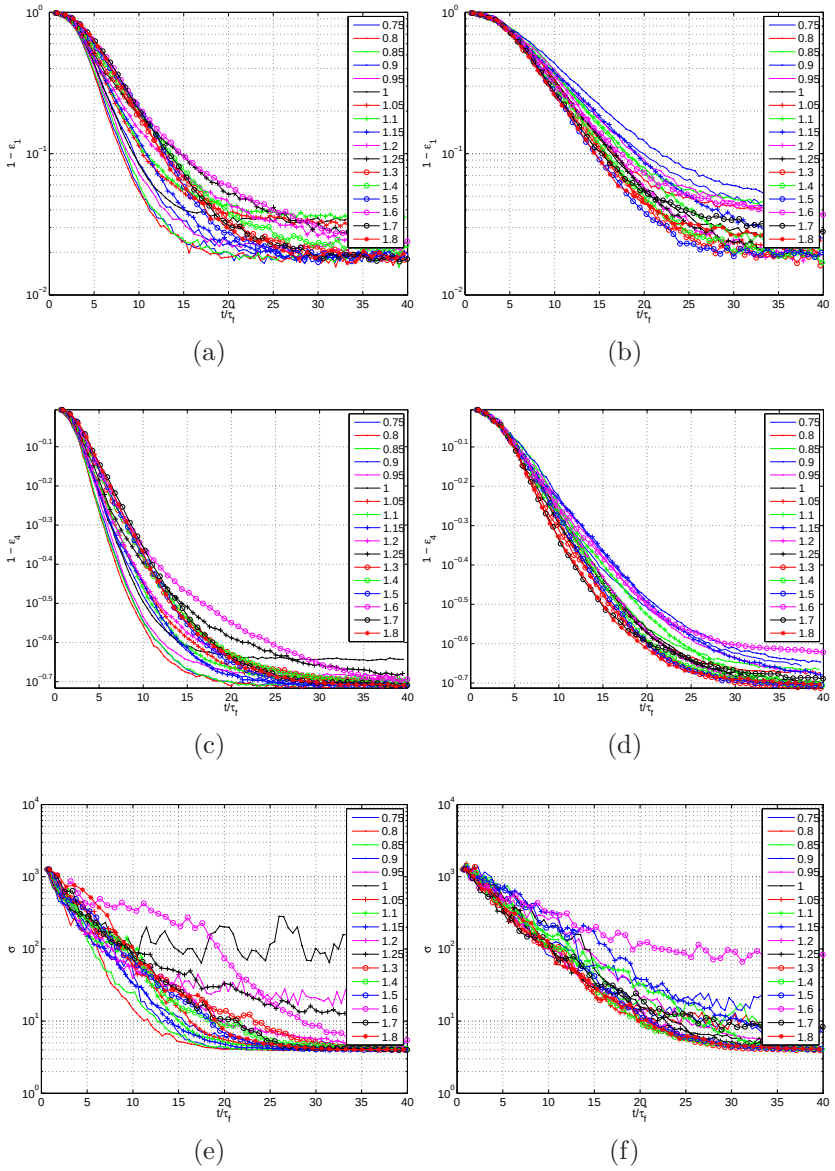

Figure 3.9: Re = 30: Plots show the evolution of the spreading index $1-\epsilon_1$, the homogeneity index $1-\epsilon_4$ and variance of concentration σ with time from top to bottom for various switching periods τ. Lower values indicate better mixing. The figures on the left are for the pA case and the ones on the right are for the finite order case. As can be seen, the pA cases achieve better mixing overall as compared to the finite order cases.

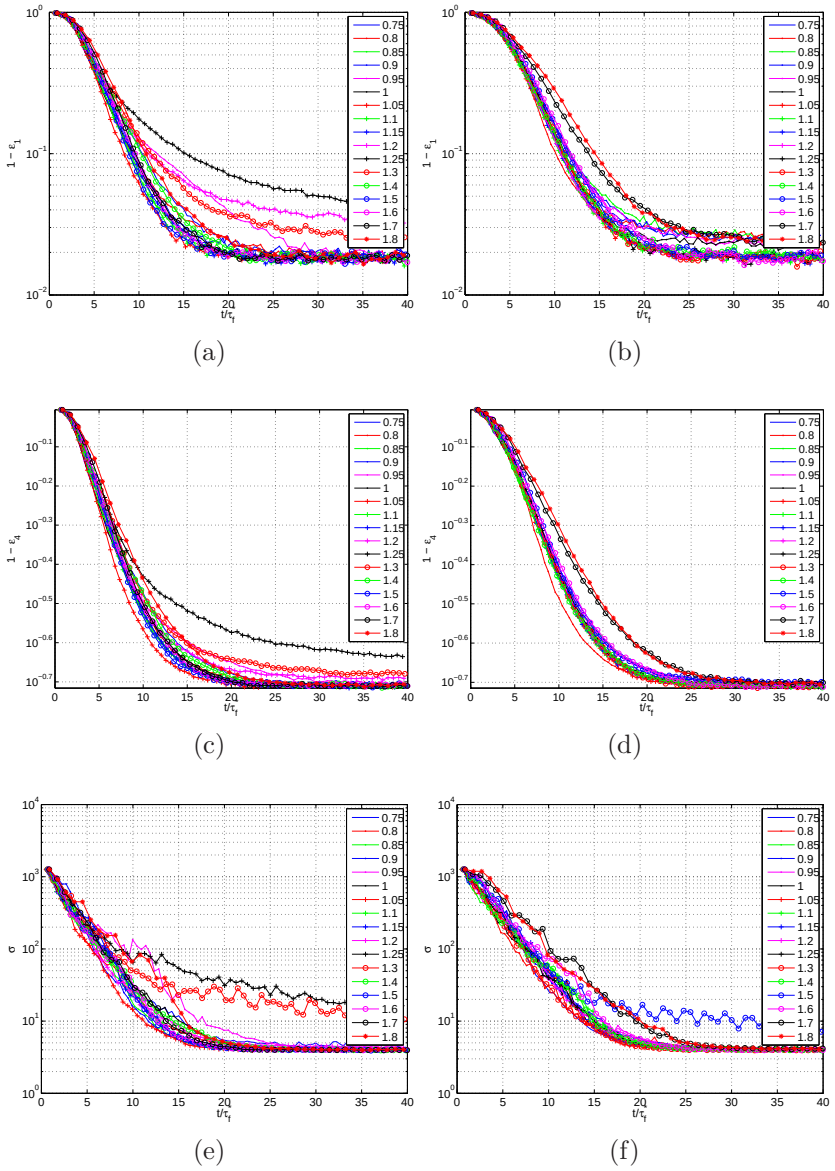

Figure 3.10: Re = 50: Plots show the evolution of the spreading index $1-\epsilon_1$, the homogeneity index $1-\epsilon_4$ and variance of concentration σ with time from top to bottom for various switching periods τ. Lower values indicate better mixing. The figures on the left are for the pA case and the ones on the right are for the finite order case. As can be seen, the pA cases achieve better mixing overall as compared to the finite order cases.

The correspondence between topological entropy and mixing rates is made clearer in Fig. 3.11. This figure compares h_{fluid} with the mixing rate exponents for ϵ_1 and ϵ_2 calculated using the method outlined in §2.5. Some of the peaks in h_{fluid} do not correspond to peaks in the mixing rates, and similarly some of the troughs in h_{fluid} do not correspond to troughs in the mixing rates.

This lack of correspondence occurs in some cases because there are not 1 but 3 factors that determine the mixing efficiency of the system. The first is the topological entropy of the flow, and therefore the stretching rate; the second is the extent of the region over which this exponential stretching is observed; and the third is the leakiness of the AIS. Recall from §2.2 that the TCNT does not predict the size of the region over which material lines stretch exponentially by a factor of λ, and in theory this could be a region of measure zero. Thus, if the size of this region is small compared to the domain (which could correspond to the AIS/ACS being large), the overall mixing achieved by the flow will be poor in spite of the flow exhibiting a high h_{f,τ_f^*}. Further, since the AIS are by definition almost invariant, they are regions of poor mixing and therefore are barriers to transport. The leakiness of the AIS is determined by the magnitude of the eigenvalue as described in §2.1.1. This plays an important role in long time behaviour. Fig. 3.12 compares the magnitude of $\lambda^{(2)}$ of the reversible matrix $R_{n,\tau}$ with the value of $1-\epsilon_1$ after 40 base flow periods for all the Reynolds number cases considered. For the majority of cases a high value of $\lambda^{(2)}$ corresponds to a high value of $1-\epsilon_1$, which indicates a higher number of bins in which there are zero particles. Thus, for good mixing we require that the braiding of the AIS produce exponential stretching in most of the domain, the region occupied by the AIS be small, and the corresponding eigenvalues have low values. The results from this section are consistent with the observations made in Gheisarieha's Ph.D. dissertation [36].

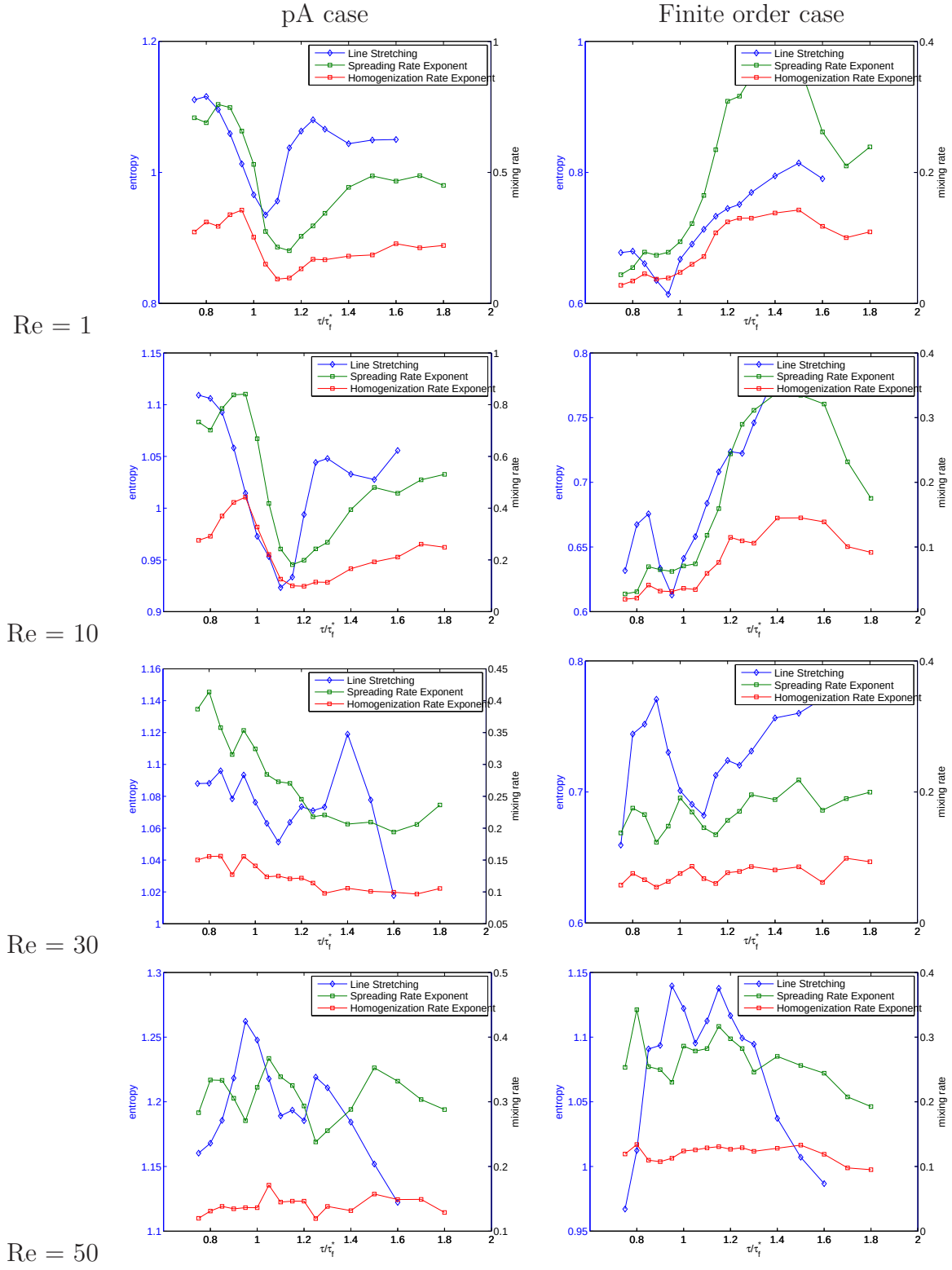

Figure 3.11: Comparison of h_{fluid} with mixing rate exponents. Here, the spreading rate is ϵ_1 and homogenization rate is ϵ_4 which are both defined in §2.5

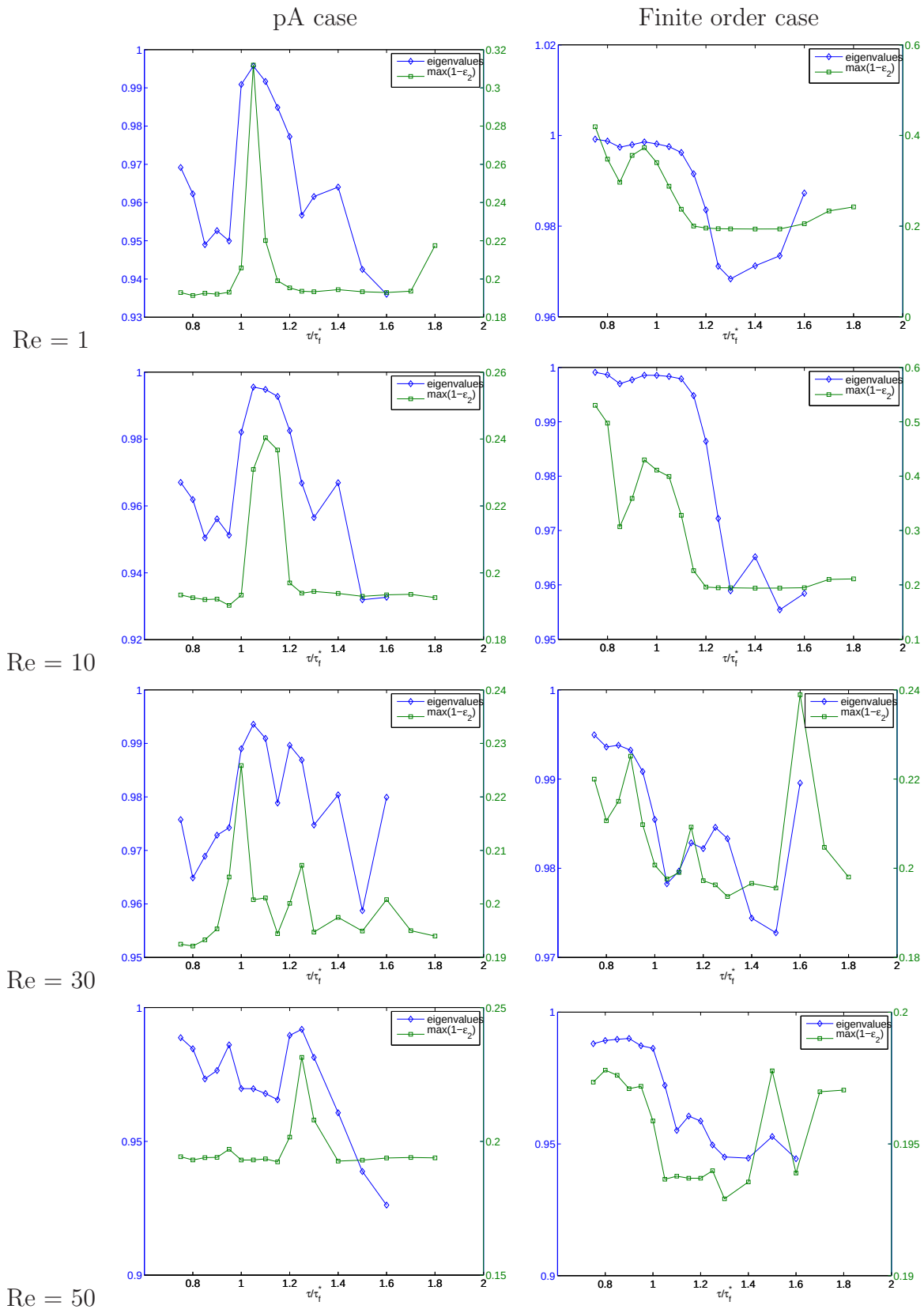

Figure 3.12: Comparison of $\lambda^{(2)}$ of the reversible matrix with the lowest value of $1-\epsilon_4$ after 40 τ_f^*

Chapter 4

Braiding using ACS and FTCS

4.1 Methodology for identifying ACS from AIS using thresholding

The following methodology is used to identify ACS in the flow domain using the eigenvectors of the reversible matrix $R_{n,\tau}$. Every eigenvector $v^{(p)}$ partitions the domain X into two almost invariant sets $A_1^{(p)}$ and $A_2^{(p)}$ based on the choice of c as in Eq. 2.14. The coherent structures identified by each such set are determined by keeping only those bins which correspond to an entry in $v^{(p)}$ that meets a threshold criterion as outlined below. First, vectors corresponding to each half are derived from the eigenvector using the relation

$$w_{1,i} = c - v_i, \{i : v_i \leq c\} \tag{4.1}$$

$$w_{2,i} = v_i - c, \{i : v_i \geq c\}. \tag{4.2}$$

The superscripts (p) have been dropped in the following discussion for convenience. The vectors w_1 and w_2 are then normalised by the maximum value in each vector, to obtain $\hat{w}_1$ and $\hat{w}_2$. A threshold c_2 is selected, so as to obtain the sets $\hat{A}_1$ and $\hat{A}_2$ by selecting bins that

are a subset of the bins from Eq. 2.14 in the following manner

$$\hat{A}_1 = \cup_{i \in I_1} B_i, \qquad \text{where} \quad I_1 = \{i : \hat{w}_{1,i} \geq c_2\}, \tag{4.3}$$

$$\hat{A}_2 = \cup_{i \in I_2} B_i, \qquad \text{where} \quad I_2 = \{i : \hat{w}_{2,i} \geq c_2\}. \tag{4.4}$$

A value of 0.5 was used for c_2 for all results reported in this paper. This value (found by trial and error) gave the best results for the detection of ACS for the flow maps considered in this study. Coherent structures are then identified in each of the sets $\hat{A}_1$ and $\hat{A}_2$ by grouping adjacent bins together. Thus a set of groups of bins (or coherent structures) is identified in every AIS $\hat{A}$ and this can be expressed as

$$\hat{A} = \cup_{i \in I} G_i, \qquad \text{where} \quad I = \{1 \cdots n_g\}, \tag{4.5}$$

where G_i is the ith group and n_g is the total number of groups that are contained in a particular AIS.

Next, the ACS are determined as subsets of the set of groups that form an AIS. The set of groups that make up an AIS is represented as a connected graph. Each group in the set is represented as a node in the graph. An edge exists between nodes i and j iff

$$\Phi_\tau(G_i) \cap G_j \neq \emptyset. \tag{4.6}$$

A depth traversal algorithm is used to identify all cycles in this graph. From this set of cycles (if it is a non-empty set), all cycles that satisfy the following condition for every node in them are selected :

$$(\Phi_\tau(G_{i-1}) \cap G_i) \cap (\Phi_{-\tau}(G_{i+1}) \cap G_i) \neq \emptyset, \tag{4.7}$$

where $i-1$ is the node preceding node i and $i+1$ is the node succeeding node i in the cycle.

From the cycles that match this criteria, the cycle with the largest number of nodes is selected as the representative ACS for the corresponding AIS.

A representative point is selected from each of the nodes (groups) of this ACS. To calculate the entropy associated with the ACS, the positions of the representative points are integrated in time for one period (τ) using the velocity field to calculate their trajectories. These trajectories approximate the trajectories of the coherent structures that form the ACS. The manner of identifying the representative points outlined above guarantees that the trajectories stay within their respective coherent structures at least for one period. Thus the entropy calculated from a periodic continuation of these trajectories gives the entropy of the braiding action of the ACS. It is important to note however that these coherent structures used to calculate the entropy are almost-cyclic, and not necessarily exactly-cyclic (and may not therefore contain points on elliptic orbits). The braid calculated in the methodology described above is exact if there exist points on elliptic orbits within each of the elements of the ACS, and is an approximation of the braiding action of the ACS otherwise.

4.2 Methodology for identifying Finite Time Coherent Structures

To identify finite time coherent structures in the flow field, the right singular vectors $v_s^{(p)}$ of the discretised Perron-Frobenius operator are first calculated as described in §2.1.2. The flow map Φ_T required for calculating the discretised Perron-Frobenius operator is calculated by advecting evenly distributed points in the domain for a duration of $t = T$, and following the steps in §2.1.2. The value of T selected should be the longest time for which coherent structures can be detected using this method. A long T enables one to get structures in the flow that remain coherent for long times, which can be used to get more meaningful trajectories for the estimation of topological entropy of the flow field. For the FTCS results

in this thesis, the value of T selected varied between 6 flow periods (for the shortest switching periods) to 3 flow periods (for the longest flow period). For the purposes of calculation of the braid using the representative FTCS points, the braid trajectories were calculated by advecting the points in time for 8 flow periods. Note that in some cases, this time window is not enough to approach the asymptotic value of the topological entropy calculated using the Dynnikov method, which leads h_{FTCS} to predict a value higher than h_f.

Each singular vector divides the domain into two halves. The vectors $\hat{w}_1$ and $\hat{w}_2$ corresponding to each half are then calculated exactly as done for the calculation of ACS. A suitable threshold is selected to obtain groups of coherent structures, and a union of the groups obtained from each half is selected. The local maximum of $\hat{w}_1$ or $\hat{w}_2$, as the case might be within each group is selected as the representative point for that group.

The trajectories of these points are then used to estimate the topological entropy of the flow field. Since the calculation for FTCS does not assume any periodicity of the flow, the braids generated by these trajectories can not be assumed to be periodic in time.

4.3 Braiding results for flow fields based on the 3-rod pA protocol

4.3.1 Re = 1

In the mixing study done using the reference case parameters in Ref. [1] it was found that the results for Re $\leq$ 1 were essentially identical suggesting that the Stokes' assumptions are valid for Re $\leq$ 1. Figures 4.1(a,b) show the comparison between the entropy calculated using the line stretching method (h_f) and the methodology described in the previous section using the ACS (h_{ACS}) and FTCS (h_{FTCS}) for Re = 1. The switching periods considered vary between $0.75\tau_f^*$ and $1.8\tau_f^*$.

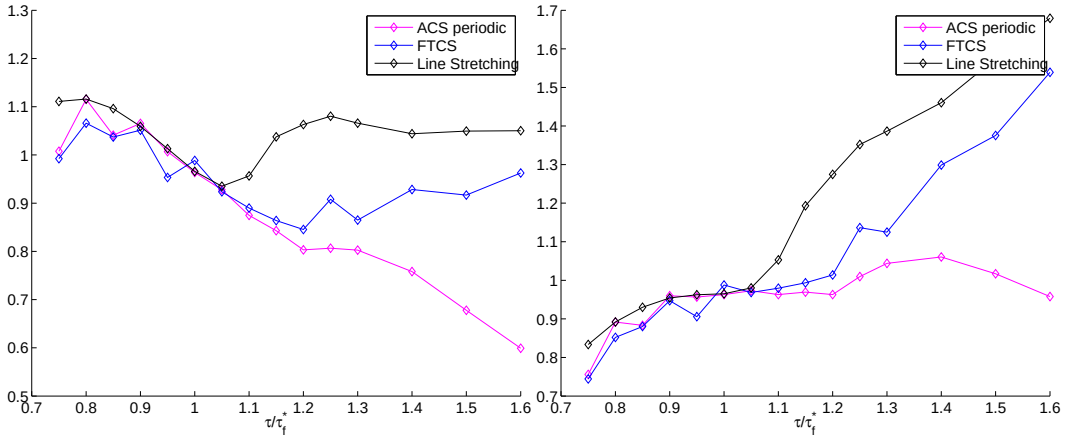

(a) (b)

Figure 4.1: Topological entropy obtained for Re = 1 for various switching periods. The black line corresponds to topological entropy calculated using the line stretching method (h_f), the blue line shows the maximum entropy calculated among various FTCS, and the magenta line shows the maximum entropy calculated among various ACS (h_{ACS}) for each switching period. The graph on left is normalised using τ_f^* and the graph on the right is normalised using τ.

As is seen from the figures, the entropy calculated using the ACS method is always lower than that of the entropy calculated by the line stretching method. This should be the case, because the line stretching method in effect takes into account all the trajectories in the flow field and effectively estimates the entropy of the entire flow field, whereas, the ACS method looks at the trajectories of just one set of ACS. This methodology does not capture complexity in the flow due to the interaction of different ACS across different AIS or even within the same AIS.

The value of $h_{f,\tau}$ increases monotonically with increase in τ. This is expected, as $h_{f,\tau}$ is a measure of the stretching of material lines per period, and τ is the time for one period in each case. As the length of the period increases, the fluid is under the action of a pA braid for more time per period, which should lead to more stretching per period. There is no such monotonic behaviour seen in h_{f,τ_f^*}, which is a measure of stretching of material lines in the flow per reference flow period (τ_f^*). This value stays relatively constant over the range

of switching periods when compared to $h_{f,\tau}$. Particularly, for Re = 1, there is a monotonic decrease in $h_{f,\tau}$ in the neighbourhood of $\tau = \tau_f^*$.

For Re = 1, the value of $h_{\mathrm{ACS},\tau_f^*}$ mostly decreases with increase in τ, whereas the value of $h_{\mathrm{ACS},\tau}$ remains relatively constant with τ. This would indicate that the dominant ACS braids are similar across varying τ and are closely related to the 3-rod braid. Thus, for $\tau \leq 1.05\tau_f^*$, the value of h_{ACS} closely matches that of h_f, and gives a better approximation as compared to h_{FTCS}. For greater values of τ however, since the highest entropy per cycle does not increase significantly, the value of h_{ACS} diverges from that of h_f, and h_{FTCS} provides a better approximation of h_f, with a similar rate of increase in entropy with increase in τ.

Figures 4.2(a), 4.3(a), 4.4(a) and 4.5(a), show the entropies calculated for individual ACS across different τ. The x axis for the figures is the ACS number, where, the two ACS corresponding to the eigenvector (of the reversible matrix) i are numbered $(i-1)*2-1$ and $(i-1)*2$. Recall that the first eigenvector is trivial as it corresponds to the entire domain. The left y axis is the topological entropy (normalised by τ), and the right y axis is the number of braids for each case. The entropy calculated using the ACS is compared with the entropy obtained using the line stretching method and the baseline entropy of the 3-ghost rod system. Note that not all AIS are represented for each case in these figures. The missing ACS points correspond to the cases where the methodology described in §4.1 was not able to determine at least 3 groups on a cycle.

Similarly, figures 4.2(b), 4.3(b), 4.4(b) and 4.5(b), show the entropies calculated for individual FTCS across different τ. The ith intercept on the x axis gives the number of trajectories identified in the $(i+1)$th singular vector, with i = 1 being the trivial singular vector corresponding to the entire domain. Note that since the generators of the ACS braid are periodic in time, we can use periodic extensions of the ACS braid for a finite time to get a very good approximation of the asymptotic topological entropy of the ACS braid using the Dynnikov method. However, the FTCS generators are not necessarily periodic in time. Therefore,

using the generators formed by the FTCS braids for a finite time may not give us a good approximation of the asymptotic value of h_{FTCS}. This could explain why calculated value of h_{FTCS} overstimates h_f in some cases.

The entropy calculated using the FTCS trajectories (h_{FTCS}) is compared with the entropy estimated using the ensemble averaging method (h_{ensemble}). This method calculates the ensemble average of the topological entropy of the braids of trajectories of multiple seedings of random points in the fluids as described in §2.2. In the figures, the y coordinate for the plots of h_{ensemble} is the average topological entropy for all the random seedings, and the error bar indicates $\pm$ one standard deviation.

Figure 4.2 shows the results for $\tau = 0.9\tau_f^*$. This case can be thought of as one in which the shorter switching period causes the elliptical points from the reference flow to stop short of exchanging positions with each other. A look at the contour plots of the eigenvectors of the reversible matrix reveals the absence of the 3 ghost-rod structure. The 2nd AIS gives us 2 ACS with 8 and 7 braids respectively, and the 3rd and 5th AIS give us ACS with 5 braids. The topological entropy of these braids is very close to that of the 3-rod braid. The singular vectors for this case produce FTCS in the form of elongated structures. For this case, it is observed that h_{FTCS} gives a better estimate of h_f than h_{ensemble}.

Figure 4.3 shows the results for $\tau = \tau_f^*$. From the conclusions drawn in Ref. [1], this case is expected to be very similar to the reference Stokes' flow case. Indeed, the 3-ghost rod structure is seen in all the ACS of the first 8 eigenvectors of the reversible matrix, all of them having $h_{\mathrm{ACS}} \approx 0.96$. Similar structures are seen in the FTCS plots as well.

Figure 4.4 shows the results for $\tau = 1.25\tau_f^*$. The plots of the eigenvectors of the reversible matrix seem to suggest that the 3-ghost rod structures in $\tau = \tau_f^*$ have fragmented into 3 groups of coherent structures. The ACS corresponding to the second eigenvector consist of 11 braids each, and have a topological entropy slightly higher than 0.96. The ACS corresponding to the 3rd eigenvector are formed of 3 braids each, and the topological entropy of these braids

is the same as that of the 3-rod pA braid. The topological entropy predicted by the FTCS closely matches h_{ACS}. The value obtained for h_f however is higher than that predicted by the ACS and FTCS. Further, h_{ensemble} gives a slightly better estimate of h_f than h_{FTCS}.

Figure 4.5 shows the results for $\tau = 1.4\tau_f^*$. The first eigenvector gives 2 ACS on 2 braids each, which produce trivial braids by themselves. The 3rd and 4th eigenvectors give ACS on 4 braids which give an h_{ACS} an order of magnitude lower than that of the 3-rod pA braid. The 4th and 5th eigenvectors give ACS on 6 braids that have an entropy very close to that of the 3-rod pA braid. For this case, the topological entropy predicted by the FTCS method gives a better approximation of h_f as compared to the ACS method, and the results of h_{FTCS} and h_{ensemble} are essentially identical for the number of trajectories greater than 10.

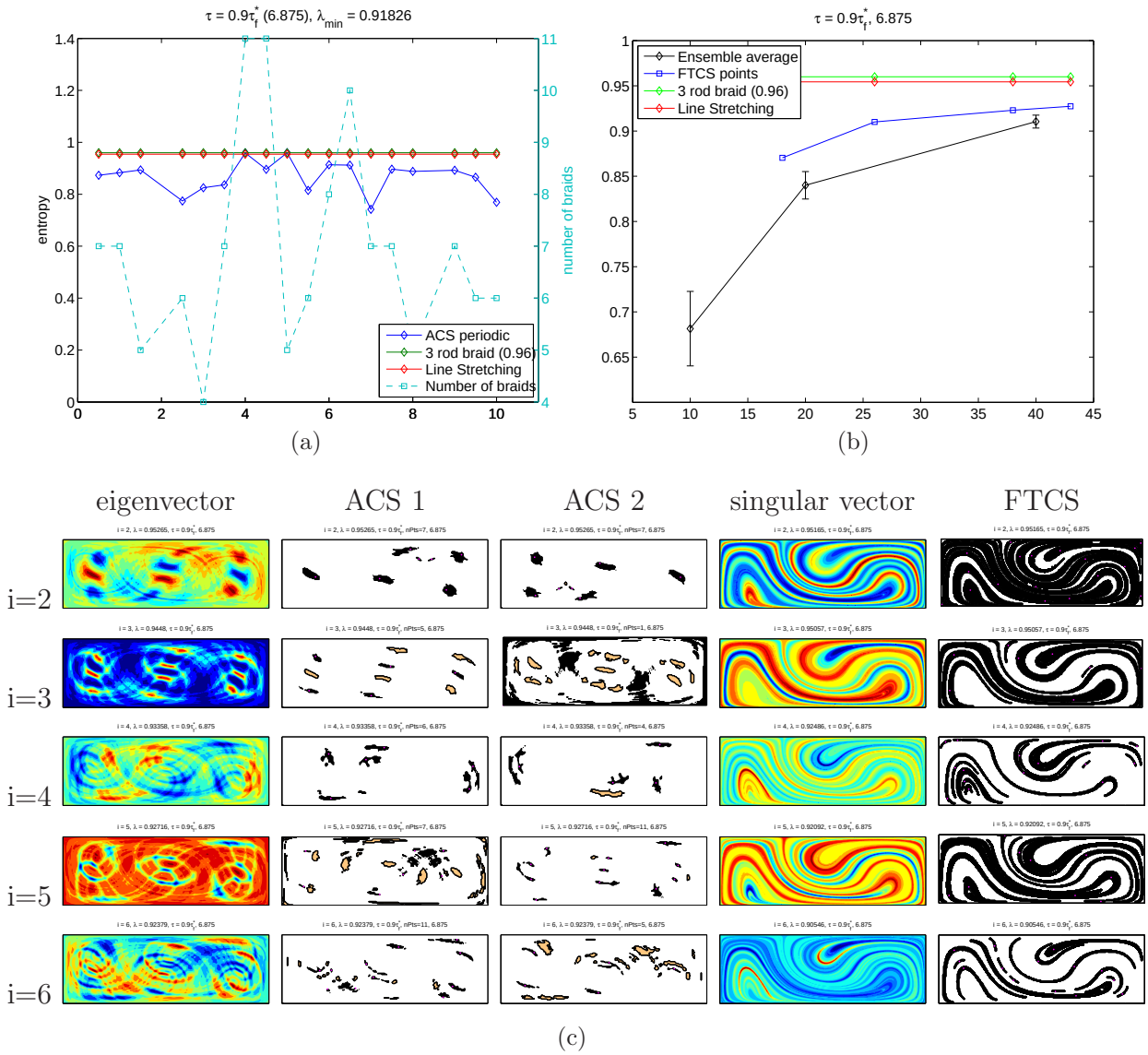

Figure 4.2: Figures (a) and (b) show the entropy for Re=1, $\tau = 0.9\tau_f^*$ calculated using the ACS and FTCS methods respectively, normalised using τ_f^*. The x axis in (a) is the ACS number, where, the two ACS corresponding to the eigenvector (of the reversible matrix) i are numbered $(i-1)\times 2-1$ and $(i-1)\times 2$. The left y axis is the topological entropy (normalised by τ), and the right y axis is the number of braids for each case. In (b), the ith x intercept corresponds to the $(i+1)$th singular vector. The 2nd and 3rd columns in (c) show the two ACS corresponding to the eigenvector in the first column. In these figures, the black structures form the ACS with the highest number of elements in the AIS, where as the light brown structures are coherent structures from the AIS that are not part of that ACS. The magenta points are the representative points for the coherent structures. The rightmost column in (c) shows the FTCS extracted from the singular vectors (4th column).

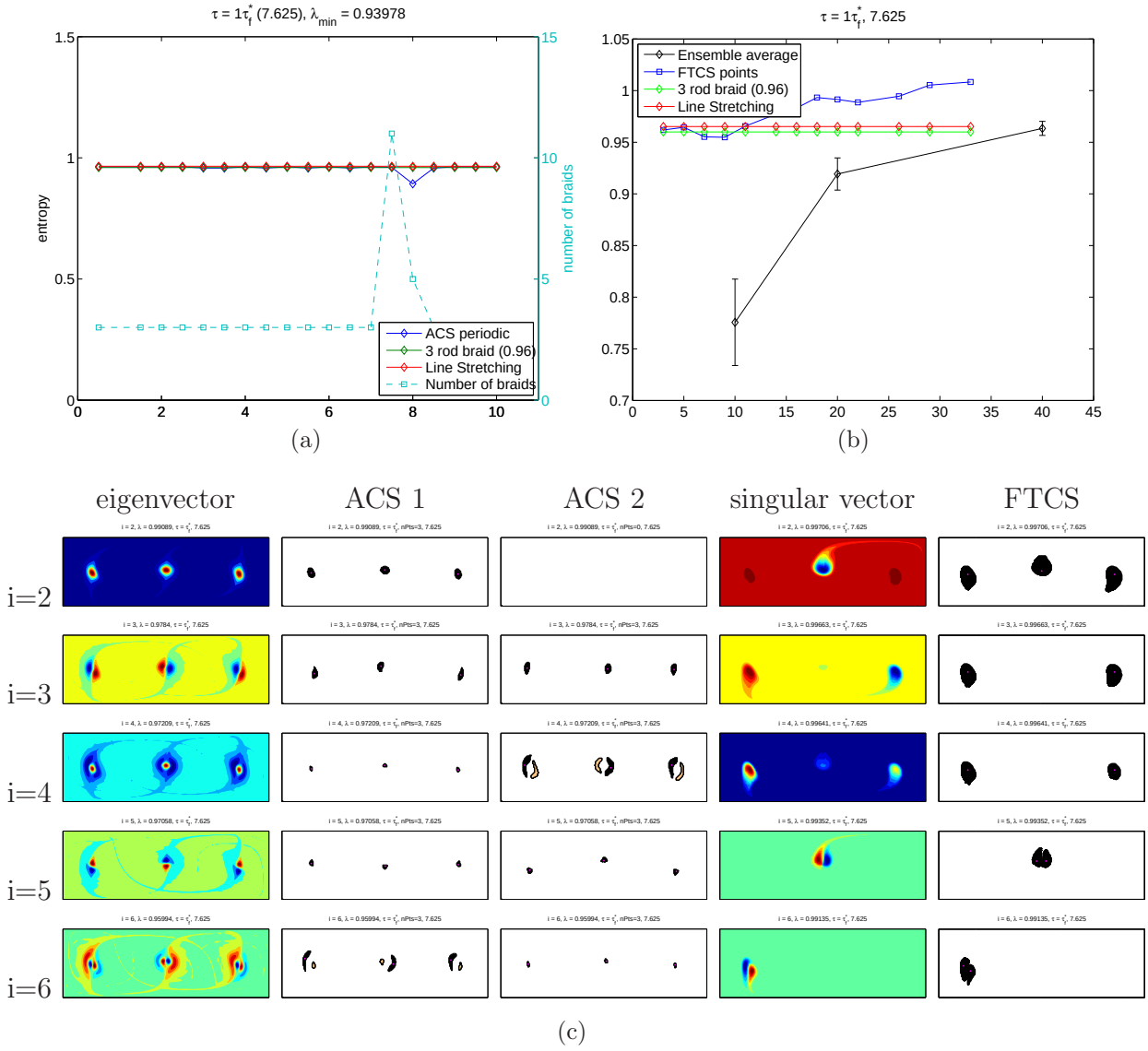

Figure 4.3: Figures (a) and (b) show the entropy for Re=1, $\tau = \tau_f^*$ calculated using the ACS and FTCS methods respectively, normalised using τ_f^*. The x axis in (a) is the ACS number, where, the two ACS corresponding to the eigenvector (of the reversible matrix) i are numbered $(i-1)\times 2-1$ and $(i-1)\times 2$. The left y axis is the topological entropy (normalised by τ), and the right y axis is the number of braids for each case. In (b), the ith x intercept corresponds to the $(i+1)$th singular vector. The 2nd and 3rd columns in (c) show the two ACS corresponding to the eigenvector in the first column. In these figures, the black structures form the ACS with the highest number of elements in the AIS, where as the light brown structures are coherent structures from the AIS that are not part of that ACS. The magenta points are the representative points for the coherent structures. The rightmost column in (c) shows the FTCS extracted from the singular vectors (4th column).

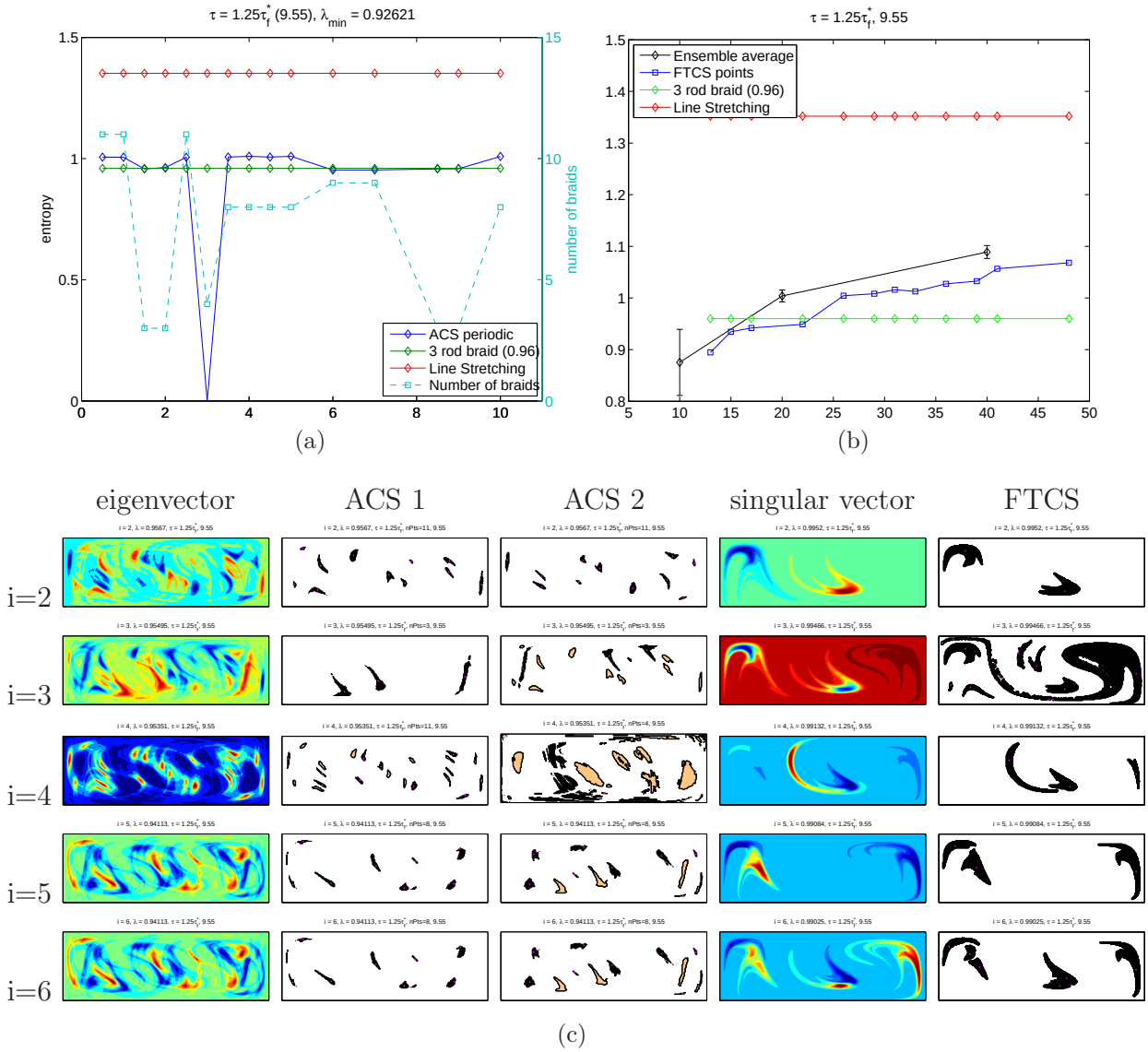

Figure 4.4: Figures (a) and (b) show the entropy for Re=1, $\tau = 1.25\tau_f^*$ calculated using the ACS and FTCS methods respectively, normalised using τ_f^*. The x axis in (a) is the ACS number, where, the two ACS corresponding to the eigenvector (of the reversible matrix) i are numbered $(i-1)\times 2-1$ and $(i-1)\times 2$. The left y axis is the topological entropy (normalised by τ), and the right y axis is the number of braids for each case. In (b), the ith x intercept corresponds to the $(i+1)$th singular vector. The 2nd and 3rd columns in (c) show the two ACS corresponding to the eigenvector in the first column. In these figures, the black structures form the ACS with the highest number of elements in the AIS, where as the light brown structures are coherent structures from the AIS that are not part of that ACS. The magenta points are the representative points for the coherent structures. The rightmost column in (c) shows the FTCS extracted from the singular vectors (4th column).

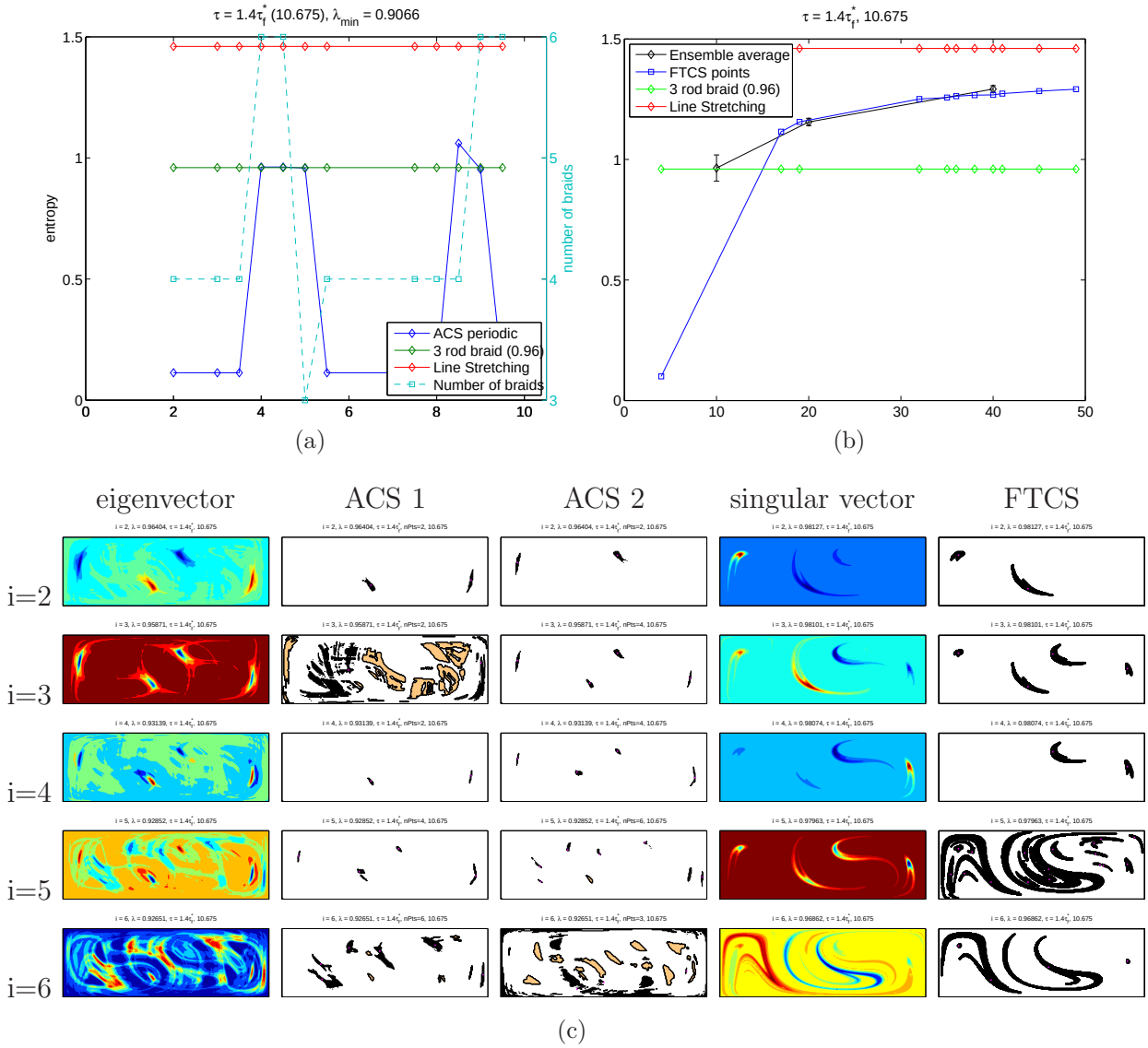

Figure 4.5: Figures (a) and (b) show the entropy for Re=1, $\tau = 1.4\tau_f^*$ calculated using the ACS and FTCS methods respectively, normalised using τ_f^*. The x axis in (a) is the ACS number, where, the two ACS corresponding to the eigenvector (of the reversible matrix) i are numbered $(i-1)\times 2-1$ and $(i-1)\times 2$. The left y axis is the topological entropy (normalised by τ), and the right y axis is the number of braids for each case. In (b), the ith x intercept corresponds to the $(i+1)$th singular vector. The 2nd and 3rd columns in (c) show the two ACS corresponding to the eigenvector in the first column. In these figures, the black structures form the ACS with the highest number of elements in the AIS, where as the light brown structures are coherent structures from the AIS that are not part of that ACS. The magenta points are the representative points for the coherent structures. The rightmost column in (c) shows the FTCS extracted from the singular vectors (4th column).

4.3.2 Re = 10

Figures 4.6(a,b) show the comparison between the entropy calculated using the line stretching method (h_f), ACS (h_{ACS}) and FTCS (h_{FTCS}) for Re = 10.The switching periods considered vary between $0.75\tau_f^*$ and $1.5\tau_f^*$. The entropy estimated using the ACS method is always lower than that of the entropy calculated by the line stretching method. Just as was the case for Re = 1, value of $h_{f,\tau}$ increases monotonically with increase in τ. Further, in the neighbourhood of $\tau = \tau_f^*$, there is a monotonic decrease in h_{f,τ_f^*}, which increases again and stabalises around $\tau = 1.2\tau_f^*$.

For Re = 10, just like in the case for Re = 1, the value of $h_{\mathrm{ACS},\tau_f^*}$ mostly decreases with increase in τ, whereas the value of $h_{\mathrm{ACS},\tau}$ remains relatively constant with τ. This would indicate that the dominant ACS braids are similar across varying τ and are closely related to the 3-rod braid. Thus, for $\tau \leq 1.05\tau_f^*$, the value of h_{ACS} closely matches that of h_f. The value of $h\mathrm{ACS}, \tau$ remains constant over $0.9\tau_f^* \leq \tau \leq 1.2\tau_f^*$. This is because the braid with the highest entropy for these cases is the 3-rod braid.

Figures 4.7(a), 4.8(a), 4.9(a) and 4.10(a), show the entropies calculated for individual ACS across different τ for Re = 10. Similarly, figures 4.7(b), 4.8(b), 4.9(b) and 4.10(b), show the entropies calculated for individual FTCS across different τ.

Figure 4.7 shows the contours of eigenvectors along with the corresponding ACS structures, as well as the singular vectors and corresponding FTCS for $\tau = 0.9\tau_f^*$. The 2nd eigenvector gives us 2 ACS with 8 and 7 braids respectively. There are 10 well defined structures in the 3rd eigenvector, all of which form part of one AIS. These AIS are split into two groups of 5 ACS structures, one of which has been considered for the calculation of h_{ACS}. The topological entropy of these braids is very close to that of the 3-rod braid. This would seem to suggest that the structures move together in 3 groups to give an overall motion similar to that generated by the 3-rod braid. Just as in the case of Re = 1, the FTCS is comprised of elongated structures that extend through most of the domain. The FTCS do not seem to

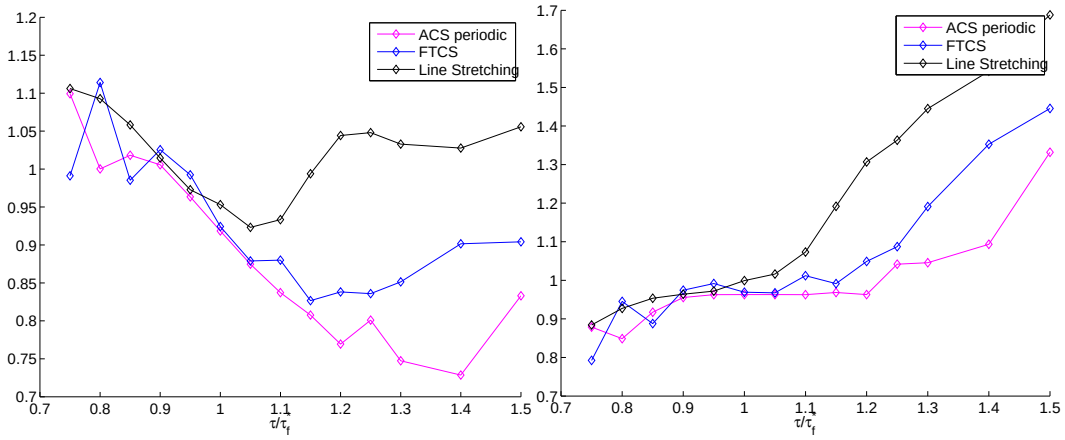

(a) (b)

Figure 4.6: A comparison of the topological entropy for Re = 10 for various switching periods. The black line corresponds to topological entropy calculated using the line stretching method (h_f), the blue line shows the maximum entropy calculated among various FTCS, and the magenta line shows the maximum entropy calculated among various ACS (h_{ACS}) for each switching period. The graph on left is normalised using τ_f^* and the graph on the right is normalised using τ.

bear resemblance to the AIS structures. Just like in the case for Re = 1, the singular vectors give us long and elongated FTCS structures. In this case however, h_{ensemble} gives a slightly better approximation of h_f than h_{FTCS}.

Figure 4.8 shows the results for $\tau = \tau_f^*$. The ACS as well as FTCS structures clearly show the presence of coherent structures on the pA 3-rod braid. This proves that the 3-rod mixing protocol can be extended up to Re = 10 with the reference case parameters to get similar results. This 3-rod structure is the dominant ACS for Re = 10 up to $\tau = 1.25\tau_f^*$, due to which all these cases have the same h_{ACS}. However, due to the interaction between the ACS corresponding to the lower eigenvectors, h_f for these cases actually increases with τ, which is not reflected by the values of h_{ACS}.

Figure 4.9 shows the results for $\tau = 1.3\tau_f^*$. For this case, each AIS from the two most dominant eigenvectors gives us ACS with 6 braid trajectories. The braid formed by these is identical and they have an entropy that is higher than that of the 3-rod braid. The FTCS

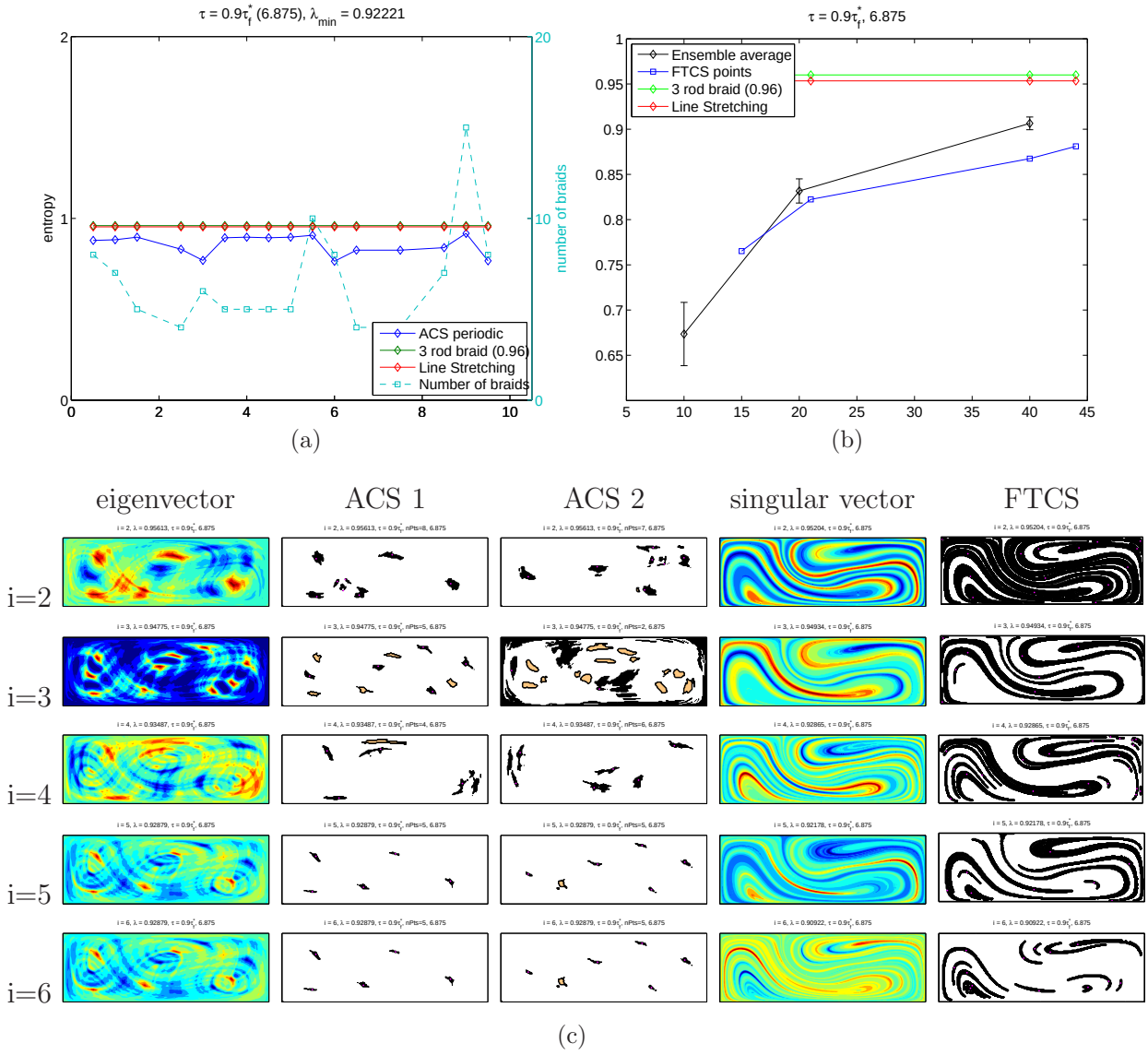

Figure 4.7: Figures (a) and (b) show the entropy for Re=10, $\tau = 0.9\tau_f^*$ calculated using the ACS and FTCS methods respectively, normalised using τ_f^*. The x axis in (a) is the ACS number, where, the two ACS corresponding to the eigenvector (of the reversible matrix) i are numbered $(i-1)\times 2-1$ and $(i-1)\times 2$. The left y axis is the topological entropy (normalised by τ), and the right y axis is the number of braids for each case. In (b), the ith x intercept corresponds to the $(i+1)$th singular vector. The 2nd and 3rd columns in (c) show the two ACS corresponding to the eigenvector in the first column. In these figures, the black structures form the ACS with the highest number of elements in the AIS, where as the light brown structures are coherent structures from the AIS that are not part of that ACS. The magenta points are the representative points for the coherent structures. The rightmost column in (c) shows the FTCS extracted from the singular vectors (4th column).

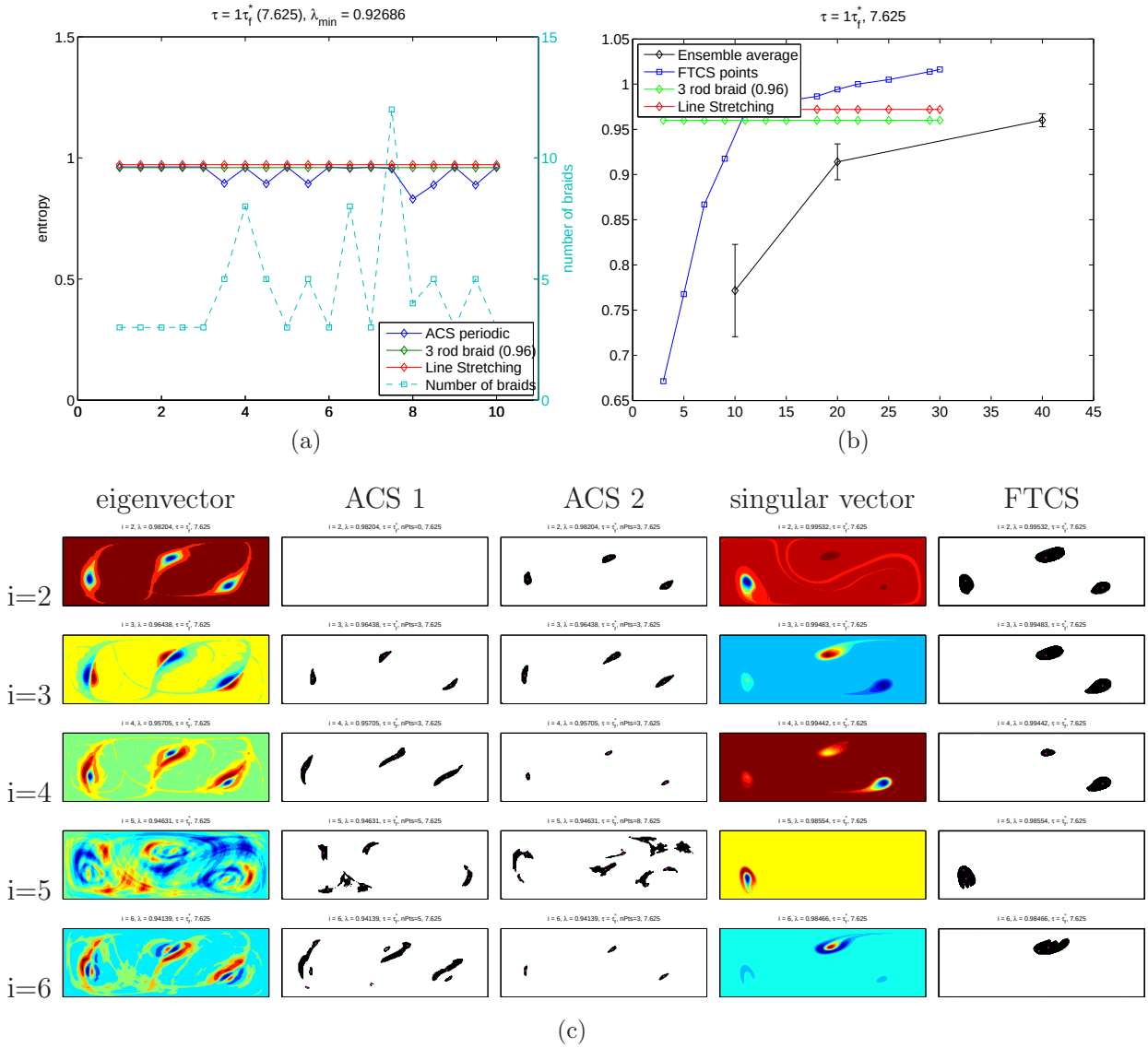

Figure 4.8: Figures (a) and (b) show the entropy for Re=10, $\tau = \tau_f^*$ calculated using the ACS and FTCS methods respectively, normalised using τ_f^*. The x axis in (a) is the ACS number, where, the two ACS corresponding to the eigenvector (of the reversible matrix) i are numbered $(i-1)\times 2-1$ and $(i-1)\times 2$. The left y axis is the topological entropy (normalised by τ), and the right y axis is the number of braids for each case. In (b), the ith x intercept corresponds to the $(i+1)$th singular vector. The 2nd and 3rd columns in (c) show the two ACS corresponding to the eigenvector in the first column. In these figures, the black structures form the ACS with the highest number of elements in the AIS, where as the light brown structures are coherent structures from the AIS that are not part of that ACS. The magenta points are the representative points for the coherent structures. The rightmost column in (c) shows the FTCS extracted from the singular vectors (4th column).

singular vectors give us structures that resemble the 3-rod braid system.

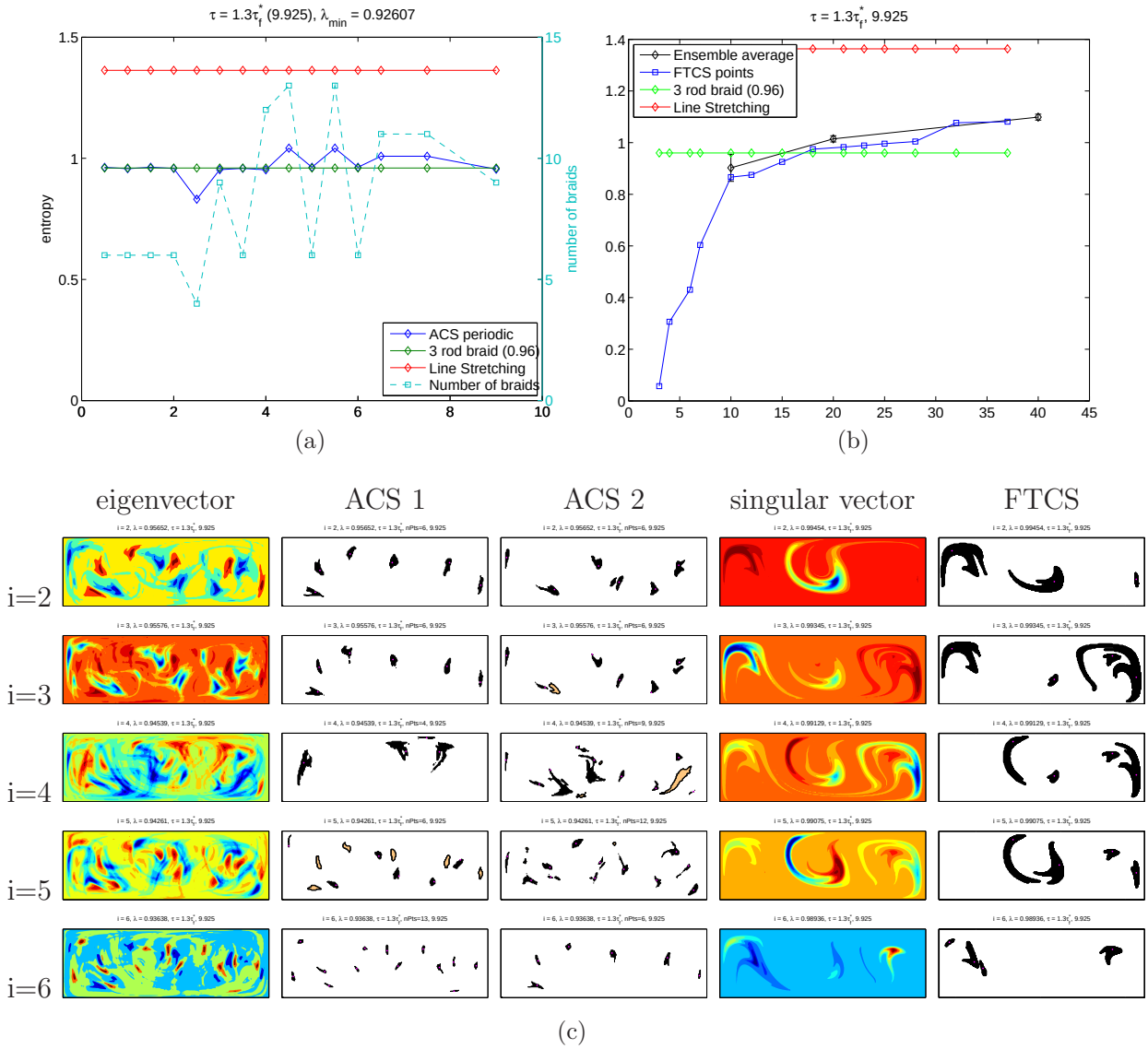

Figure 4.9: Figures (a) and (b) show the entropy for Re=10, $\tau = 1.3\tau_f^*$ calculated using the ACS and FTCS methods respectively, normalised using τ_f^*. The x axis in (a) is the ACS number, where, the two ACS corresponding to the eigenvector (of the reversible matrix) i are numbered $(i-1)\times 2-1$ and $(i-1)\times 2$. The left y axis is the topological entropy (normalised by τ), and the right y axis is the number of braids for each case. In (b), the ith x intercept corresponds to the $(i+1)$th singular vector. The 2nd and 3rd columns in (c) show the two ACS corresponding to the eigenvector in the first column. In these figures, the black structures form the ACS with the highest number of elements in the AIS, where as the light brown structures are coherent structures from the AIS that are not part of that ACS. The magenta points are the representative points for the coherent structures. The rightmost column in (c) shows the FTCS extracted from the singular vectors (4th column).

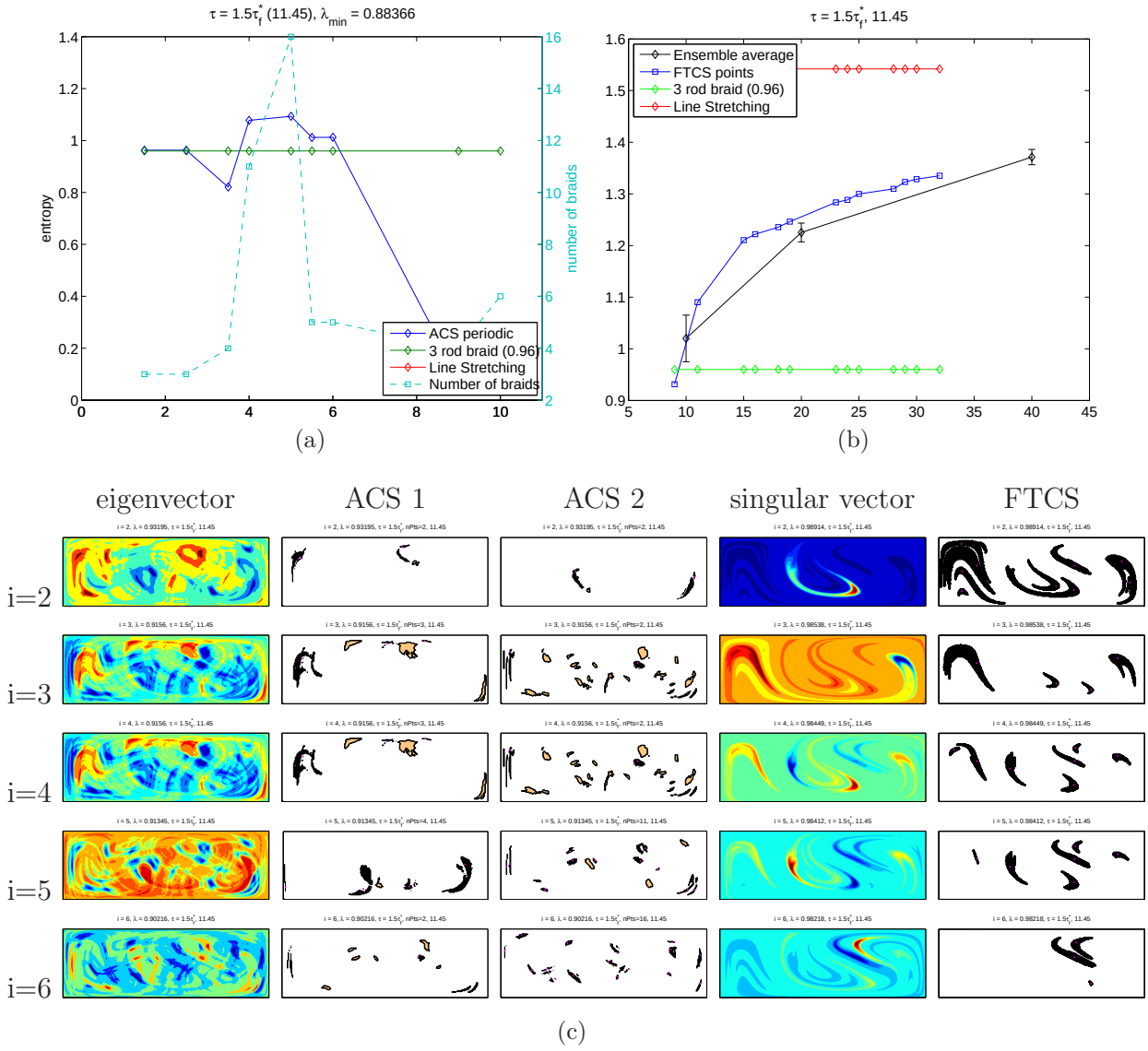

Figure 4.10: Figures (a) and (b) show the entropy for Re=10, $\tau = 1.5\tau_f^*$ calculated using the ACS and FTCS methods respectively, normalised using τ_f^*. The x axis in (a) is the ACS number, where, the two ACS corresponding to the eigenvector (of the reversible matrix) i are numbered $(i-1)\times 2-1$ and $(i-1)\times 2$. The left y axis is the topological entropy (normalised by τ), and the right y axis is the number of braids for each case. In (b), the ith x intercept corresponds to the $(i+1)$th singular vector. The 2nd and 3rd columns in (c) show the two ACS corresponding to the eigenvector in the first column. In these figures, the black structures form the ACS with the highest number of elements in the AIS, where as the light brown structures are coherent structures from the AIS that are not part of that ACS. The magenta points are the representative points for the coherent structures. The rightmost column in (c) shows the FTCS extracted from the singular vectors (4th column).

4.3.3 Re = 30

Figures 4.11(a,b) show the comparison between the entropy calculated using the line stretching method (h_f), ACS (h_{ACS}) and FTCS (h_{FTCS}) for Re = 30. The switching periods considered vary between $0.75\tau_f^*$ and $1.5\tau_f^*$. For Re = 30, the entropy estimated using the ACS and FTCS methods are always lower than that of the entropy calculated by the line stretching method, and give a value within 60% of the one given by line stretching. Just as was the case for Re = 1, the value of $h_{f,\tau}$ increases monotonically with increase in τ. The value of h_{f,τ_f^*} however remains relatively constant for all cases considered. Similarly, in the neighbourhood of $\tau = \tau_f^*$, there is a monotonic decrease in h_{f,τ_f^*}. Unlike Re = 10, however, this trend continues up to $\tau = 1.5\tau_f^*$.

For Re = 30, just like in the case for Re = 10, the value of h_{ACS,τ_f^*} mostly decreases with increasing τ. The value of $h_{\text{ACS},\tau}$, however, follows a monotonic increase, except for between $\tau = 1.3\tau_f^*$ and $\tau = 1.5\tau_f^*$, where we see a dip.

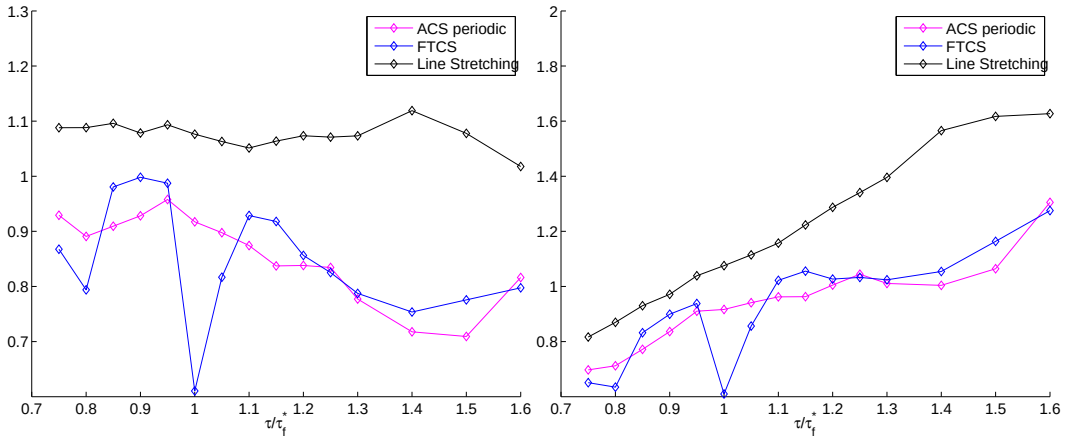

(a) (b)

Figure 4.11: Topological entropy obtained for Re = 30 for various switching periods. The black line corresponds to topological entropy calculated using the line stretching method (h_f), the blue line shows the maximum entropy calculated among various FTCS, and the magenta line shows the maximum entropy calculated among various ACS (h_{ACS}) for each switching period. The graph on left is normalised using τ_f^* and the graph on the right is normalised using τ.

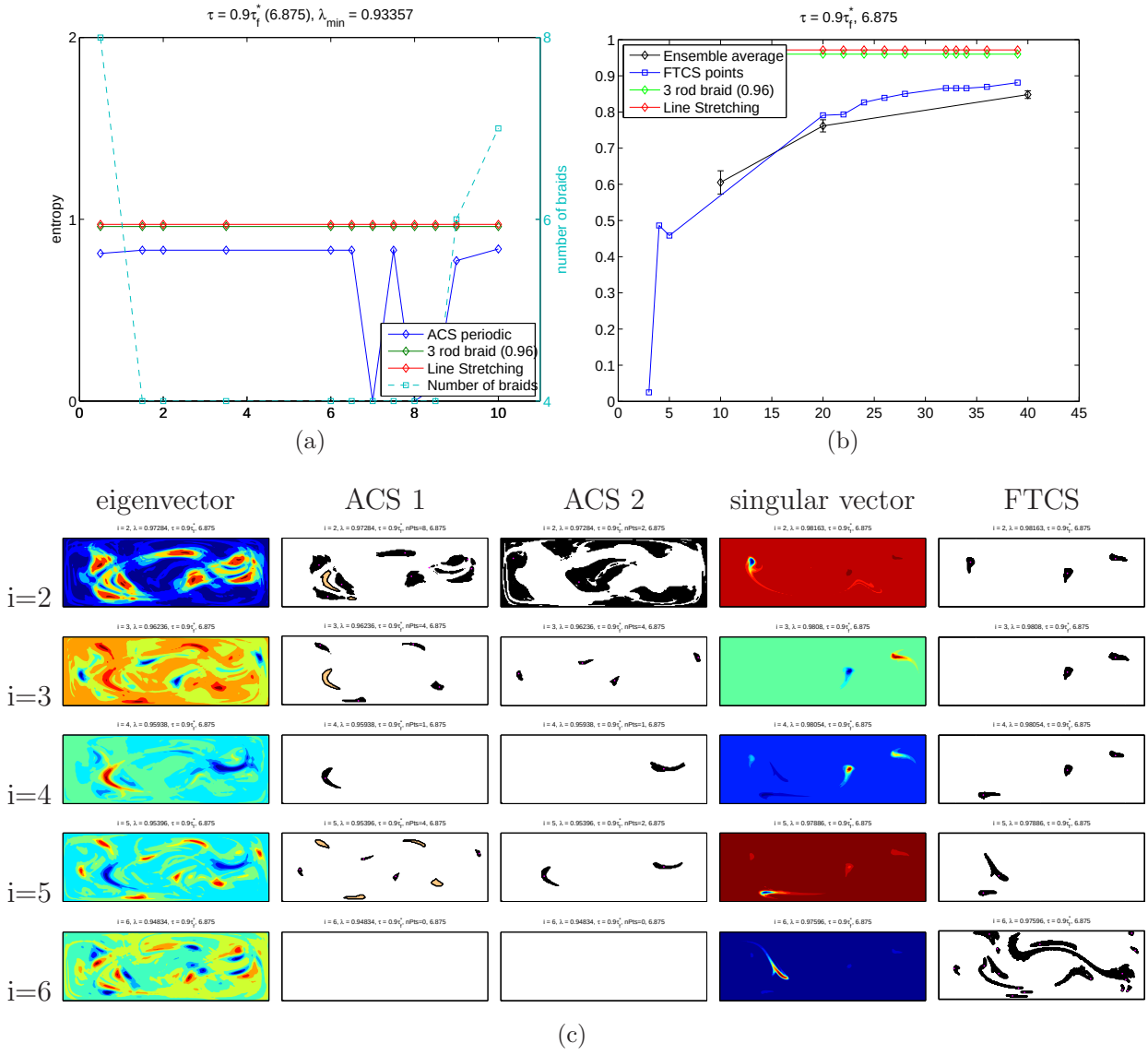

Figure 4.12: Figures (a) and (b) show the entropy for Re=30, $\tau = 0.9\tau_f^*$ calculated using the ACS and FTCS methods respectively, normalised using τ_f^*. The x axis in (a) is the ACS number, where, the two ACS corresponding to the eigenvector (of the reversible matrix) i are numbered $(i-1)\times 2-1$ and $(i-1)\times 2$. The left y axis is the topological entropy (normalised by τ), and the right y axis is the number of braids for each case. In (b), the ith x intercept corresponds to the $(i+1)$th singular vector. The 2nd and 3rd columns in (c) show the two ACS corresponding to the eigenvector in the first column. In these figures, the black structures form the ACS with the highest number of elements in the AIS, where as the light brown structures are coherent structures from the AIS that are not part of that ACS. The magenta points are the representative points for the coherent structures. The rightmost column in (c) shows the FTCS extracted from the singular vectors (4th column).

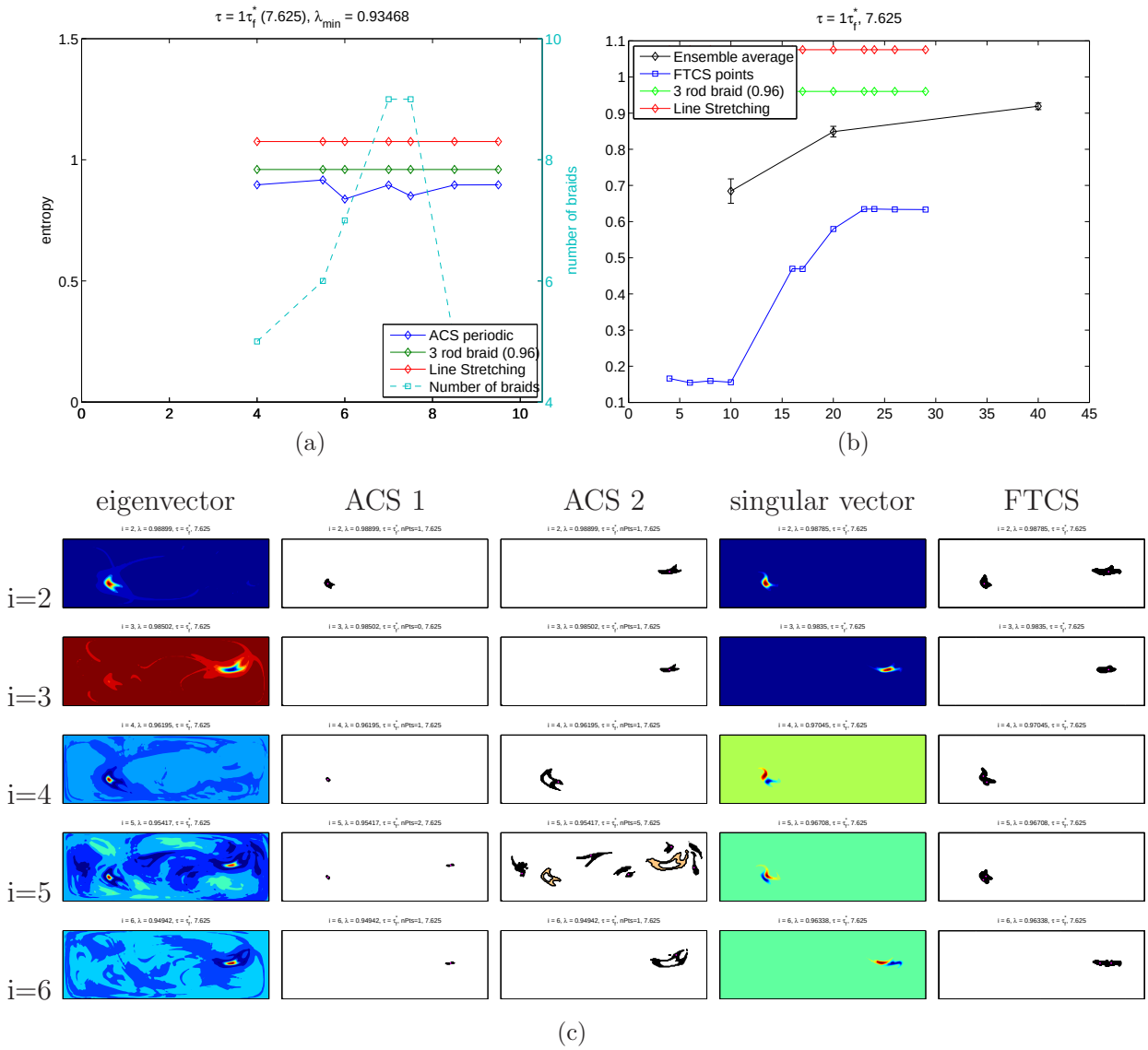

Figure 4.13: Figures (a) and (b) show the entropy for Re=30, $\tau = 1\tau_f^*$ calculated using the ACS and FTCS methods respectively, normalised using τ_f^*. The x axis in (a) is the ACS number, where, the two ACS corresponding to the eigenvector (of the reversible matrix) i are numbered $(i-1)\times 2-1$ and $(i-1)\times 2$. The left y axis is the topological entropy (normalised by τ), and the right y axis is the number of braids for each case. In (b), the ith x intercept corresponds to the $(i+1)$th singular vector. The 2nd and 3rd columns in (c) show the two ACS corresponding to the eigenvector in the first column. In these figures, the black structures form the ACS with the highest number of elements in the AIS, where as the light brown structures are coherent structures from the AIS that are not part of that ACS. The magenta points are the representative points for the coherent structures. The rightmost column in (c) shows the FTCS extracted from the singular vectors (4th column).

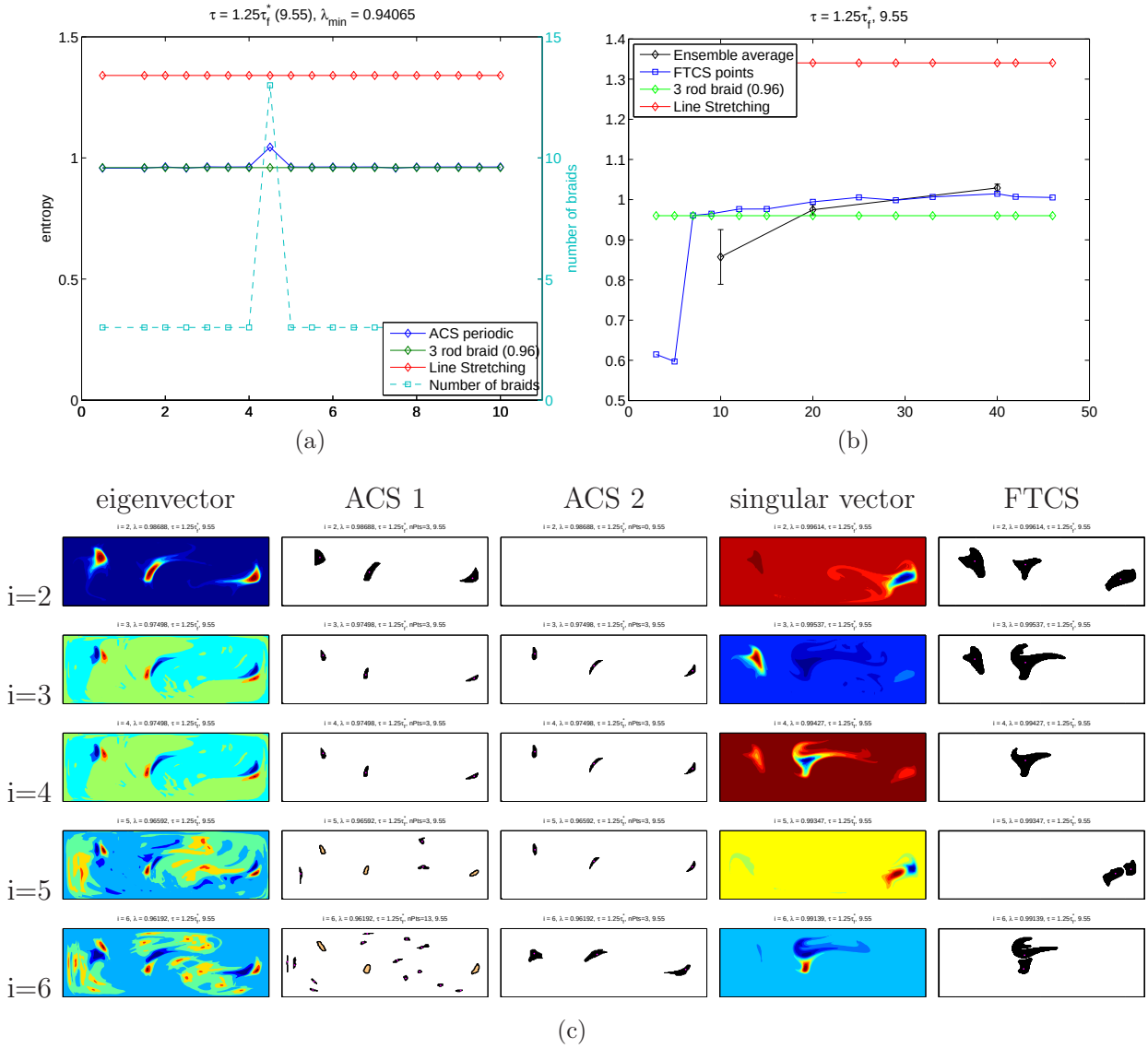

Figure 4.14: Figures (a) and (b) show the entropy for Re=30, $\tau = 1.25\tau_f^*$ calculated using the ACS and FTCS methods respectively, normalised using τ_f^*. The x axis in (a) is the ACS number, where, the two ACS corresponding to the eigenvector (of the reversible matrix) i are numbered $(i-1)\times 2-1$ and $(i-1)\times 2$. The left y axis is the topological entropy (normalised by τ), and the right y axis is the number of braids for each case. In (b), the ith x intercept corresponds to the $(i+1)$th singular vector. The 2nd and 3rd columns in (c) show the two ACS corresponding to the eigenvector in the first column. In these figures, the black structures form the ACS with the highest number of elements in the AIS, where as the light brown structures are coherent structures from the AIS that are not part of that ACS. The magenta points are the representative points for the coherent structures. The rightmost column in (c) shows the FTCS extracted from the singular vectors (4th column).

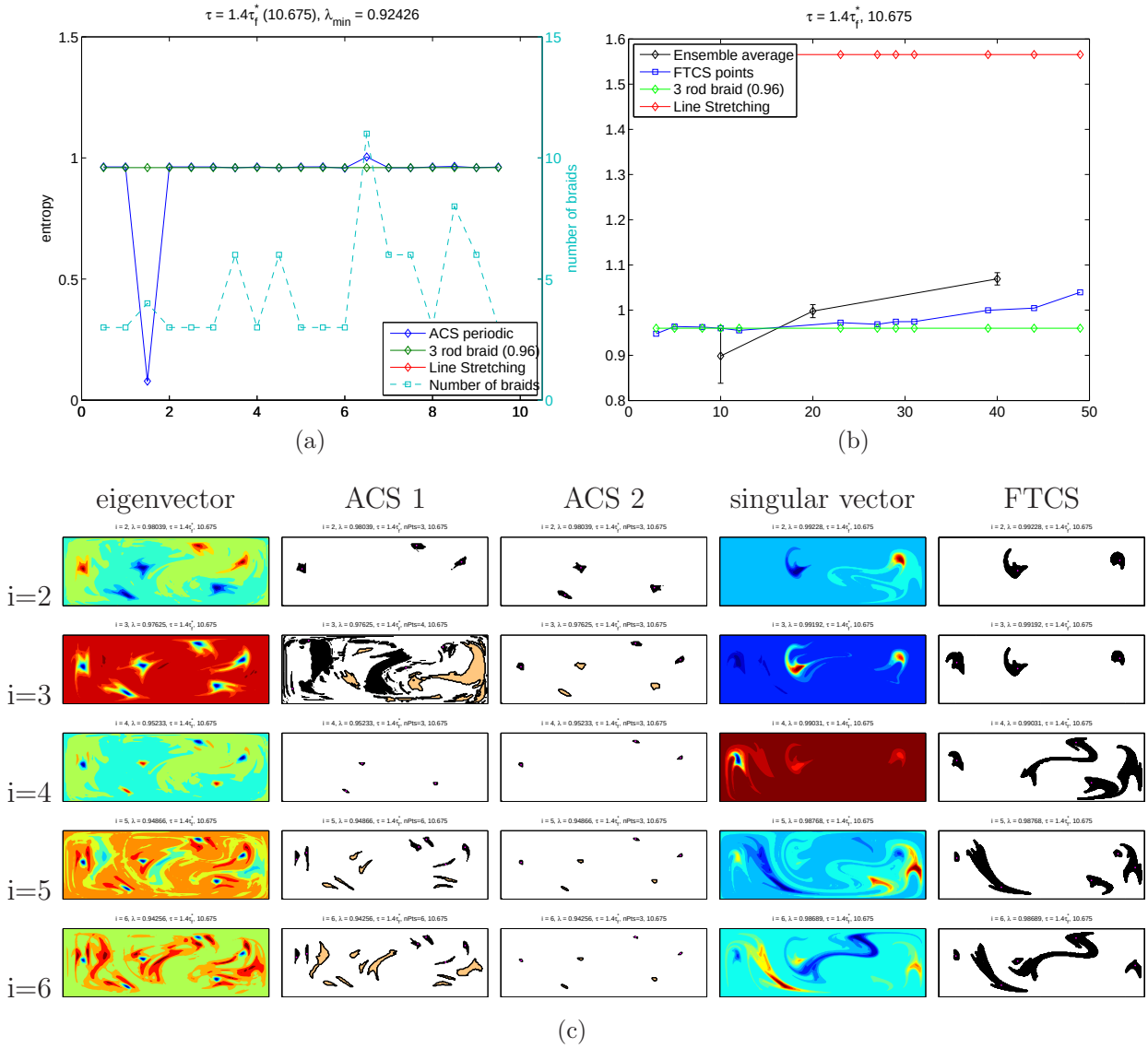

Figure 4.15: Figures (a) and (b) show the entropy for Re=30, $\tau = 1.4\tau_f^*$ calculated using the ACS and FTCS methods respectively, normalised using τ_f^*. The x axis in (a) is the ACS number, where, the two ACS corresponding to the eigenvector (of the reversible matrix) i are numbered $(i-1)\times 2-1$ and $(i-1)\times 2$. The left y axis is the topological entropy (normalised by τ), and the right y axis is the number of braids for each case. In (b), the ith x intercept corresponds to the $(i+1)$th singular vector. The 2nd and 3rd columns in (c) show the two ACS corresponding to the eigenvector in the first column. In these figures, the black structures form the ACS with the highest number of elements in the AIS, where as the light brown structures are coherent structures from the AIS that are not part of that ACS. The magenta points are the representative points for the coherent structures. The rightmost column in (c) shows the FTCS extracted from the singular vectors (4th column).

Figures 4.12(a), 4.13(a), 4.14(a) and 4.15(a), show the entropies calculated for individual ACS across different τ for Re = 30. Similarly, figures 4.12(b), 4.13(b), 4.14(b) and 4.15(b), show the entropies calculated for individual FTCS across different τ.

Figure 4.12 shows the results for $\tau = 0.9\tau_f^*$. The 3rd eigenvector produces 2 ACS with 4 braids each, and the 5th eigenvector produces an ACS with 4 braids as well. These braids are identical and, therefore, have the same braid entropy, which is very close to that of the 3-rod pA braid. The FTCS structures corresponding to the 2nd singular vector show structures similar to that in the 3-rod braid.

Figure 4.13 shows the results for $\tau = \tau_f^*$. Interestingly for this case, no topologically significant structures can be discerned until the fifth eigenvector or the eighth singular vector. Thus the most dominant AIS do not influnce the braiding in the fluid, at least just by themselves. Further, this leads to a low value of h_{FTCS} predicted by the singular vectors. The value of h_{ensemble} therefore is a much better approximation of the topological entropy of the flow as compared to h_{FTCS}. This is a good example of a flow with a pA braid in its dynamics that is not apparent in the most dominant AIS. The fifth eigenvector gives us an ACS with 5 braid trajectories, and the seventh gives 2 ACS with 6 and 7 braids respectively. The entropy of the braids produced by these ACS is comparable.

Figure 4.14 shows results for $\tau = 1.25\tau_f^*$. The ACS as well as FTCS strucutures clearly show the presence of coherent structures on the pA 3-rod braid. These structures persist all through the 11th eigenvector, making the 3-rod braid the dominant stirring mechanism for this case. This behaviour is seen for cases from $\tau = 1.2\tau_f^*$ to $\tau = 1.3\tau_f^*$.

Figure 4.15 shows the results for $\tau = 1.4\tau_f^*$. For this case, the two most dominant eigenvectors show 6 separate structures in the flow that are split across 2 ACS of 3 braids each.

4.3.4 Re = 50

Figures 4.16(a,b) show the comparison between the entropy calculated using the line stretching method (h_f), ACS (h_{ACS}) and FTCS (h_{FTCS}) for Re = 50. The switching periods considered vary between $0.75\tau_f^*$ and $1.5\tau_f^*$. For Re = 50, the entropy estimated using the ACS and FTCS methods are always lower than that of the entropy calculated by the line stretching method, and give a value within 50% of the one given by line stretching. Just as was the case for Re = 1, the value of $h_{f,\tau}$ increases monotonically with increase in τ. The value of h_{f,τ_f^*} remains relatively constant for all cases considered. Similarly, in the neighbourhood of $\tau = \tau_f^*$, there is a monotonic decrease in h_{f,τ_f^*}.

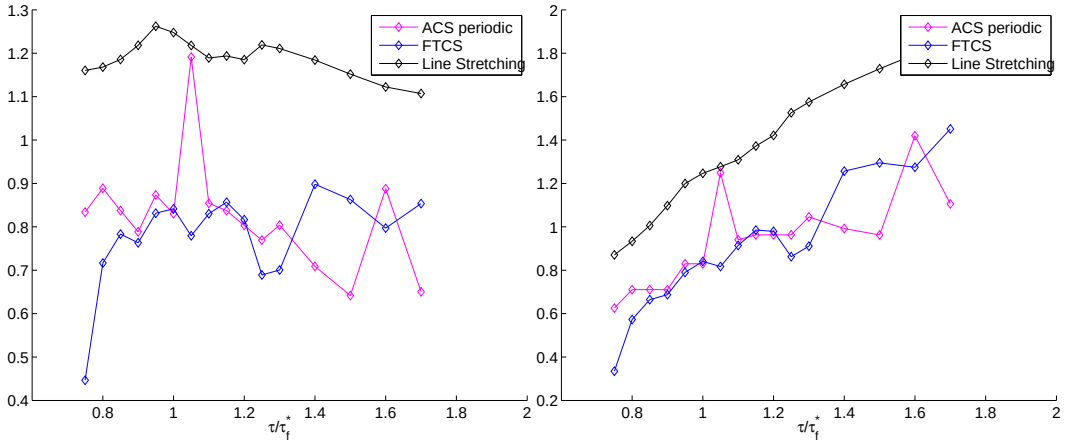

(a) (b)

Figure 4.16: Topological entropy obtained for Re = 50 for various switching periods. The black line corresponds to topological entropy calculated using the line stretching method (h_f), the blue line shows the maximum entropy calculated among various FTCS, and the magenta line shows the maximum entropy calculated among various ACS (h_{ACS}) for each switching period. The graph on left is normalised using τ_f^* and the graph on the right is normalised using τ.

Figures 4.17(a), 4.18(a) and 4.19(a), show the entropy calculated for individual ACS across different τ for Re = 50. Similarly, figures 4.17(b), 4.18(b) and 4.19(b), show the entropy calculated for individual FTCS across different τ.

Figure 4.17 shows the results for $\tau = 0.9\tau_f^*$. The first three eigenvectors have ACS that

produce finite order braids. The best approximation to h_f is produced by the ACS from the 7th and 8th eigenvectors that have braids on 7 strands.

Figure 4.18 shows the results for $\tau = \tau_f^*$. In this case, the 2nd and 3rd eigenvectors produce braids on 4 strands that have a low h_{ACS}. The 4th and 6th eigenvectors have ACS that produce braids on 4 strands with h_{ACS} that is of the same order of magnitude as h_f.

Figure 4.19 shows results for $\tau = 1.25\tau_f^*$. The ACS as well as FTCS strucutures clearly show the presence of coherent structures on the pA 3-rod braid.

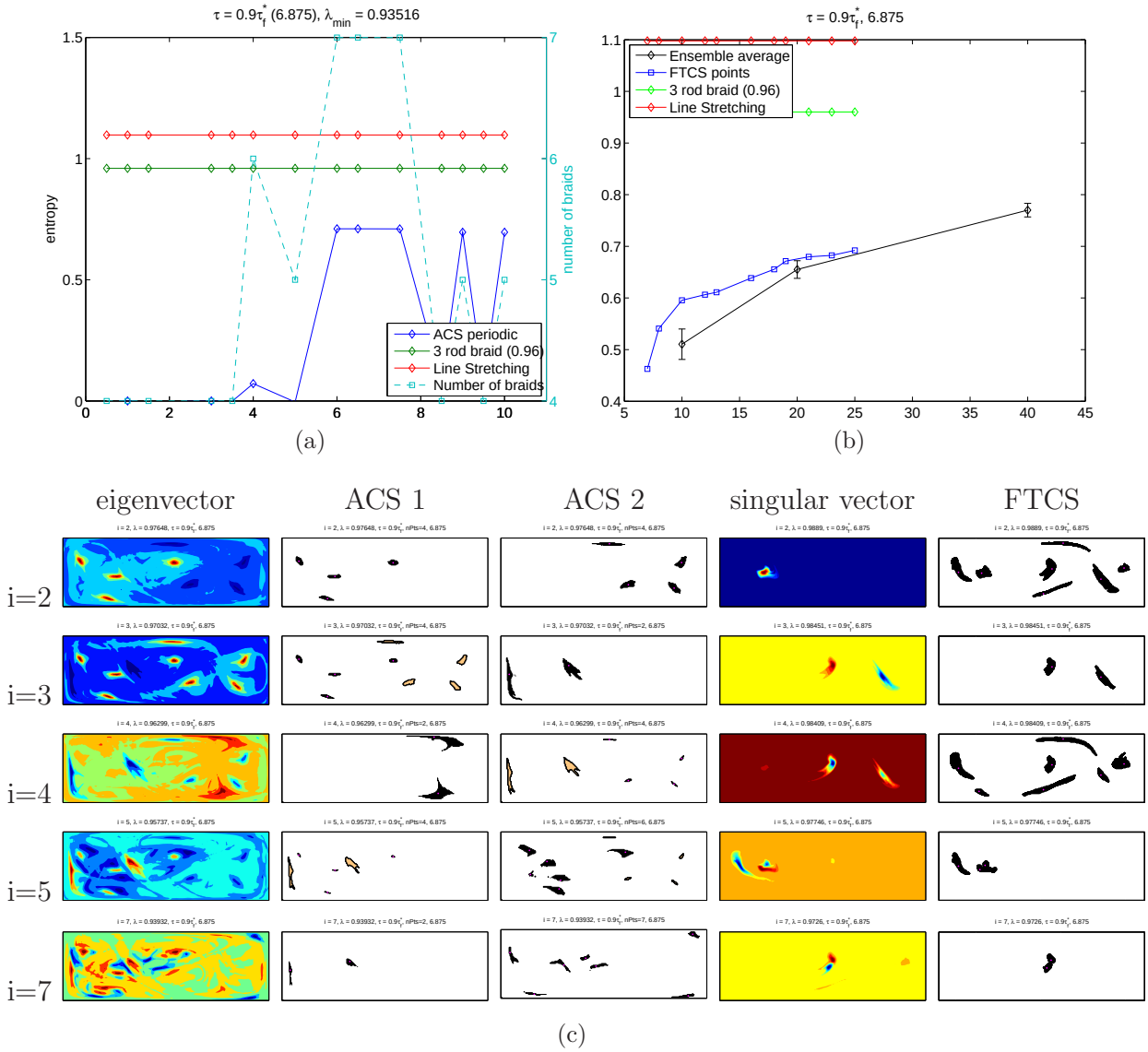

Figure 4.17: Figures (a) and (b) show the entropy for Re=50, $\tau = 0.9\tau_f^*$ calculated using the ACS and FTCS methods respectively, normalised using τ_f^*. The x axis in (a) is the ACS number, where, the two ACS corresponding to the eigenvector (of the reversible matrix) i are numbered $(i-1)\times 2-1$ and $(i-1)\times 2$. The left y axis is the topological entropy (normalised by τ), and the right y axis is the number of braids for each case. In (b), the ith x intercept corresponds to the $(i+1)$th singular vector. The 2nd and 3rd columns in (c) show the two ACS corresponding to the eigenvector in the first column. In these figures, the black structures form the ACS with the highest number of elements in the AIS, where as the light brown structures are coherent structures from the AIS that are not part of that ACS. The magenta points are the representative points for the coherent structures. The rightmost column in (c) shows the FTCS extracted from the singular vectors (4th column).

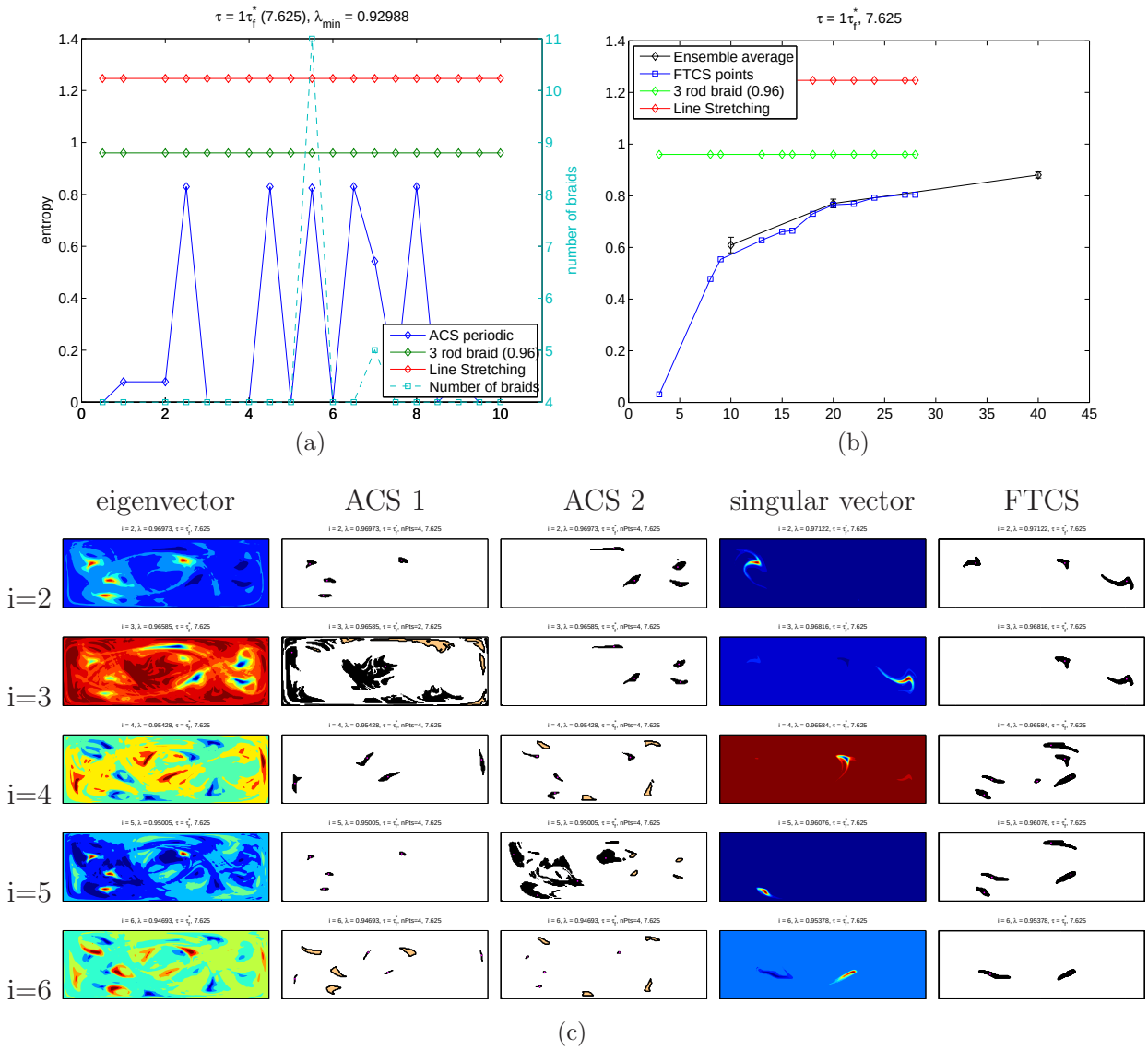

Figure 4.18: Figures (a) and (b) show the entropy for Re=50, $\tau = \tau_f^*$ calculated using the ACS and FTCS methods respectively, normalised using τ_f^*. The x axis in (a) is the ACS number, where, the two ACS corresponding to the eigenvector (of the reversible matrix) i are numbered $(i-1)\times 2-1$ and $(i-1)\times 2$. The left y axis is the topological entropy (normalised by τ), and the right y axis is the number of braids for each case. In (b), the ith x intercept corresponds to the $(i+1)$th singular vector. The 2nd and 3rd columns in (c) show the two ACS corresponding to the eigenvector in the first column. In these figures, the black structures form the ACS with the highest number of elements in the AIS, where as the light brown structures are coherent structures from the AIS that are not part of that ACS. The magenta points are the representative points for the coherent structures. The rightmost column in (c) shows the FTCS extracted from the singular vectors (4th column).

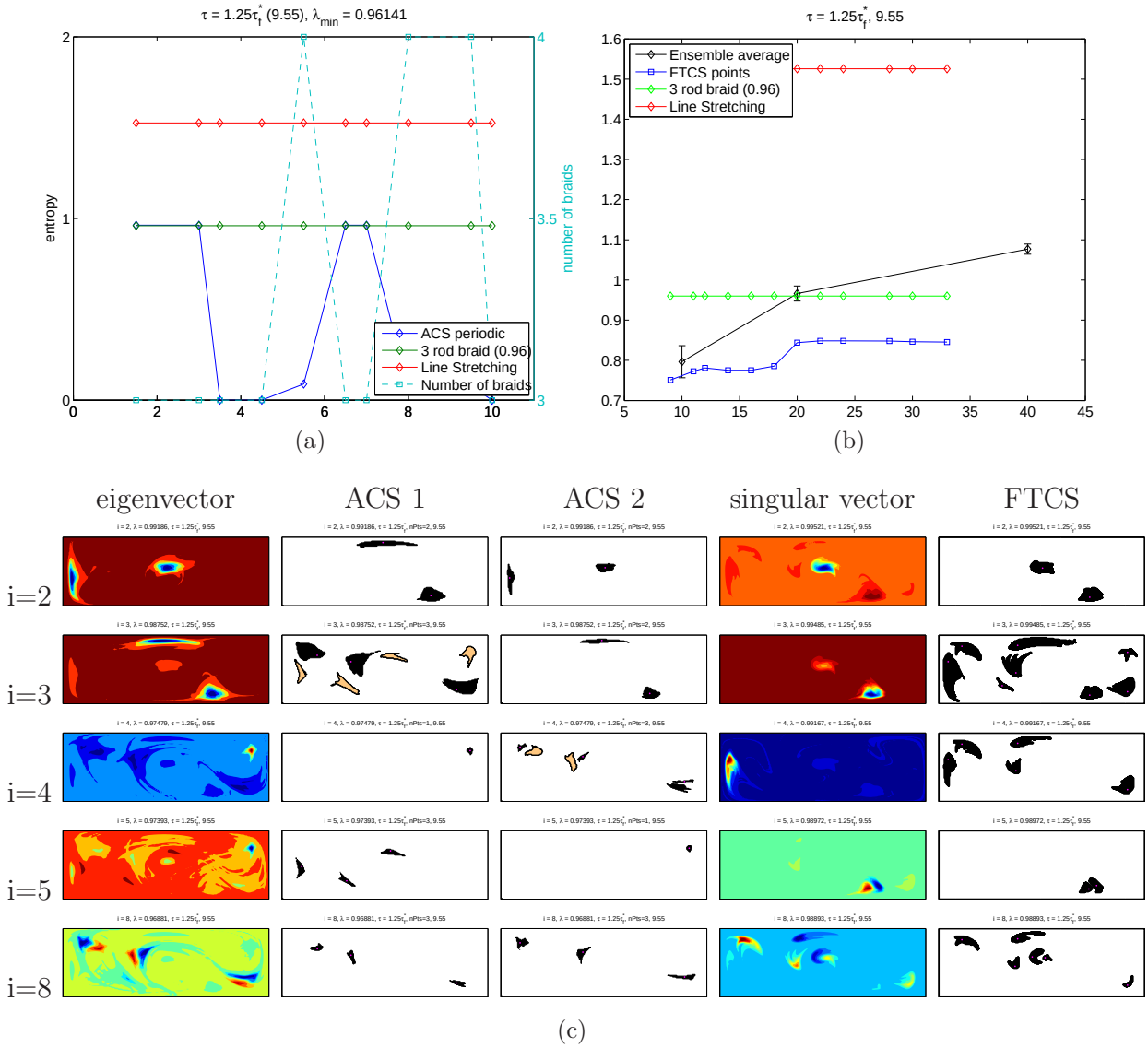

Figure 4.19: Figures (a) and (b) show the entropy for Re=50, $\tau = 1.25\tau_f^*$ calculated using the ACS and FTCS methods respectively, normalised using τ_f^*. The x axis in (a) is the ACS number, where, the two ACS corresponding to the eigenvector (of the reversible matrix) i are numbered $(i-1)\times 2-1$ and $(i-1)\times 2$. The left y axis is the topological entropy (normalised by τ), and the right y axis is the number of braids for each case. In (b), the ith x intercept corresponds to the $(i+1)$th singular vector. The 2nd and 3rd columns in (c) show the two ACS corresponding to the eigenvector in the first column. In these figures, the black structures form the ACS with the highest number of elements in the AIS, where as the light brown structures are coherent structures from the AIS that are not part of that ACS. The magenta points are the representative points for the coherent structures. The rightmost column in (c) shows the FTCS extracted from the singular vectors (4th column).

Chapter 5

Braiding results for flow fields based on the 3-rod finite order protocol

In the previous section, it was seen that the braids formed by dominant ACS in the flow fields considered gave a strict lower bound on the complexity of the flow, and provided an estimate of the topological entropy of the flow. However, all the cases were based on the Stokes' flow reference flow field with the 3-rod pA braid. It would be interesting to make this comparison between τ_{ACS} and τ_f for flow fields based on the Stokes' flow reference case with the 3-rod braid finite order braid.

Figure 5.1 shows the results obtained for the coherent structures in the flow field and their corresponding entropies, by using the same boundary conditions as the Stokes' flow case with the 3-rod finite order braid but varying the switching periods for Re = 1 and Re = 30 (top and bottom). For these cases as well, it is seen that the $h_{f,\tau}$ which is the topological entropy in the fluid normalised using the switching period (τ) increases with τ. Just as in the previous section, we see that h_{ACS} gives a strict lower bound for h_f. However, unlike in the previous section, we see that for a lot of cases, the ACS detected in the flow field do not give a very good estimate for h_f. This is seen in the case of h_{FTCS} as well.

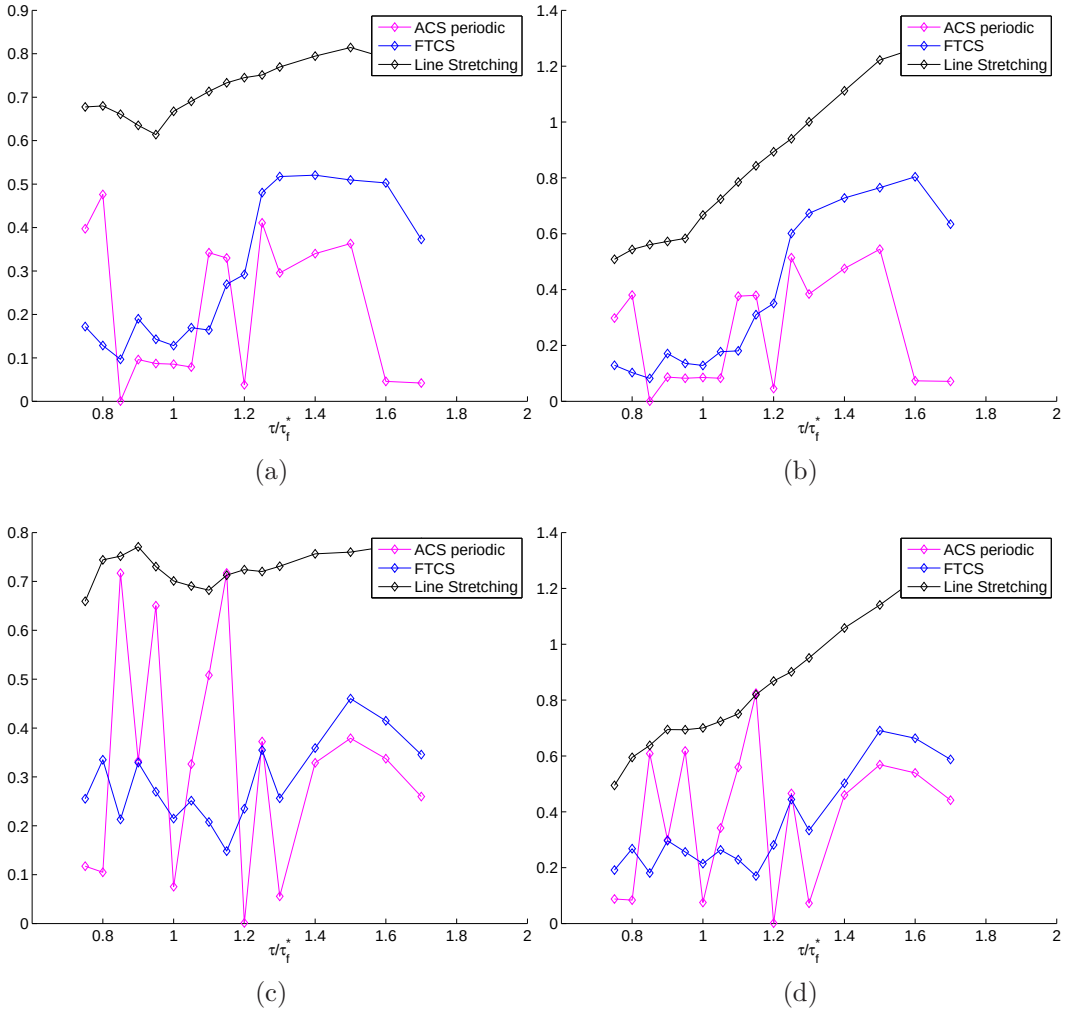

Figure 5.1: A comparison of the topological entropy for Re = 1 (top) and Re = 30 (bottom) for various switching periods. The black line corresponds to topological entropy calculated using the line stretching method (h_f), the blue line shows the maximum entropy calculated among various FTCS, and the magenta line shows the maximum entropy calculated among various ACS (h_{ACS}) for each switching period. The graphs on left are normalised using τ_f^* and the graph on the right are normalised using τ.

Figure 5.2 gives the results for $\tau = 0.8\tau_f^*$ for Re = 1, for the flow based on the Stokes' flow with the 3-rod finite order braid. As can be seen from the plot for h_{ACS}, the ACS identified in the first 4 eigenvectors are in sets of less than 3, and therefore do not have non-trivial braids. The braids formed by the ACS identified in the next 5 eigenvectors are all of finite order type, and have an entropy of 0. The only ACS that gives us a pA braid is the one

identified in the 10th eigenvector. This ACS forms a braid on 11 trajectories. The entropy predicted by the FTCS structures (h_{FTCS}) is a poor approximation of the entropy of the flow.

Figure 5.3 gives the results for $\tau = \tau_f^*$ for Re = 1, for the flow based on the Stokes' flow with the 3-rod finite order braid. As can be seen from the plot for h_{ACS}, the ACS identified in the first 3 eigenvectors of the reversible matrix are all of finite order type, and have an entropy of 0. The ACS from subsequent eigenvectors are of pA type. However, the topological entropy of the braids formed by the ACS give a poor estimate of the actual topological entropy of the flow. Further, the FTCS structures of the first 8 singular vectors are closely related to the AIS seen in the most dominant eigenvector of the reversible matrix. The entropy predicted by the FTCS structures (h_{FTCS}) also gives a poor approximation of the entropy of the flow.

Similary, figures 5.4 and 5.5 present two cases where the ACS provide good and poor approximations of h_f respectively for Re = 30. Fig. 5.4 is for $\tau = 0.85\tau_f^*$ where the ACS from the 9th eigenvector of the reversible matrix produces a pA braid on 6 strands that gives a very close approximation of h_f. On the other hand, as seen in Fig. 5.5 for $\tau = \tau_f^*$, all the first 25 eigenvectors have ACS either on finite order braids, or on pA braids that give an entropy which is an order of magnitude lower than h_f. In both these cases, h_{FTCS} does not give a good approximation of h_f.

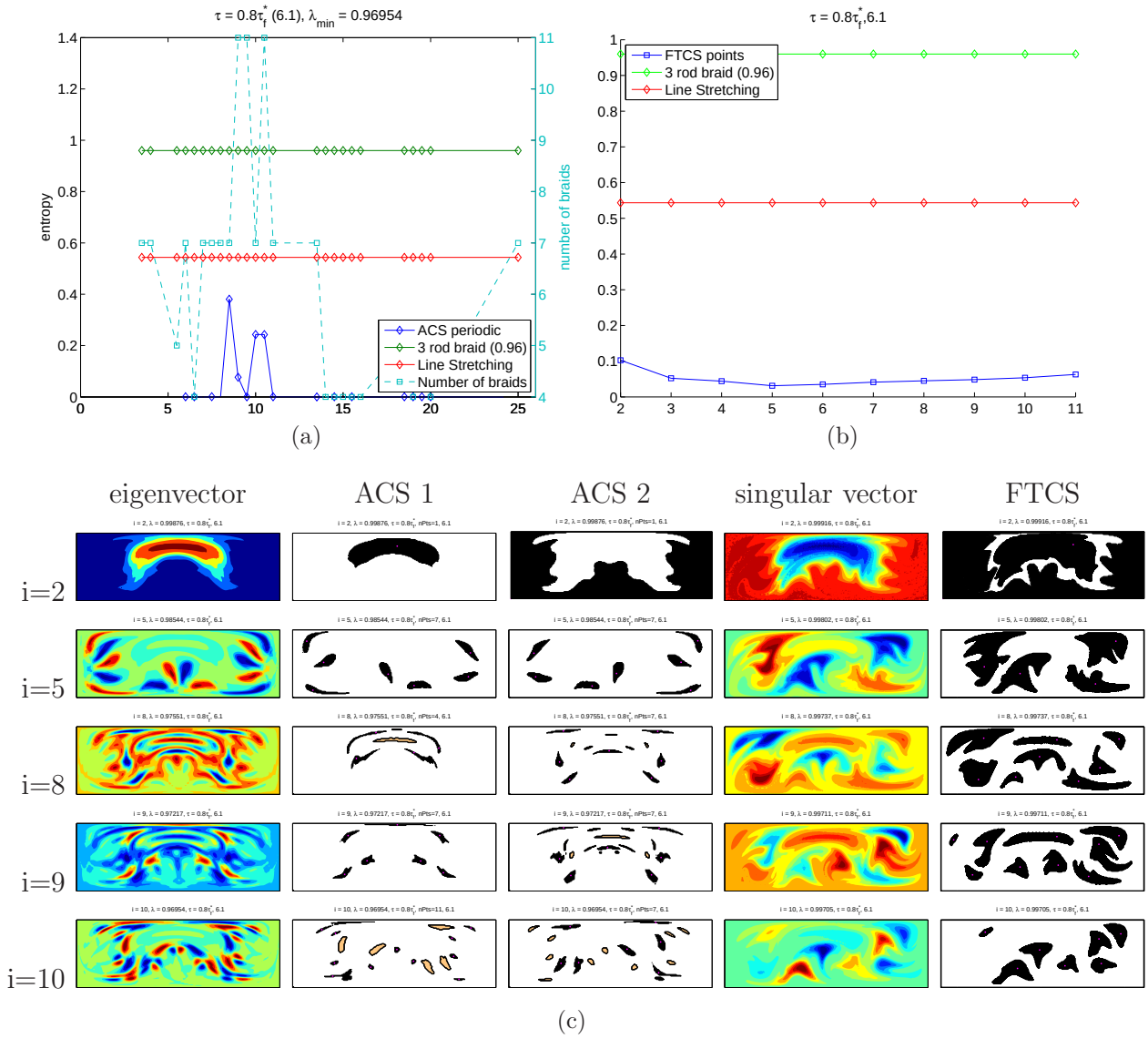

Figure 5.2: Figures (a) and (b) show the entropy for Re=1, $\tau = 0.8\tau_f^*$ calculated using the ACS and FTCS methods respectively, normalised using τ_f^*. The x axis in (a) is the ACS number, where, the two ACS corresponding to the eigenvector (of the reversible matrix) i are numbered $(i-1)\times 2-1$ and $(i-1)\times 2$. The left y axis is the topological entropy (normalised by τ), and the right y axis is the number of braids for each case. In (b), the ith x intercept corresponds to the $(i+1)$th singular vector. The 2nd and 3rd columns in (c) show the two ACS corresponding to the eigenvector in the first column. In these figures, the black structures form the ACS with the highest number of elements in the AIS, where as the light brown structures are coherent structures from the AIS that are not part of that ACS. The magenta points are the representative points for the coherent structures. The rightmost column in (c) shows the FTCS extracted from the singular vectors (4th column).

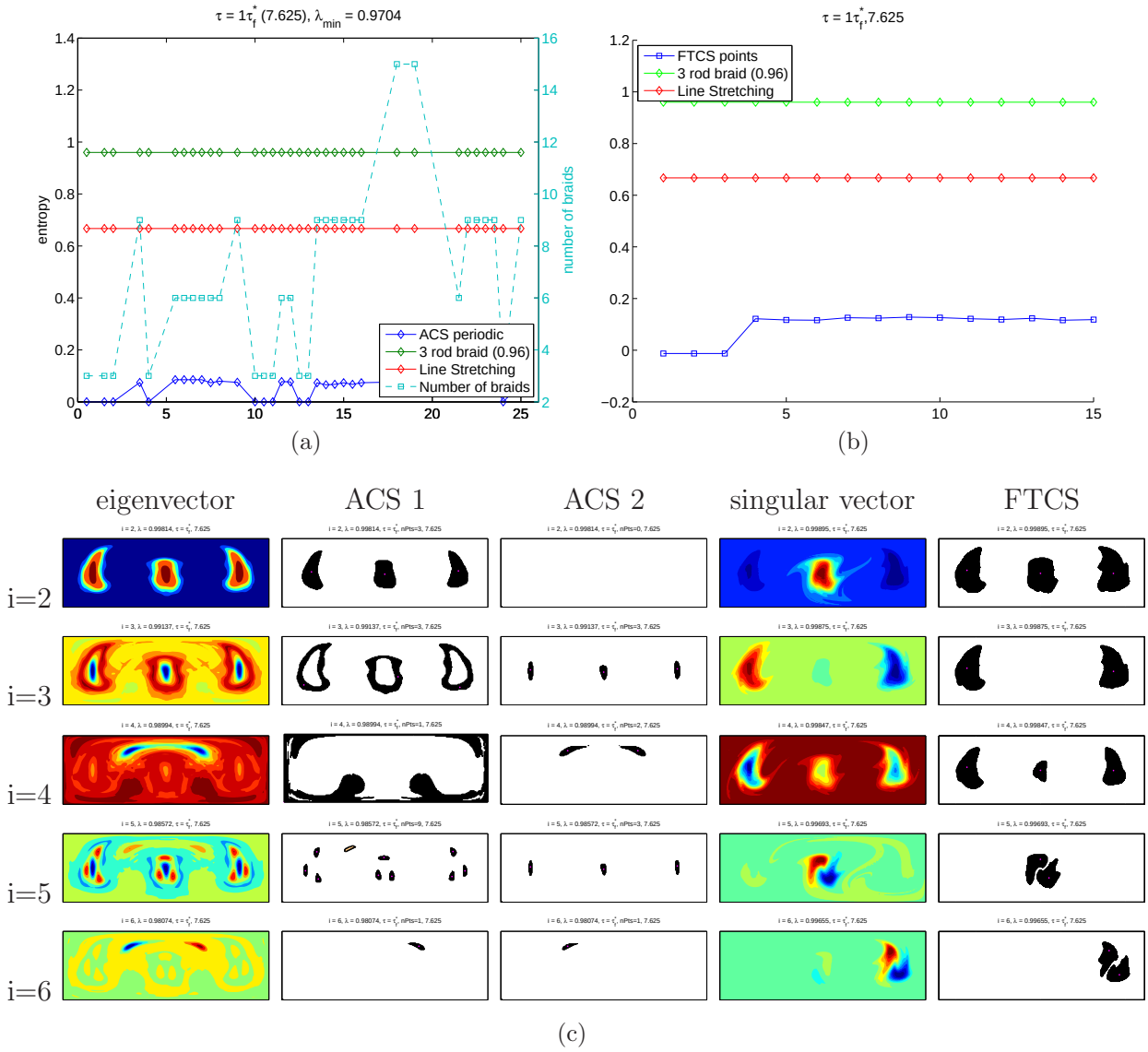

Figure 5.3: Figures (a) and (b) show the entropy for Re=1, $\tau = \tau_f^*$ calculated using the ACS and FTCS methods respectively, normalised using τ_f^*. The x axis in (a) is the ACS number, where, the two ACS corresponding to the eigenvector (of the reversible matrix) i are numbered $(i-1)\times 2-1$ and $(i-1)\times 2$. The left y axis is the topological entropy (normalised by τ), and the right y axis is the number of braids for each case. In (b), the ith x intercept corresponds to the $(i+1)$th singular vector. The 2nd and 3rd columns in (c) show the two ACS corresponding to the eigenvector in the first column. In these figures, the black structures form the ACS with the highest number of elements in the AIS, where as the light brown structures are coherent structures from the AIS that are not part of that ACS. The magenta points are the representative points for the coherent structures. The rightmost column in (c) shows the FTCS extracted from the singular vectors (4th column).

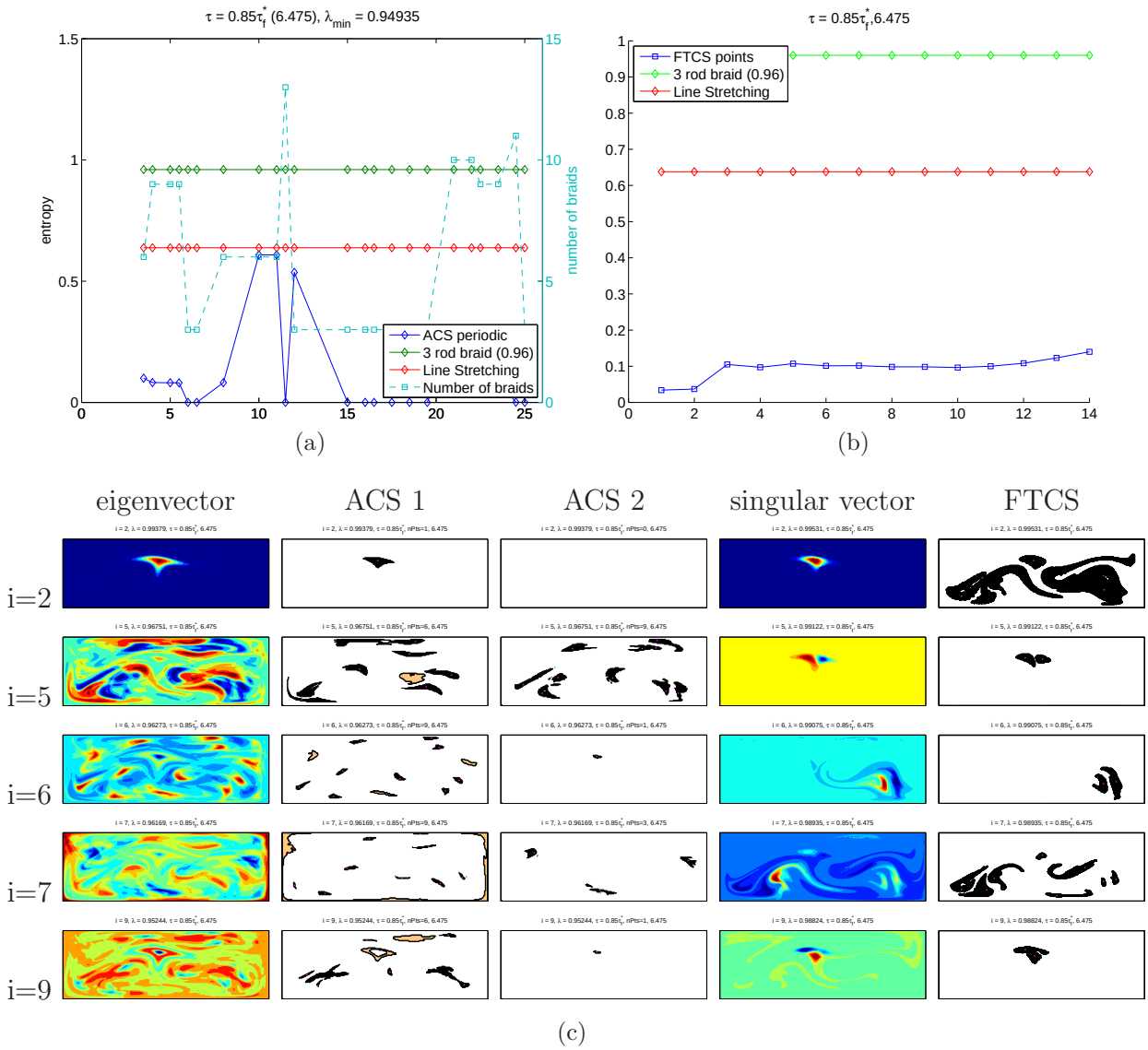

Figure 5.4: Figures (a) and (b) show the entropy for Re=30, $\tau = 0.85\tau_f^*$ calculated using the ACS and FTCS methods respectively, normalised using τ_f^*. The x axis in (a) is the ACS number, where, the two ACS corresponding to the eigenvector (of the reversible matrix) i are numbered $(i-1)\times 2-1$ and $(i-1)\times 2$. The left y axis is the topological entropy (normalised by τ), and the right y axis is the number of braids for each case. In (b), the ith x intercept corresponds to the $(i+1)$th singular vector. The 2nd and 3rd columns in (c) show the two ACS corresponding to the eigenvector in the first column. In these figures, the black structures form the ACS with the highest number of elements in the AIS, where as the light brown structures are coherent structures from the AIS that are not part of that ACS. The magenta points are the representative points for the coherent structures. The rightmost column in (c) shows the FTCS extracted from the singular vectors (4th column).

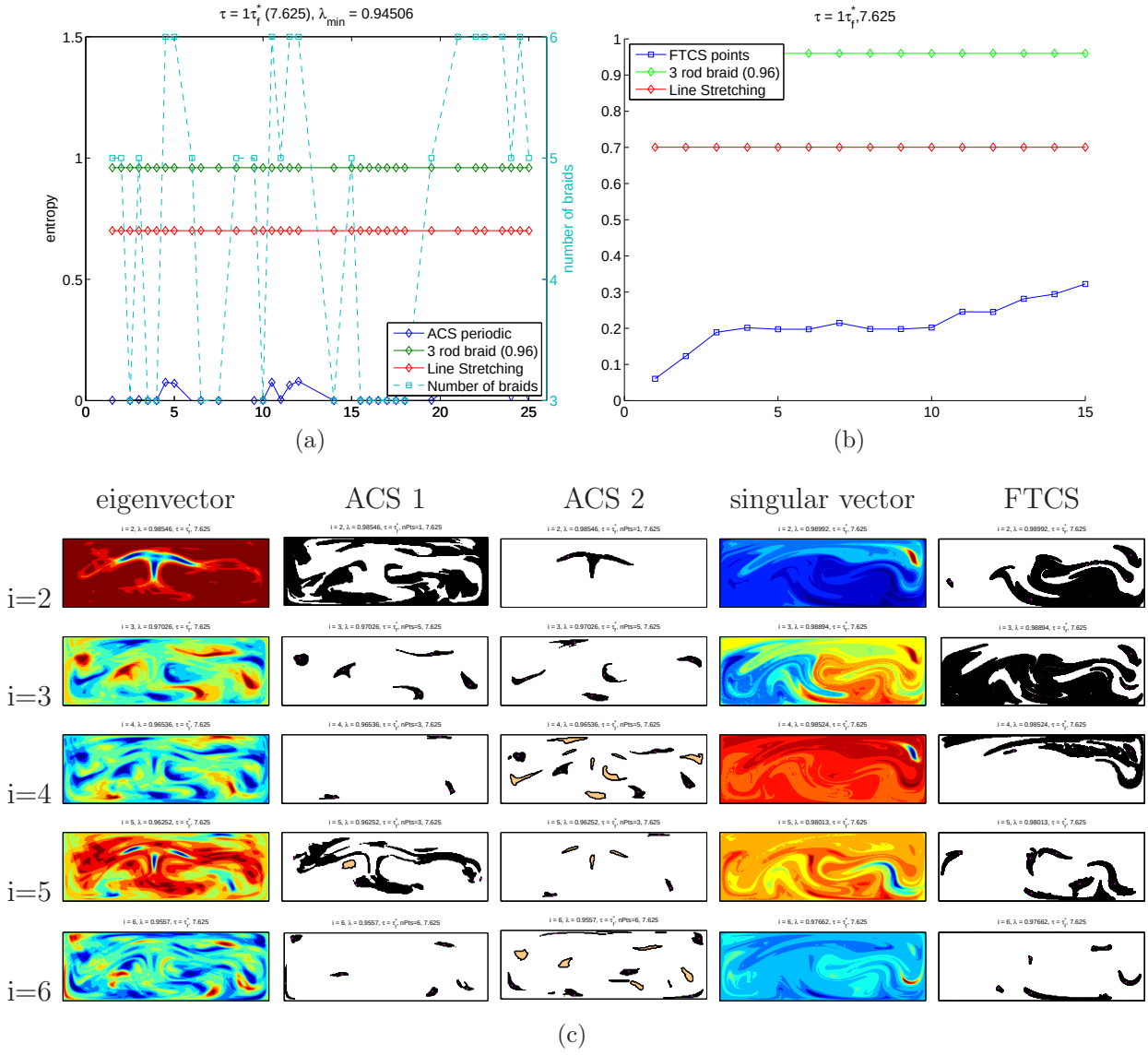

Figure 5.5: Figures (a) and (b) show the entropy for Re=30, $\tau = \tau_f^*$ calculated using the ACS and FTCS methods respectively, normalised using τ_f^*. The x axis in (a) is the ACS number, where, the two ACS corresponding to the eigenvector (of the reversible matrix) i are numbered $(i-1)\times 2-1$ and $(i-1)\times 2$. The left y axis is the topological entropy (normalised by τ), and the right y axis is the number of braids for each case. In (b), the ith x intercept corresponds to the $(i+1)$th singular vector. The 2nd and 3rd columns in (c) show the two ACS corresponding to the eigenvector in the first column. In these figures, the black structures form the ACS with the highest number of elements in the AIS, where as the light brown structures are coherent structures from the AIS that are not part of that ACS. The magenta points are the representative points for the coherent structures. The rightmost column in (c) shows the FTCS extracted from the singular vectors (4th column).

Chapter 6

Conclusions

This work has investigated the relationship between topological entropy of flows and mixing, and the influence of coherent structures in the flow on the dynamics of transport.

Mixing rates were found to be related to the topological entropy of the flow fields for $Re \leq 30$ for the cases considered. Flows based on the pA 3-rod braid, which showed a higher topological entropy overall, had better mixing rates than the flows based on the finite order 3-rod braid, which had a lower topological entropy overall. The variance in mixing rates between cases for the same Reynolds numbers was found to be dependent on the Reynolds number as well. Essentially, increasing the Reynolds number reduced this variance. Lastly, the invariance of the AIS in the flow was shown to be related to the final mixed state.

The flows based on the 3-rod pA Stokes' flow case depict a high topological entropy even when the switching period is perturbed, or inertial effects are included. It is interesting to note that the 3-rod braid shows up as the dominant braid for Reynolds numbers 1 through 50. This is seen for $\tau_*^f \leq \tau \leq 1.2\tau_f^*$ for Re $= 1$, $\tau_*^f \leq \tau \leq 1.25\tau_f^*$ for Re $= 10$, $1.2\tau_*^f \leq \tau \leq 1.4\tau_f^*$ for Re $= 30$ and $1.2\tau_*^f \leq \tau \leq 1.25\tau_f^*$ for Re $= 50$. For Re > 1, these cases also correspond with dips in the topological entropy calculated using the ACS and FTCS as compared to the line stretching method.

This work has shown that the dynamics of coherent structures in the flow influence its complexity, and set oriented methods provide an efficient way to detect them. It was shown that at finite Reynolds numbers as well, just as in the Stokes' flow studies, the topological entropy of the braids formed by the ACS gives us an estimate for the lower bound for the complexity in the flow field. However, unlike the Stokes' flow cases, the ACS from the most dominant eigenvectors of the reversible matrix may not be the best choice to calculate this lower bound. The lower bound predicted by the ACS was found to be a very close approximation of the entropy obtained using the line stretching method in some cases. For the rest, the entropy calculated using the ACS was found to be of the same order of magnitude as the line stretching method.

Thus the ACS method overall is better suited as a tool for predicting a minimum rate of stretching of material lines in the flow field. The ACS methodology can therefore prove to be very helpful in the design of mixing protocols for fluid systems with time periodic flow fields which need to guarantee a minimum mixing rate. The added advantage of using this method is that the AIS structures can be used to easily identify regions of poor mixing in the fluid, especially over short times. Further, the ACS method can be used to complement the line stretching method for calculating the topological entropy of flows where the stretching rate per period is extremely high. This is because the cost of calculating h_f using the line stretching method grows exponenially with the stretching rate per flow period, whereas the cost for the ACS method is independent of the stretching rate.

For most cases, the topological entropy calculated from the FTCS was found to be close to the ACS method. However, for cases where the dominant eigenvectors of the reversible matrix that produced ACS with either finite order braids or trivial braids, h_{FTCS} was found to be a poor approximation of h_f. In such cases, the ensemble averaging method produced better results. For the rest of the cases however, the FTCS method gave better approximations of h_f. These two methods therefore complement each other, and for non time-periodic flows, a combination of the two can be used to estimate the topological entropy of the flow.

Bibliography

[1] P. Rao, A. Duggleby, and M. Stremler, "Mixing analysis in a lid-driven cavity flow at finite Reynolds numbers", J. Fluids. Engg. **134** (2012).

[2] H. Aref, "The development of chaotic advection", Physics of Fluids **14**, 1315–1325 (2002).

[3] H. Aref, "Stirring by chaotic advection", J. Fluid Mech **143**, 1–21 (1984).

[4] J. Ottino, *The Kinematics of Mixing: Stretching, Chaos, and Transport* (Cambridge University Press) (1989).

[5] S. Wiggins and J. M. Ottino, "Foundations of chaotic mixing", Phil. Trans. R. Soc. Lond. A **362**, 937–970 (2004).

[6] P. L. Boyland, H. Aref, and M. A. Stremler, "Topological fluid mechanics of stirring", J. Fluid Mech. **403**, 277–304 (2000).

[7] P. Boyland, M. Stremler, and H. Aref, "Topological fluid mechanics of point vortex motions", Physica D **175**, 69–95 (2003).

[8] E. Gouillart, J.-L. Thiffeault, and M. D. Finn, "Topological mixing with ghost rods", Phys. Rev. E **73**, 036311 (2006).

[9] M. A. Stremler, S. D. Ross, P. Grover, and P. Kumar, "Topological chaos and periodic braiding of almost-cyclic sets", Phys. Rev. Lett. **106**, 114101 (2011).

[10] G. Froyland, "Statistically optimal almost-invariant sets", Physica D **200**, 205–219 (2009).

[11] G. Froyland, N. Santitissadeekorn, and A. Manohan, "Transport in time-dependent dynamical systems: Finite-time coherent sets", Chaos **20**, 043116 (2010).

[12] P. Grover, S. D. Ross, M. A. Stremler, and P. Kumar, "Topological chaos, braiding and bifurcation of almost-cyclic sets", Chaos **22**, 043135 (2012).

[13] M. Dellnitz, G. Froyland, C. Horenkamp, and K. Padberg, "On the approximation of complicated transport phenomena - a dynamical systems approach", GAMM-Mitt **32**, 47–60 (2009).

[14] G. Froyland, K. Padberg, M. England, and A. M. Treguier, "Detection of coherent oceanic structures via transfer operators", Phys. Rev. Lett. **98** (2007).

[15] G. Froyland and K. Padberg, "Almost-invariant sets and invariant manifolds - connecting probabilistic and geometric descriptions of coherent structures in flows", Physica D **238**, 1507–1523 (2009).

[16] W. Thurston, "On the geometry and dynamics of diffeomorphisms of surfaces", Bull. Am. Math. Soc. **19**, 417–431 (1988).

[17] M. Handel, "Global shadowing of pseudo-anosov homeomorphisms", Ergod. Theory Dyn. Syst. **5**, 373–377 (1985).

[18] M. A. Stremler and J. Chen, "Generating topological chaos in lid-driven cavity flow", Physics of Fluids **19**, 103602 (2007).

[19] M. H. M. Bestvina, "Train-tracks for surface homeomorphisms", Topology **34**, 109–140 (1995).

[20] E. Artin, "Theory of braids", Annals of Mathematics **48**, 101–126 (1946).

[21] J.-L. Thiffeault, "Braids of entangled particle trajectories", Chaos **20**, 017516 (2009).

[22] J. S. Birman, *Braids, links and mapping class groups* (Princeton University Press, Princeton, NJ.) (1975).

[23] J.-L. Thiffeault and M. D. Finn, "Topology, braids and mixing in fluids", Phil. Trans. R. Soc. A **364**, 3251–3266 (2006).

[24] T. Hall, "Train: A c++ program for computing train tracks of surface homoemorphism", .

[25] J.-O. Moussafir, "On computing the entropy of braids", Funct. Anal. Other Math. **1**, 37–46 (2006).

[26] I. A. Dynnikov, "On a Yang-Baxter map and the Dehornoy ordering", Russ. Math. Surv. **57**, 592–594 (2002).

[27] S. Newhouse and T. Pignataro, "On the estimation of topological entropy", Journal of Statistical Physics **72**, 1331–1351 (1993).

[28] J.-L. Thiffeault, "Measuring topological chaos", Physical Review Letters **94** (2005).

[29] M. Dellnitz and O. Junge, "On the approximation of complicated dynamical behaviour", J. Numer. Anal. **36**, 491–515 (1999).

[30] C. Canuto, M. Y. Hussaini, A. Quarteroni, and J. Thomas A. Zang, *Spectral Methods, Fundamentals in Single Domains* (Springer-Verlag, Berlin) (2006).

[31] R. Peyret, *Spectral Methods for Incompressible Viscous Flow* (Springer-Verlag Inc, New York) (2002).

[32] J. Kim, P. Moin, and R. Moser, "Turbulent statistics in fully developed channel flow at low Reynolds number", J. Fluid Mech. **177**, 133–166 (1987).

[33] C. Lanczos, *Applied Analysis* (Prentice-Hall, Englewood Cliffs, NJ.) (1956).

[34] M. Liu, F. J. Muzzio, and R. L. Peskin, "Quantification of mixing in aperiodic chaotic flows", Chaos, Solitons & Fractals **4**, 869–893 (1994).

[35] M. A. Stremler, *Encyclopedia of Microfluidics and Nanofluidics*, chapter Mixing measures, 1376–1382 (Springer) (2008).

[36] M. Gheisarieha, "Topological chaos and chaotic mixing of viscous flows", Ph.D. thesis, Virginia Polytechnic Institute and State University, Blacksburg, Virginia (2011).